

SYNTHESIS AND CHARACTERIZATION OF TRANSITION METAL OXIDES AND
DICHALCOGENIDES AND THEIR APPLICATION IN
ORGANIC PHOTOVOLTAICS

by

Diego Barrera Mendez

APPROVED BY SUPERVISORY COMMITTEE:

Julia W. P. Hsu, Chair

Kyeongjae Cho

Christopher Hinkle

Manuel Quevedo-Lopez

Copyright 2017

Diego Barrera Mendez

All Rights Reserved

To Silvia... and my baby that she is carrying

SYNTHESIS AND CHARACTERIZATION OF TRANSITION METAL OXIDES AND
DICHALCOGENIDES AND THEIR APPLICATION IN
ORGANIC PHOTOVOLTAICS

by

DIEGO BARRERA MENDEZ, MS

DISSERTATION

Presented to the Faculty of
The University of Texas at Dallas
in Partial Fulfillment
of the Requirements
for the Degree of

DOCTOR OF PHILOSOPHY IN
MATERIALS SCIENCE AND ENGINEERING

THE UNIVERSITY OF TEXAS AT DALLAS

May 2017

ACKNOWLEDGMENTS

First and foremost, I would like to express my sincere gratitude to my advisor, Professor Julia W. P. Hsu who always showed her trust and belief in me during my Ph.D. Without her patience and support I could not have finished my research. I am thankful to my committee members: Professors Kyeongjae Cho, Christopher Hinkle, and Manuel Quevedo-Lopez for the inspiring suggestions and comments regarding my dissertation and research that I greatly appreciate.

To Dr. Yun-Ju Lee who answered uncountable questions and without his help, advice and expertise, this research would not have happened. I would also like to thank the support from all my friends in the Materials Science and Engineering department and group members: Juan Yi, Kaiyuan Luo, Jian Wang, Lian Xu, Sampreetha Thampy, Michael Womble, Trey Daunis for helping me when I needed and making my graduate student life endurable and fun.

I am grateful to my family in Mexico and SA. Without their constant support and encouragement, it would not have been possible for me to achieve my education goals.

Finally, I would like to especially thank Silvia, my unfailingly supportive wife. I have encountered many hurdles during this journey, and her love and encouragement have kept me focused. This is yours as much as it is mine, thank you from the bottom of my heart.

February 2017

SYNTHESIS AND CHARACTERIZATION OF TRANSITION METAL OXIDES AND
DICHALCOGENIDES AND THEIR APPLICATION IN
ORGANIC PHOTOVOLTAICS

Diego Barrera Mendez, PhD
The University of Texas at Dallas, 2017

Supervising Professor: Julia W. P. Hsu

This Ph.D. research focused on the development of new materials for alternative renewable energy using organic photovoltaics (OPVs). The first step was to establish reliable fabrication and characterization methods of organic photovoltaic devices. The reproducibility of organic photovoltaic cell performance is one of the essential issues that must be achieved before engaging serious investigations of the applications of creative and challenging ideas.

Secondly, we thoroughly studied the surface chemistry of the underlying layer and its critical role on the morphology of the BHJ active layer. We showed that when the active layer (which consists of blends of poly(3-hexylthiophene) (P3HT) and phenyl-C60-butyric acid methyl ester (PCBM)) is deposited and annealed over a sol-gel ZnO electron transport layer surface made from monoethanolamine (MEA) containing precursor, PCBM clusters form during annealing and this phase segregation leads to a drastic reduction of OPV parameters due to both low charge generation and high bimolecular recombination. Rinsing the pyrolyzed ZnO films with solvents or using a ZnO recipe without MEA significantly reduced the formation of PCBM clusters and produced devices with good performance.

Third, we developed new materials suitable for low-temperature processing and large-area deposition methods to be used as transport layer on OPVs. We achieved the synthesis of MoO_x suspensions suitable for large area deposition, with controlled size, stoichiometry, and electronic properties using controlled oxidative dissolution of organometallic powders with H_2O_2 in n-butanol. The small nanoparticle diameters of ~ 2 nm enabled solution processing of nanoparticle films on ITO with electronic properties comparable to solution processed and vacuum deposited counterparts, without the need for any post processing.

We also accomplished the synthesis of transition metal dichalcogenides (TMDs) directly from precursors in solution using a versatile synthesis method. We demonstrate the ability to synthesize few-layer (~ 2 nm) MoS_2 , MoSe_2 , WS_2 , and WSe_2 flakes with relatively large lateral sizes (> 2 μm) using a solvothermal method. We demonstrate that the reducing agent, 1,2-hexadecanediol is critical to ensure TMD formation and eliminate corresponding metal oxide. TEM, Raman, PESA, and Kelvin Probe measurements confirmed that all TMDs are p-type, highly crystalline, exhibit 2H phase and present hexagonal crystalline structure. In addition, thickness for all TMDs was consistent with a few-layer flakes.

Finally, we studied the use of films spray casted from liquid-exfoliated MoS_2 suspensions as hole transport layer for OPVs. Electrical measurements on the devices showed that FF achieved using MoS_2 is identical to that using spin-coated polymeric reference material. Calculations showed that the lower J_{sc} observed in MoS_2 devices is explained by reduced light absorption in the active layer region due to less back-reflected light in MoS_2 devices. With all these results we have contributed to enable a route towards low-cost OPV and other electronics fabrication.

TABLE OF CONTENTS

ACKNOWLEDGMENTS	v
ABSTRACT	vi
LIST OF FIGURES	x
LIST OF TABLES	xvi
CHAPTER 1 Introduction to Organic Photovoltaics.....	1
1.1 Organic Photovoltaics Overview	1
1.2 OPV Basic Principles.....	3
1.3 Solution Processed Materials for OPVs.....	7
1.4 Electronic Structure Measurements in Air.....	11
1.5 Outline of Dissertation.....	14
CHAPTER 2 Influence of ZnO Sol-gel Electron Transport Layer Processing on BHJ Active Layer Morphology and OPV Performance.....	15
2.1 Introduction and motivation.....	16
2.2 Experiments	17
2.3 Results and Discussion	19
2.4 Conclusions.....	30
CHAPTER 3 In Situ Chemical Oxidation of Ultrasmall MoO _x Nanoparticles in Suspension.....	31
3.1 Introduction and motivation.....	32
3.2 Experiments	34
3.3 Results and Discussion	36
3.4 Conclusions.....	42
CHAPTER 4 Solution Synthesis of Few-layer 2H MX ₂ (M= Mo,W; X= S,Se).....	44
4.1 Introduction and motivation.....	46
4.2 Experiments	47
4.3 Results and Discussion	50
4.4 Synthesis of tellurides	64
4.5 Alternative sulfur precursors.....	66
4.6 Alternative molybdenum precursor	69

4.7	Conclusions.....	72
CHAPTER 5 Inverted OPVs With MoS ₂ Hole Transport Layer Deposited By Spray Coating...		73
5.1	Introduction and motivation.....	75
5.2	Experiments	77
5.3	Results and Discussions.....	81
5.4	MoSe ₂ Devices.....	88
5.5	Conclusions.....	89
CHAPTER 6 General Conclusions.....		91
APPENDIX I. Band Structure Measurements on Bulk Transition Metal Dichalcogenides.....		93
	Air stability characterization on other exfoliated TMDs	97
	Electronic characterization on other exfoliated 2-D materials	98
	Conclusions.....	99
APPENDIX II. Conventional OPVs Using NiO _x Deposited by PLD as Hole Transport Layer.		100
REFERENCES		108
BIOGRAPHICAL SKETCH		125
CURRICULUM VITAE		

LIST OF FIGURES

Fig. 1.1 Highest certified conversion efficiencies for a range of PV technologies. This plot is courtesy of the National Renewable Energy Laboratory, Golden, CO.....	2
Fig. 1.2 Basic photoconversion mechanism of an OPV: (a) Light absorption, (b) exciton diffusion, (c) exciton dissociation, and (d) charge transport.	4
Fig. 1.3 (a) Basic structure of an OPV cell and (b) structure of an OPV with buffer layers.	5
Fig. 1.4 (a) Equivalent circuit model for OPV. (b) Typical J - V curves of an OPV cell under dark (black) and under illumination (red) conditions. The open circuit (V_{oc}) and short-circuit current density (J_{sc}) are shown. The maximum output is given by the square $J_{max} * V_{max}$. .	6
Fig. 1.5 Effect of the (a) series resistance and (b) shunt resistance on the solar cell efficiency.....	7
Fig. 1.6 Three dimensional schematic representation of a typical MX_2 structure, with chalcogen atoms (X) in yellow and metal atoms (M) in grey.....	9
Fig. 1.7 Band structures calculated from first-principles density functional theory (DFT) for bulk and monolayer MoS_2	10
Fig. 1.8 Schematic semiconductor band structure and energy levels.	11
Fig. 1.9 Energy alignment in Kelvin probe measurements in floating (left), short-circuit (center), and voltage-nulling situations (right). ³⁹	12
Fig. 1.10 Typical photoelectron spectrum	13
Fig. 2.1 Optical microscopic images of annealed P3HT:PCBM layer deposited on top of ZnO films made by (a) MOE ZnO, (b) EtOH ZnO, (c) rinsed MOE ZnO. (d) $5 \times 5 \mu m$ AFM image of a typical PCBM sample.	20
Fig. 2.2 UV-vis absorbance spectra for various P3HT:PCBM films deposited over MOE ZnO with cluster area fraction of 0.01 (black), 0.07 (red), 0.34 (green), and 0.46 (blue).	21
Fig. 2.3 Cluster area fraction vs MEA concentration in the precursor solution used to make MOE ZnO films, showing a positive correlation between the two parameters.	21
Fig. 2.4 (a) Comparison of FT-IR absorbance spectra for various MOE ZnO films: unpyrolyzed (black), pyrolyzed (blue, $\times 45$), pyrolyzed and rinsed (green, $\times 15$). The NH stretching	

mode at 1420 cm^{-1} is highlighted with an arrow. (b) TGA thermogram of MOE ZnO for temperature range 250– 400 °C.	22
Fig. 2.5 J - V characteristics of solar cells under 100 mW/cm^2 AM 1.5G illumination for devices with different cluster area fraction: 0.01 (black), 0.06 (red), 0.34 (orange), 0.39 (green), and 0.46 (blue).	24
Fig. 2.6 Comparison between MOE ZnO rinsed (black) and EtOH ZnO (blue) on J - V characteristics of solar cells under 100 mW/cm^2 AM 1.5G illumination.	25
Fig. 2.7 Influence of cluster area fraction on OPV device parameters.	26
Fig. 2.8 Current density integrated from EQE spectra, J_{sc} (EQE^*), at different background intensities for P3HT:PCBM devices on MOE ZnO with cluster area fraction of 0.01 (black), 0.33 (red), and 0.46 (blue). Dashed lines represent average J_{sc} (EQE^*) value at $< 10\text{ mW/cm}^2$ background intensity for each device.	28
Fig. 2.9 Effect of cluster area fraction on performance reduction of solar cells taken under 100 mW/cm^2 AM 1.5G illumination: before (solid line) and after (dashed line) white-light biased EQE measurements for a 0.01 cluster area fraction device (black) and a 0.38 cluster area fraction device (red).	29
Fig. 3.1 Picture of microwave synthesis and chemical oxidation of MoO_x nanoparticles. A mixture of molybdenum oxide bis(acetylacetonate) in n-butanol was placed in a microwave reactor (CEM Discovery) and heated using 2.45 GHz radiation. When heated at $200\text{ }^\circ\text{C}$ for 15 minutes, Moacac reacted, forming a brown suspension of nanoparticles. Chemical oxidation of the nanoparticle suspension with $0.1\text{M H}_2\text{O}_2$ for 24 hours yielded a blue suspension of nanoparticles.	35
Fig. 3.2 Effect of chemical oxidation with H_2O_2 on MoO_x nanoparticle properties. a) Dependence of nanoparticle size on chemical oxidation time (up to 24 h), showing that compared to as-synthesized nanoparticles (dashed line), both $0.1\text{M H}_2\text{O}_2$ (blue) and 0.3M caused npMoO_x size to decrease to 1 nm (up to 3 h) and then increase back to 2 nm (24 h). b) Dependence of nanoparticle film Φ versus chemical oxidation conditions, showing Φ of as-synthesized npMoO_x (black) was increased from 4.48 eV to 4.85 eV with $0.05\text{M H}_2\text{O}_2$ (purple) and that the increase was independent of the reaction time between 20 min and 24 hr. In contrast, 0.1M (blue), 0.2M (green), and 0.3M (red) H_2O_2 all caused work function to increase to 5.0 eV with a reaction time of up to 3 hr. However, a further increase in reaction time to 24 h decreased Φ to 4.9 eV.	37
Fig. 3.3 Effect of chemical oxidation conditions on MoO_x nanoparticle stoichiometry. a) Mo 3d XPS spectra of as-synthesized npMoO_x on ITO (crosses) and curve fit (solid), showing mixed oxidation states with contributions from Mo^{5+} , Mo^{4+} , and a small amount of Mo^{6+} .	

b) Mo 3d XPS spectra of npMoO _x after chemical oxidation with 0.05M H ₂ O ₂ for 1 h, showing mixed oxidation states with a majority of Mo ⁶⁺ oxidation state. c) Mo 3d XPS spectra of npMoO _x after chemical oxidation with 0.1M H ₂ O ₂ for 1 h, showing almost complete oxidation to Mo ⁶⁺ oxidation state. d) Mo 3d XPS spectra of npMoO _x after chemical oxidation with 0.1M H ₂ O ₂ for 24 h, showing mixed oxidation states with a majority of Mo ⁶⁺ oxidation state.....	39
Fig. 3.4 O 1s and C 1s regions of XPS spectra for MoO _x nanoparticle films with different H ₂ O ₂ reaction conditions: a) as-synthesized npMoO _x . b) npMoO _x after chemical oxidation with 0.05M H ₂ O ₂ for 1 h. c) npMoO _x after chemical oxidation with 0.1M H ₂ O ₂ for 1 h. d) npMoO _x after chemical oxidation with 0.1M H ₂ O ₂ for 24 h.	41
Fig. 3.5 Φ versus Mo ⁶⁺ fraction for npMoO _x as synthesized and chemically oxidized at 0.025M, 0.035M, 0.042M, 0.05M, 0.1M, and 0.3M H ₂ O ₂ concentrations for 1 h (circles) and at 0.1M H ₂ O ₂ for 24 h (triangle), showing a positive correlation between the two parameters.....	42
Fig. 4.1 Mo 3d XPS spectra of MoS ₂ synthesized with different HDD concentrations: (a) No HDD, (b) 150 mM, and (c) 500 mM. The Mo 3d peaks were deconvoluted to show Mo ⁴⁺ and Mo ⁶⁺ oxidation states contributions, represented by red and blue areas, respectively. The orange areas represent an oxysulfide species contribution. (d) Mo ⁴⁺ fraction in the MoS ₂ films, area under the Mo ⁴⁺ peaks divided by the total Mo peaks area, vs HDD concentration.....	51
Fig. 4.2 HAADF images of synthesized few-layer TMD flakes: a) MoS ₂ and b) WS ₂	52
Fig. 4.3 O 1s, C 1s, and S 2p of XPS spectra for synthesized MoS ₂ at different HDD concentrations: (a) No HDD, (b) 150 mM, and (c) 500 mM.....	54
Fig. 4.4 XPS spectra of TMDs synthesized with 150mM HDD concentration: (a) MoSe ₂ , (b) WS ₂ (c) WSe ₂	55
Fig. 4.5 O 1s and C 1s XPS spectra of synthesized TMDs using 150 mM HDD: (a) MoS ₂ , (b) MoSe ₂ , (c) WS ₂ , and (d) WSe ₂	56
Fig. 4.6 5 x 5 μ m AFM images of typical TMD flakes for (a) MoS ₂ , (b) MoSe ₂ , (c) WS ₂ , and (d) WSe ₂ . Inset: Height profile taken along the white line in the AFM image.	57
Fig. 4.7 1 x 1 μ m AFM image of thick MoS ₂ flakes with small lateral size. Inset: Height profile taken along the white line in the AFM image.....	58
Fig. 4.8 Raman spectra of TMD films deposited on silicon substrates: (a) MoS ₂ , (b) MoSe ₂ , (c) WS ₂ , and (d) WSe ₂	58

- Fig. 4.9 Raman characterization for MoS₂ flakes. (a) Optical image and (b) Raman intensity mapping at 401 cm⁻¹ (A_{1g} mode peak, dashed line) of an individual MoS₂ nanoflake using 532 nm laser excitation. (c) Raman spectra of a typical MoS₂ nanoflake deposited on silicon substrate showed in (a). 59
- Fig. 4.10 HAADF images of synthesized few-layer TMD flakes: (a, e) MoS₂, (b, f) MoSe₂, (c, g) WS₂, and (d, h) WSe₂. In (g), W atomic positions have been resolved clearly while the intensity of S atoms is very weak. The atomic positions have been labeled in the high resolution HAADF images: Mo (green), W (magenta), S (Yellow), and Se (Orange). All the TMD flakes show 2H structure. 60
- Fig. 4.11 Photoelectron spectrum of oleylamine and oleylamine in presence of HDD(150 mM).62
- Fig. 4.12 Schematic representation of the impact of the formation of an interface dipole on the ionization energy at the oleylamine-MoS₂ interface denoting a shift of vacuum level at the interface due to dipole layer formation. 64
- Fig. 4.13 XPS spectra of tellurides synthesized using 150mM HDD: (a) MoTe₂, (b) WTe₂. 65
- Fig. 4.14 XPS spectra of sulfides synthesized with sulfur powder as chalcogen precursor: (a) MoS₂, (b) WS₂. The Mo 3d and W 4f peaks were deconvoluted to show different oxidation states contributions, represented by red, orange, and blue areas. 67
- Fig. 4.15 XPS spectra of sulfides synthesized with CS₂ as chalcogen precursor: (a) MoS₂, (b) WS₂. The W 4f peaks were deconvoluted to show different oxidation states contributions, represented by red, orange, and blue areas. 69
- Fig. 4.16 XPS spectra of TMD flakes synthesized with MoCl₅ as molybdenum precursor: (a) MoS₂, (b) MoSe₂. The Mo 3d peaks were deconvoluted to show Mo⁴⁺ and Mo⁶⁺ oxidation states contributions, represented by red and blue areas, respectively. 71
- Fig. 4.17 SAED diffraction pattern of MoS₂ flakes synthesized with 150 mM HDD, using different molybdenum precursor: (a) MoCl₅ and (b) MoCl₃. 71
- Fig. 5.1 Inverted organic photovoltaics with MoS₂ as the hole transport layer. (a) Schematic of the device architecture. (b) Energy diagram of the P3HT:PCBM active layer sandwiched between the ITO anode and the Ag cathode utilizing ZnO and MoS₂ as the electron transport layer and hole extraction layer, respectively. 81
- Fig. 5.2 Liquid-exfoliated MoS₂ characterization. (a) Mo 3d and S 2p XPS spectra. (b) Raman spectra at 532 nm excitation wavelength. (c) STEM images showing 2H structure. 82

- Fig. 5.3 Optical, Raman and AFM characterization for MoS₂ HTL films. (a) Optical microscopic image of a typical MoS₂ spray-coated on top of P3HT:PCBM. (b) Raman intensity mapping at 375 cm⁻¹ (E_{2g} mode peak) of the MoS₂ film on P3HT:PCBM, using 532 nm laser excitation showing complete coverage. (c) 2 x 2 μm tapping mode AFM of a typical MoS₂ film spray-coated on top of P3HT:PCBM. 83
- Fig. 5.4 J-V characteristics of solar cells under (a) 100 mW/cm² AM 1.5G illumination and (b) darkness for devices fabricated with MoS₂ (blue), PEDOT:PSS (red), and without HTL (black). Generation rate for photovoltaic devices fabricated with (c) MoS₂, and (d) PEDOT:PSS. 85
- Fig. 5.5 UV-vis absorbance spectra for spray-coated MoS₂ (blue) and spin-coated PEDOT:PSS (red) films deposited on glass. 86
- Fig. 5.6 Influence of the active layer thickness on the MoS₂ device performance. Photocurrent profile ratio between MoS₂ and PEDOT:PSS devices calculated from TMM (dashed line), and experimental results obtained from J_{sc} (solid markers). 87
- Fig. 5.7 J-V characteristics of solar cells under (a) 100 mW/cm² AM 1.5G illumination and (b) darkness for devices fabricated with MoSe₂ (green) and MoS₂ (blue). 89
- Fig. A.I.1 (a) Kelvin probe measurements of the Φ of two different samples MoS₂-A and MoS₂-B. (b) Φ evolution recorded on another (MoS₂-C) freshly exfoliated surface (0 h) until reaching the initial value (dashed line) after a week (168 h) in air. (c) Φ measurements on as-exfoliated HOPG. The HOPG Φ averaged from 3000 measurements during 1 h is 4.55 eV. Panels d and e show the IE measurement of MoS₂-A and MoS₂-B, respectively. The photoemission threshold energy for this second slope is 5.40 eV. 95
- Fig. A.I.2 Band diagram constructed from the Φ measurements on two different MoS₂ crystals, and using the measured values of electron affinity ($\chi = 4.3$ eV) and bandgap (E_g = 1.3 eV). 96
- Fig. A.I.3 TMD stability as function of time exposure in air. The plot shows the Φ measured immediately after exfoliation (0 h) and after different exposure times in air (1 h, 24 h, 72 h, and 168 h). The pre-exfoliation Φ value is represented by the dashed lines for each sample, measured on as-received samples exposed to air for long periods of time (< 1 month). 98
- Fig. A.II.1 Electronic properties characterization for NiO_x films deposited by PLD using oxygen partial pressure of 1 mT (red), 5 mT (orange), 8 mT (green), 10 mT (blue), 15 mT (gray), and 25 mT (cyan). (a) Photoelectron spectroscopy in air and (b) UV-vis absorption. Dashed lines in (b) indicate the extrapolated bandgap values. 101

Fig. A.II.2 Conventional device architecture using NiO _x films as HTL.....	103
Fig. A.II.3 J-V response under (a) AM 1.5 100 mW/cm ² and (b) darkness for conventional P3HT:PCBM OPVs with as-deposited NiO _x films deposited at different oxygen partial pressure as HTL, 1 mT (red), 5 mT (orange), 8 mT (green), 10 mT (blue), 15 mT (gray), and 25 mT (cyan).	103
Fig. A.II.4 NiO _x films resistivity from Hall effect measurements (black), showing a positive correlation with R _{se} from OPVs fabricated with NiO _x HTL (red).....	104
Fig. A.II.5 J-V response under (a) AM 1.5 100 mW/cm ² and (b) darkness for conventional P3HT:PCBM OPVs with NiO _x films deposited 10 mT oxygen partial pressure, annealed at 300 °C for 2 h in air (blue) and under O ₂ atmosphere (red) as HTL.	106

LIST OF TABLES

Table 2.1 Summary of the device performance parameter dependence on cluster area fraction obtained from J - V characteristics of solar cells taken under 100 mW/cm^2 AM 1.5G illumination. Series resistance (R_{se}) and shunt resistance (R_{sh}) were calculated from J - V characteristics measured in the dark.	24
Table 2.2 Summary of the device performance parameter of rinsed MOE ZnO and EtOH ZnO obtained from J - V characteristics of solar cells measured under 100 mW/cm^2 AM 1.5G illumination.	25
Table 2.3 Summary of the device performance parameter change before and after white-light EQE measurements for devices with two different cluster area fractions.	29
Table 4.1 XPS binding energy values comparison for MoO_x nanoparticles as synthesized and MoS_2 flakes synthesized without HDD.	51
Table 4.2 Electronic properties of synthesized TMDs using 150 mM HDD.	61
Table 4.3 Ionization energies of MoS_2 films obtained from synthesized solution, liquid exfoliation solution, and commercial powder.	62
Table 4.4 Ionization energies of commercial powder MoS_2 measured directly on the powder and films deposited from commercial powder MoS_2 dispersion in DCM following different preparation methods.	63
Table 5.1 Summary of the device performance obtained from J - V characteristics of organic photovoltaics taken under 100 mW/cm^2 AM 1.5G illumination and darkness.	85
Table 5.2 Summary of the device performance obtained from J - V characteristics of organic photovoltaics taken under 100 mW/cm^2 AM 1.5G illumination and darkness.	89
Table A.I.1 Φ and IE measurements on two different samples before and after 25 min from exfoliation.	94
Table A.I.2 IE measurements on MoS_2 , MoSe_2 , WS_2 , and WSe_2 before and immediately after mechanical exfoliation.	97
Table A.I.3 Electronic structure characterization done on geological and synthesized 2-D materials.	99

Table A.II.1 Summary of electronic properties of NiO _x films deposited at different oxygen partial pressures.....	101
Table A.II.2 Performance of conventional P3HT:PCBM OPVs with as-deposited NiO _x HTL under AM 1.5G 100 mW/cm ² illumination.	104
Table A.II.3 Electronic properties of NiO _x films deposited at 10 mT at different annealing conditions.....	105
Table A.II.4 Performance of conventional P3HT:PCBM OPVs with annealed NiO _x HTL under AM 1.5G 100 mW/cm ² illumination.	106

CHAPTER 1

INTRODUCTION TO ORGANIC PHOTOVOLTAICS

1.1 Organic Photovoltaics Overview

Over the past decade, the field of renewable energy production experienced a rapid growth as a result of the increased awareness regarding the limited availability of fossil fuels, the negative impact on the environment induced by their use, and the high price volatility of oil.¹ Amongst renewable energy sources, photovoltaics (PV) represent one of the most promising technologies because it is an abundant and easily accessible source of power.² In addition of being plentiful, solar radiation is also widely available geographically, giving photovoltaic technology a significant portability and scalability advantage over other alternative energy technologies.³

The major PV technology commercially available nowadays is crystalline silicon, represents around 90% of the market^{1,4} and it is mainly based on costly batch-to-batch semiconductor processing production techniques. Thus, finding an alternative PV technology is essential and organic photovoltaics (OPVs) have acquired much attention in this area during the past decade.⁵ OPV technologies combine manufacturing adaptability, the potential to be flexible, lightweight and semitransparent.^{2,3} In addition to these qualities, the main property that makes this technology attractive is the potential to be manufactured in a continuous printing process by large-area coating on low cost substrates, thus considerably less effort and production energy are needed for the fabrication process.⁶ For comparison, a typical Si wafer production plant with a 30 cm wafer process has an annually processed area output of 88,000 m²/year. A typical printing machine can produce the same area in 1-10h.³

Currently, the power conversion efficiency (PCE) and operational stability of OPV are considerably lower than those offered by silicon technology. Research scientists have been focused on improving the PCE and operational stability of the devices, with a recent report of 11.9% (**Fig. 1.1**). Although this value falls short of 25-30% PCE level offered by inorganic PV cells, it may be sufficient for a feasible commercial proposition when substantially less expensive production budget for OPV is considered.²

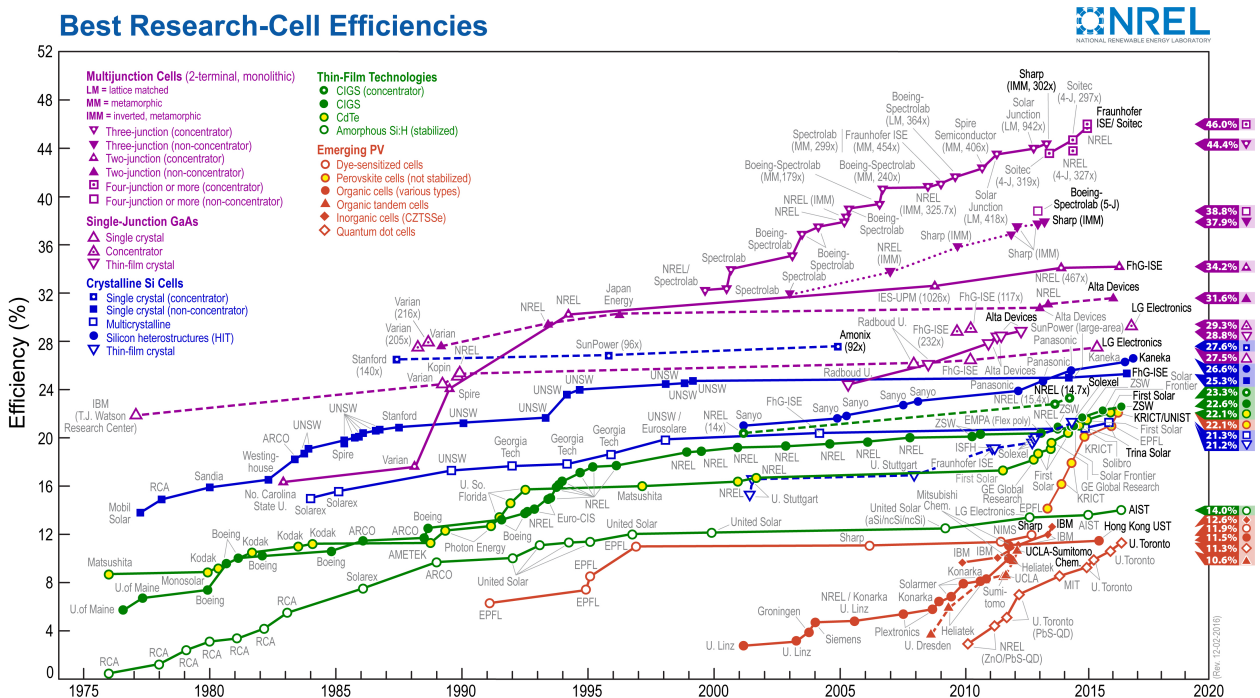


Fig. 1.1 Highest certified conversion efficiencies for a range of PV technologies. This plot is courtesy of the National Renewable Energy Laboratory, Golden, CO.

In the remaining chapters, describes basic mechanisms of OPV and different approaches proposed to improve the PCE of these devices will be discussed. The rest of the thesis, details about previous work performed in the last three years will be provided, and future research plan will be described.

1.2 OPV Basic Principles

1.2.1 OPV Photoconversion Mechanism

The basic photoconversion mechanism of OPVs is shown in **Fig. 1.2**: (a) Sunlight enters through the transparent electrode. The absorption then takes place in the active layer, the excitation caused by the absorbed photons results in the creation of excitons, which consists of a Coulombically bounded electron-hole pair. (b) Excitons diffuse through the active layer with a diffusion length of about 5-10 nm in an organic material.⁷ (c) When excitons reach the interface between the donor and the acceptor, the electric field dissociates the exciton to form free charges (electron and hole). The energy required to split an exciton is in the range of 100-400 meV compared to a few meV for crystalline inorganic semiconductors.⁸ Room temperature thermal energy kT and typical applied electric field are not sufficient to dissociate these excitons.⁷ In order to split excitons into free charge carriers, the energy can be provided in the presence of an electron accepting material with a different electron affinity than the donor material.^{7,8} Because the typical exciton diffusion length in conjugated polymers is limited to ~ 10 nm, the donor and acceptor materials should form nanoscale interpenetrating networks within the whole photoactive layer to ensure an efficient dissociation of excitons.⁹ In this sense bulk heterojunction (BHJ) has a conceptual advantage, the donor and acceptor materials are deposited such that their interface area is maximized while typical dimensions of phase separations are within the exciton diffusion range.¹⁰ (d) The free charges then transport to the cathode (electron) and anode (hole), so that a photocurrent is generated.¹¹ Another important difference to inorganic semiconductors lies in the orders of magnitudes lower charge-carrier mobility in organic semiconductors,¹² which has a

large effect on the design and efficiency of organic semiconductor devices. However, organic semiconductor have strong absorption coefficients ($\geq 10^5 \text{ cm}^{-1}$), which partly balances low mobilities, giving high absorption in even $< 100 \text{ nm}$ thin devices.¹³

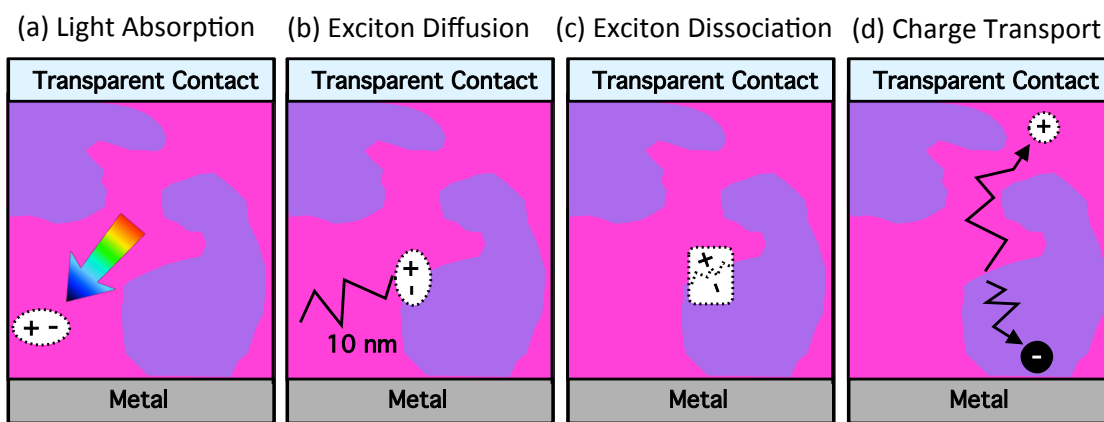


Fig. 1.2 Basic photoconversion mechanism of an OPV: (a) Light absorption, (b) exciton diffusion, (c) exciton dissociation, and (d) charge transport.

In the simplest OPV cell architecture the active layer is in direct contact with both the anode and the cathode (**Fig. 1.3a**). This makes it possible for the acceptor material to transfer electrons to the hole-collecting anode, and vice versa, resulting in large leakage current, recombination, and decreased PV performance of the OPV.¹⁴ To avoid leakage and improve charge collection, buffer layers are inserted to change the interface between active layers and electrodes. **Fig. 1.3b** shows the structure of an OPV enhanced with both electron transport layer (ETL) and a hole transport layer (HTL). These layers adjust the energetic barrier height between the active layer and the electrodes, form a selective contact for carriers of one sort, set up the internal field, determine the polarity of the device, and sometimes act as optical spacer.^{8,15}

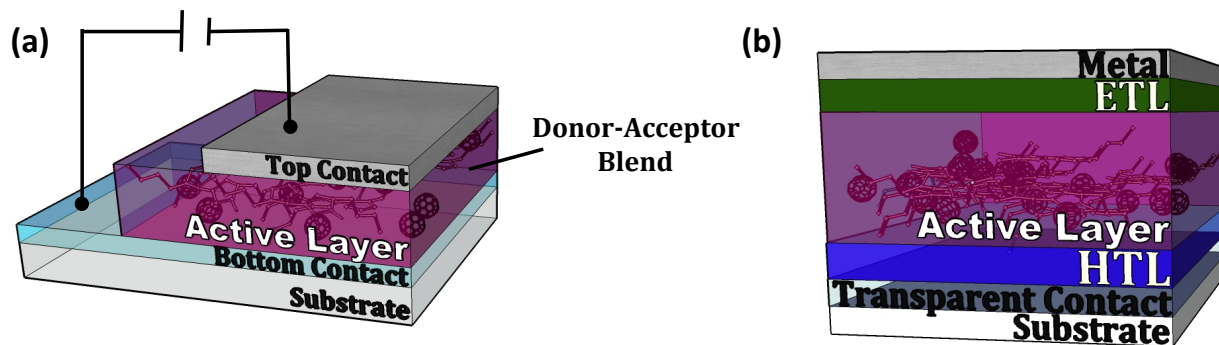


Fig. 1.3 (a) Basic structure of an OPV cell and (b) structure of an OPV with buffer layers.

1.2.2 OPV Characterization

OPV devices, like all other photovoltaics, can be described by the equivalent circuit shown in **Fig. 1.4a**. One of the primary ways to characterize a solar cell is by measuring current density as a function of applied voltage in the dark and under illumination. The typical J - V characteristics of OPVs are shown in **Fig. 1.4b**. The J - V curve of the cell in dark is depicted in black. When a cell is illuminated, the J - V curve is shifted down by the short-circuit current density, J_{sc} (**Fig. 1.4b**, red), which is the current density at zero bias. The open-circuit voltage, V_{oc} , corresponds to the zero current voltage and it balances the built-in field.¹⁶ When the cell is placed in an open circuit and it is illuminated, electrons and holes separate and flow towards the low and high work functions, respectively. At the same point the injected current equals the photocurrent. The square $J_{max}V_{max}$ is the maximum work the cell is able to yield. The fill-factor FF is a measure of closeness of the solar cell J - V curve to the rectangular shape (the ideal shape), and it is given by $J_{max}V_{max}/J_{sc}V_{oc}$. The PCE is defined by the power output delivered by the OPV divided by the incident light power.¹⁶

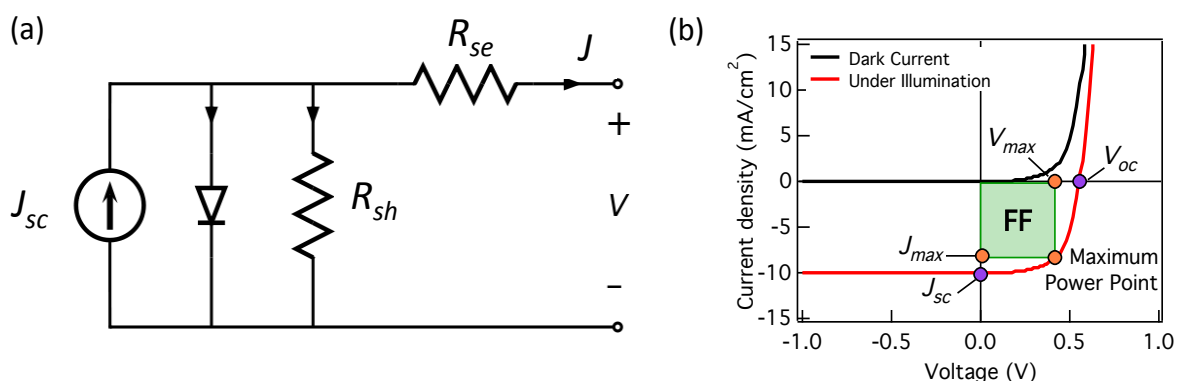


Fig. 1.4 (a) Equivalent circuit model for OPV. (b) Typical J - V curves of an OPV cell under dark (black) and under illumination (red) conditions. The open circuit (V_{oc}) and short-circuit current density (J_{sc}) are shown. The maximum output is given by the square $J_{max} * V_{max}$.

$$PCE = V_{oc} \cdot J_{sc} \cdot FF / P_{in} \quad \text{Eqn. 1}$$

In practice, solar cells can deviate from the ideal behavior predicted due to various reasons. The photogenerated charges have to travel through the semiconductor region to reach the respective electrode, which are thin and have an intrinsic resistance. This introduces an effective series resistance (R_{se}) into the photovoltaic circuit that generates a voltage drop and therefore prevents the ideal photovoltaic voltage from developing when a current is drawn. Besides the R_{se} , a fraction of the photogenerated carriers can also flow through the edges of the device instead of flowing through the external load. These effects prevent photogenerated carriers from flowing in the external circuit and are represented by an effective internal parallel or shunt resistance (R_{sh}) that diverts the photo current away from the load.¹⁷ The R_{se} can significantly deteriorate the solar cell performance as shown in **Fig. 1.5a**, where $R_{se} = 0$ is the best solar cell case. It is clear how the available maximum power decreases with the series resistance, reducing the cell efficiency. Similarly, low R_{sh} values due to extensive defects in the material also reduce the efficiency (**Fig. 1.5b**).

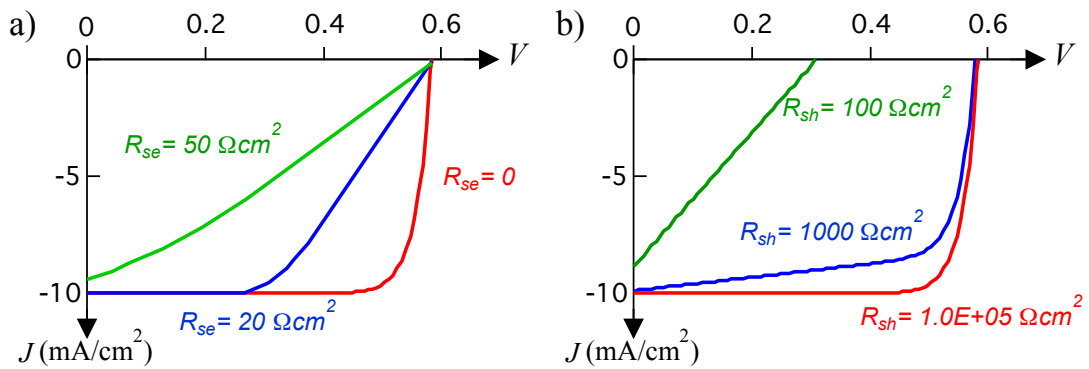


Fig. 1.5 Effect of the (a) series resistance and (b) shunt resistance on the solar cell efficiency.

1.3 Solution Processed Materials for OPVs

In Chapter 1.2.1 the general working principles of OPV cells were discussed. These include light absorption, exciton dissociation, free charges transport, and charge collection.¹¹ Using strategies to maximize each step, improvement of the OPV key parameters can be achieved, and thus, the OPV overall performance. Since one asset of OPVs is its compatibility with large-area fabrication, developing new materials suitable for low-temperature processing and large area deposition methods to be used as transport layer on OPVs is needed.

The synthesis of material suspensions suitable for large-area deposition, with controlled size, stoichiometry, and electronic properties enables a route towards low-cost OPV fabrication. Study of synthesis conditions on physical, chemical, and electric properties of these nanomaterials, as well as the use of films casted from these suspensions as transport layer for OPV will be demonstrated in the next chapters.

1.3.1 Metal Oxides

Metal oxide films for OPV transport layers are commonly deposited by thermal evaporation methods or sol-gel processes that require temperatures higher than 300 °C. These deposition methods inhibit one of the key assets of OPV technologies, which is the potential to be fabricated on flexible substrates. A widely used substitute for vacuum processed oxide films is the poly(3,4-ethylenedioxythiophene):poly(styrenesulfonate) (PEDOT:PSS); unfortunately, PEDOT:PSS has been shown to initiate a number of degradation mechanisms in organic electronic devices which limit the device lifetime and cause severely reliability issues.¹⁸

Consequently, there have been strong efforts to achieve low-temperature solution processed films. Only a few have been reported such as ZnO nanoparticles,¹⁹⁻²¹ WO₃,²² MoO₃,²³ and V₂O₅.²⁴ Nevertheless, the performance of these solution processed films depends strongly on the type and quantity of organic additives during synthesis and post-processing steps. Thus, development of new materials suitable for low-temperature processing and large-area deposition methods to be used as transport layer on OPVs is critical.

1.3.2 Transition Metal Dichalcogenides

The two-dimensional transition metal dichalcogenides (TMDs) are highly anisotropic layered, graphene-like compounds that are of great interest in basic research. Due to a large variety of electronic, optical, mechanical and thermal properties that makes them excellent candidates for electronic applications²⁵⁻²⁷ because of its 2D nature, tunable bandgap,²⁸ and high electron mobility.²⁹

Many TMD materials exist in bulk form as stacks of strongly bonded layers with weak interlayer attraction, allowing exfoliation into individual atomically thin layers.³⁰ These materials have the formula MX_2 , where M is a transition metal element from group IV, V, or VI, and X is a chalcogen (S, Se or Te). They form layered structures of the form X-M-X, with the chalcogen atoms in two hexagonal planes separated by a plane of metal atoms, as shown in **Fig. 1.6**.

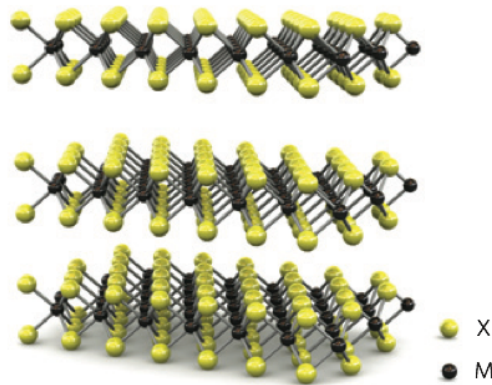


Fig. 1.6 Three dimensional schematic representation of a typical MX_2 structure, with chalcogen atoms (X) in yellow and metal atoms (M) in grey.²⁹

Flexibility and transparency are also desirable characteristics for next-generation electronics. Researchers are now turning to TMDs as ultrathin materials with tunable bandgaps that can be used in all sort of electronic applications, such as transistors,^{29,31} self-switching diodes,³² light-emitting diodes,³³ and photodetectors.³⁴ In some semiconducting TMDs, for example MoS_2 , there is a transition from an indirect bandgap (1.3 eV) in the bulk to a direct bandgap in the single-layer form (1.8 eV)³⁵ as shown in **Fig. 1.7**. Furthermore, the relatively high Earth abundance of TMDs and their direct bandgaps in the visible range make them an attractive material for solar cells.³⁶

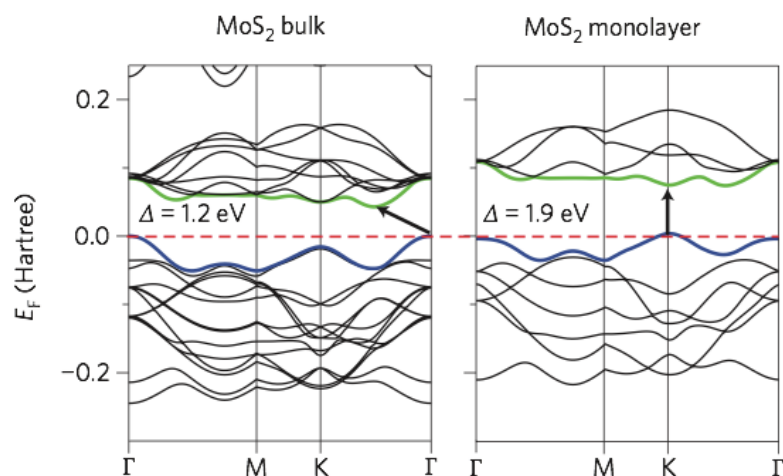


Fig. 1.7 Band structures calculated from first-principles density functional theory (DFT) for bulk and monolayer MoS₂.³⁵

Reliable production of TMDs with uniform properties is essential for translating their electronic and optical properties into applications.²⁵ Stoichiometry, size, layer thickness, and electronic properties of TMDs may vary depending on the method employed to obtain single or multilayers of TMD flakes: mechanical exfoliation, liquid exfoliation, CVD, epitaxial growth, and solvothermal synthesis have all been used.^{25,37} Solution-based colloidal synthetic route for TMDs can be useful because it represents mild reaction conditions and easy tunability in terms of size, composition, and monodispersity.³⁸

Although TMDs have been widely studied for decades, their role as near-atomically thin materials is new and current reports on solvothermal synthesis of layered TMD nanocrystals in nanometric size are scarce.²⁹

1.4 Electronic Structure Measurements in Air

A simplified band structure for a semiconductor is shown in **Fig. 1.8**. For semiconductors, the fundamental bandgap (E_g) is framed by the valence band maximum (VBM) and conduction band minimum (E_{CBM}). The work function of a material (Φ) is the energy required to remove an electron from the Fermi energy to the vacuum level ($E_{VAC} - E_F$). Finally, the ionization energy (IE) is the energy required to remove an electron from the valence band maximum to the vacuum level.

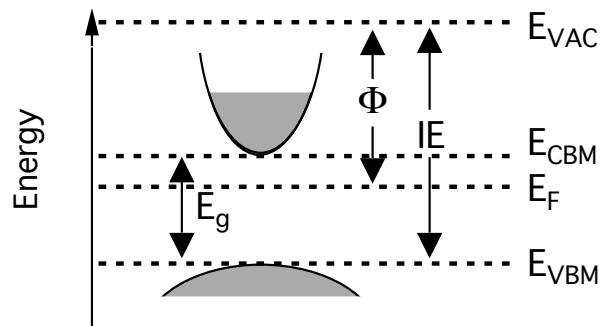


Fig. 1.8 Schematic semiconductor band structure and energy levels.

1.4.1 Kelvin Probe for Work Function Measurements

The work function of a material can be measured using different methods, including ultraviolet photoelectron spectroscopy (UPS) and Kelvin Probe (KP). Unlike UPS, the Kelvin probe does not require ultra-high vacuum conditions to measure work function. Therefore, it offers a distinct advantage over UPS of being able to quickly screen the work function of many samples under ambient conditions. Additionally, the KP also has higher resolution (5–20 meV vs. 100 meV in UPS),³⁹ which is useful for discerning small changes in sample work function.

The Kelvin probe is a non-contact technique employing a vibrating capacitor to measure the work function difference between a flat probe and the surface of a sample. When brought into close proximity of the surface, the vacuum levels are aligned, but each material (probe and sample) has a different work functions (**Fig. 1.9**, left). By connecting the two materials externally, electrons flow from the lower Φ to the higher Φ material so that, equal and opposite surface charges are formed and the Fermi energies are equal. In addition, an electrostatic potential between the tip and sample is generated called the contact potential difference or V_{CPD} , which equals the Φ difference between the tip and the sample (**Fig. 1.9**, center). In this equilibrated state, the potential field equals the work function between the materials. V_{CPD} can be determined by applying a backing potential (V_b) until the field between the two materials is zeroed (**Fig. 1.9**, right).³⁹ By knowing the work function of the tip, the work function of the sample can be obtained.

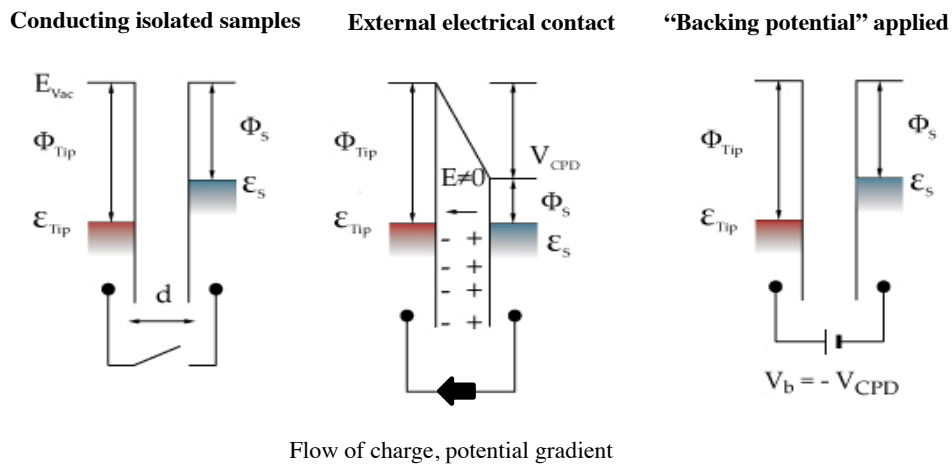


Fig. 1.9 Energy alignment in Kelvin probe measurements in floating (left), short-circuit (center), and voltage-nulling situations (right).³⁹

1.4.2 Photoelectron Spectroscopy in Air

The ionization energy (IE) of a material can be measured by photoelectron spectroscopy in air (PESA).⁴⁰ This is a non-contact, non-destructive technique that employs an open counter electron detector operated under atmospheric pressure with a low photoexcitation energy UV source (3.4 – 6.2 eV). UV-rays emitted from deuterium lamp are set through a grating monochromator, and then focused on a sample surfaces (spot diameter of 2 mm⁴⁰) in air. The spectra are acquired by increasing the energy of UV photon from 3.4 eV to 6.2 eV, with a 0.05 eV step. When the energy of UV ray is higher than the IE of the sample material, the photoelectrons are emitted from the sample surface and ionize the O₂ in the air. These ions are detected and counted in the air by the open counter. The crossing point of the background and the yield line is called photoemission threshold energy (**Fig. 1.10**). If the sample is a metal, the relationship between the photon energy and the square root of yield looks linear, the photoemission threshold energy indicates the Φ of the metal. If the sample is semiconductor, the cube root of yield shows a linear relationship with the incident photon energy, and the photoemission threshold energy equals the *VBM* of the semiconductor.⁴¹

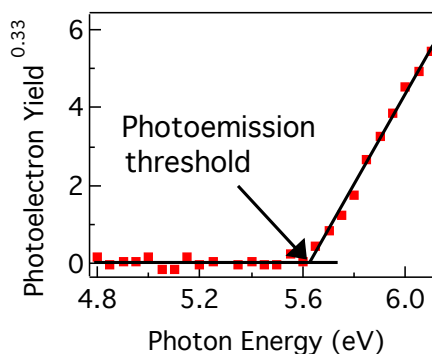


Fig. 1.10 Typical photoelectron spectrum

1.5 Outline of Dissertation

From Chapter 2 to Chapter 5, each chapter presents published/submitted results of research projects. Chapter 2 summarizes my first project related to the surface chemistry of ZnO ETL and its critical role on the morphology of the BHJ active layer ‘Influence of ZnO sol-gel electron transport layer precursor processing on BHJ active layer morphology and OPV performance’. Chapter 3 summarizes the project related to MoO_x synthesis employing an *in situ* oxidation using H₂O₂ ‘In Situ Chemical Oxidation of Ultrasmall MoO_x Nanoparticles in Suspensions’. Chapter 4 and Chapter 5 present submitted results of transition metal dichalcogenides studies. Chapter 4 discusses the solution synthesis and characterization of few-layer MoS₂, MoSe₂, WS₂, and WSe₂: ‘Solution synthesis of few-layer 2H MX₂ (M=Mo,W; X=S,Se)’. Chapter 5 reviews studied the fabrication of OPVs using spray coated films from liquid-exfoliated MoS₂ suspensions as hole transport layer: ‘Inverted OPVs with MoS₂ hole transport layer deposited by spray coating’. Chapter 6 concludes all the dissertation content.

CHAPTER 2

INFLUENCE OF ZNO SOL-GEL ELECTRON TRANSPORT LAYER

PROCESSING ON BHJ ACTIVE LAYER MORPHOLOGY

AND OPV PERFORMANCE

Authors- Diego Barrera, Yun-Ju Lee, Julia W. P. Hsu

Department of Materials Science and Engineering, The University of Texas at Dallas,

800 West Campbell Rd., Richardson, TX 75080

This chapter presents the results of my first research project, “Influence of ZnO sol-gel electron transport layer processing on BHJ active layer morphology and OPV”. The surface chemistry of the underlying layer has a critical role on the morphology of the BHJ active layer. In this research we carefully studied the surface chemistry of the ZnO electron transport layer and its effect on the BHJ morphology. Our goal was to reduce the phase segregation of the active layer to improve the charge generation and decrease the bimolecular recombination, and thus, lead to a drastic improvement of OPV parameters.

The contents of this paper are adapted with permission from “**Influence of ZnO sol-gel electron transport layer processing on BHJ active layer morphology and OPV**” [Solar Energy Materials and Solar Cells, 2014, 125, 27-32]. Copyright [2014], Elsevier. The authors are Diego Barrera, Yun-Ju Lee, and Julia W. P. Hsu. My contribution was in planning and executing the experiments, analyzing the data, and writing the manuscript. Dr. Yun-Ju Lee provided careful guidance for the experiments and analysis and Prof. Julia W. P. Hsu oversaw the project and provided the careful guidance for the experiments, analysis, and manuscript writing.

2.1 Introduction and motivation

ZnO is a versatile semiconductor material, with wide range of applications in photoelectrochemical cells,⁴² lasers,⁴³ and other electrical devices.^{44,45} Due to its combination of low work function, large band gap, high crystallinity, and processability from precursor solutions,^{46,47} sol-gel ZnO films are frequently used as the electron transport layer in light emitting diodes^{48,49} and OPV devices.⁵⁰⁻⁵⁷ While ZnO nanoparticles or nanorods have been used for similar purposes,²¹ the performance of the these ZnO films depends strongly on the type and

quantity of organic additives during synthesis⁵⁸ and post-processing steps.^{59,60} Therefore, in this study we will focus on forming ZnO films by sol-gel methods because they can be synthesized in one step and are widely used. Bulk heterojunctions (BHJs) consisting of blends of poly(3-hexylthiophene) (P3HT) and phenyl-C60-butyric acid methyl ester (PCBM) represent the best characterized active layer for OPV devices. In particular, thermal annealing of P3HT:PCBM BHJs has been shown to significantly improve all aspects of device performance,⁶¹ which is attributed to optimization of BHJ morphology such that the characteristic length of the P3HT:PCBM domains match the exciton diffusion length (~ 10 nm).^{9,62,63} However, thermal annealing can create large (> 1 μm) clusters of crystalline PCBM,^{64,65} which were observed when using blends with high PCBM ratios^{66,67} or when using long annealing times.^{68,69} These clusters have been shown to lower OPV device performance due to decreased interfacial areas between P3HT and PCBM leading to poor charge collection.^{66-68,70} Nevertheless, there has not been systematic studies on the influence of the underlying layer on the formation of PCBM clusters within the BHJ. In this report, we show that detailed processing of the sol-gel ZnO films can affect the area fraction of PCBM clusters upon thermal annealing and the OPV performance. In addition, we show that removal of residual organics after pyrolysis drastically reduces the formation of PCBM clusters and improves device performance, due to a reduction in bimolecular recombination as determined by white-light biased external quantum efficiency measurements.⁷¹

2.2 Experiments

All chemicals were purchased from Fisher Scientific and were used as received unless otherwise noted. Inverted BHJ devices were fabricated on patterned indium tin oxide (ITO; 20 Ω/sq , Thin Film Devices). ZnO ETL was deposited in air using different approaches. For the first approach

(MOE ZnO), 0.5M zinc acetate dihydrate and different concentrations of MEA ranging from 0.25M to 2M (default concentration = 0.5M) were dissolved in a 2-methoxyethanol (MOE)⁴⁷ and were spin-coated at 2000 rpm and pyrolyzed at 300 °C for 10 min. Following pyrolysis, some MOE ZnO films were rinsed with pure MOE spin-coated at 2000 rpm. For the second approach (EtOH ZnO), 0.053M zinc acetate dihydrate was dissolved in ethanol without a stabilizer, and two layers were spin-coated at 1000 rpm and pyrolyzed at 150 °C for 5 min.⁷² For the BHJ, P3HT (RMI-001E, Rieke Metals, Inc.) and PCBM (Solenne BV) were dissolved in anhydrous chlorobenzene (Sigma-Aldrich) at a concentration of 25 mg/mL each, spin-coated at 1200 rpm, and annealed at 170 °C for 10 min in N₂.^{58,73} The thickness of active layer is approximately 200 nm. 5 nm MoO₃ HTL and 100 nm Ag electrode were thermally evaporated (Angstrom Engineering) to complete the devices, with area of 0.11 cm² each.

For FTIR measurements, ZnO films were deposited on 500µm *p*-type double-side polished Si(100) substrates (10-20 W cm, University Wafers). Absorbance spectra were taken at Brewster angle ($\theta = 74^\circ$), using a Thermo Scientific Nicolet iS50 FTIR spectrometer with a mercury cadmium telluride detector (MCT). Thermogravimetric analyses (TGA) were done using a TA Instruments SDT Q600 thermogravimetric analyzer in the temperature range 20–600 °C with a heating rate of 1 °C/min, with 10 ml/min of air flux into alumina crucibles. UV-vis absorbance spectra were measured for ZnO films on glass using an Ocean Optics USB QE65 Pro spectrometer. Optical images were taken using a Leica DM2500M optical microscope, and were analyzed using ImageJ. The topography was studied using an Asylum MFP-3D atomic force microscope (AFM) under tapping mode. The current density-voltage (*J-V*) curves were measured

in N₂ under a class AAA solar simulator (Sun 3000, Abet Technologies) with an AM 1.5G filter at 100 mW/cm² using a low noise source meter (2635A, Keithley). The simulator intensity was set using a NREL calibrated photodiode. For the white-light biased external quantum efficiency (EQE) measurements,⁷⁴ the devices were placed in a o-ring sealed sample holder to avoid air exposure during the time of measurement (~1.5 hour). In brief, EQE spectra were taken using a chopped monochromated light (Horiba TRIAX-180, grating 600 groove/mm) from 350 to 750 nm with a wavelength window of 3.53 nm, while a white light emitting diode (MWWHL3, Thorlabs DC 2100) provided continuous background bias with intensity ranging from 1 to 100 mW/cm².

2.3 Results and Discussion

Fig. 2.1 shows the optical microscopy images of the surface morphology of annealed P3HT:PCBM deposited over ZnO films made by two different sol-gel recipes. P3HT:PCBM annealed on top of MOE ZnO contains a large number of objects with lateral dimensions of ~ 10 μm (**Fig. 2.1a**). The size and shape of these objects are consistent with PCBM clusters previously reported for P3HT:PCBM annealed at high temperature.⁶⁷ The cluster area fraction, defined as the area occupied by PCBM clusters divided by total area as determined from image analysis, is 0.33. In contrast, P3HT:PCBM annealed at the same temperature on top of EtOH ZnO contains a much lower number of clusters (**Fig. 2.1b**), with an area fraction of 2.4×10^{-3} . A similar reduction in the area fraction of PCBM clusters can be achieved if the MOE ZnO film is rinsed with MOE before BHJ deposition (**Fig. 2.1c**), with a cluster area fraction of 0.01. **Fig. 2.1d** shows a AFM image of a PCBM cluster found in **Fig. 2.1a**, which exhibits a height of 500 nm, approximately double the thickness of a typical P3HT:PCBM active layer. The presence of

PCBM clusters suggests that the remainder of the BHJ has lower concentration of PCBM and probably a lower interfacial area between donor and acceptor. In addition, UV-vis spectroscopy showed increasing light scattering with PCBM cluster area fraction, indicating that high cluster area fraction BHJs have increased roughness, consistent with AFM data. **Fig. 2.2** shows the UV-vis absorbance spectra for various P3HT:PCBM films deposited on MOE ZnO with cluster area fraction of 0.01 (black), 0.07 (red), 0.34 (green), and 0.46 (blue). The high cluster area fraction films show significant scattering of incident light as indicated by higher absorbance for wavelengths > 650 nm, which is consistent with the large size of PCBM clusters relative to the wavelength.

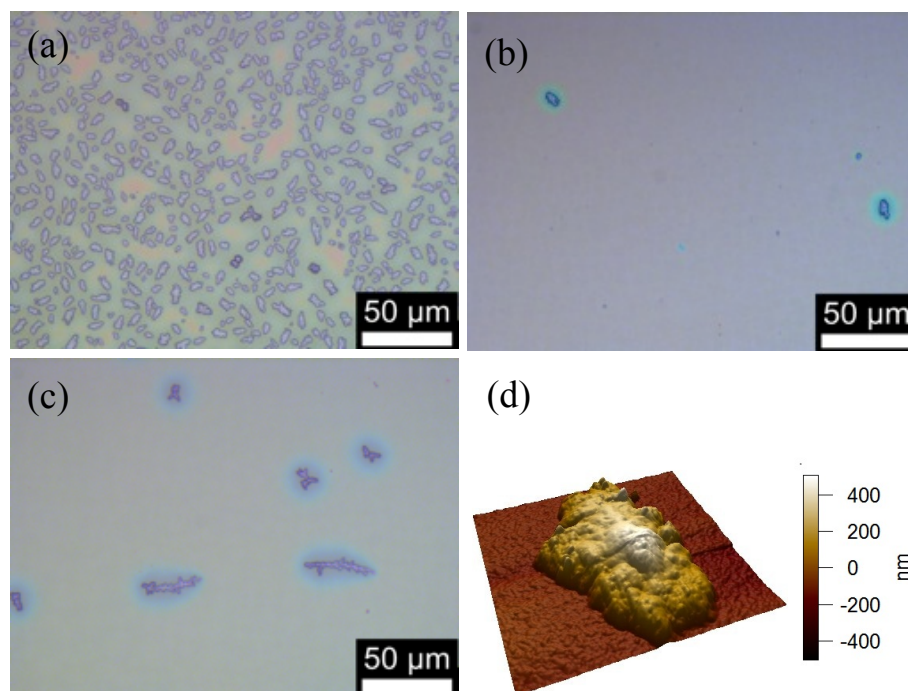


Fig. 2.1 Optical microscopic images of annealed P3HT:PCBM layer deposited on top of ZnO films made by (a) MOE ZnO, (b) EtOH ZnO, (c) rinsed MOE ZnO. (d) 5×5 μm AFM image of a typical PCBM sample.

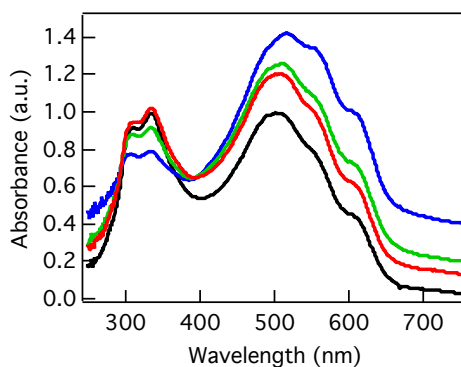


Fig. 2.2 UV-vis absorbance spectra for various P3HT:PCBM films deposited over MOE ZnO with cluster area fraction of 0.01 (black), 0.07 (red), 0.34 (green), and 0.46 (blue).

Fig. 2.3 shows cluster area fraction of the P3HT:PCBM active layer annealed on top of the MOE ZnO films as a function of MEA concentration in the precursor solution ranging from 0.25M to 2M. The data show a strong correlation between the amount of MEA in the precursor and the formation of PCBM clusters. A saturation of the cluster area fraction near 0.50 can be seen, implying a virtually complete phase separation of P3HT and PCBM since the blend consists of 50% for each component.

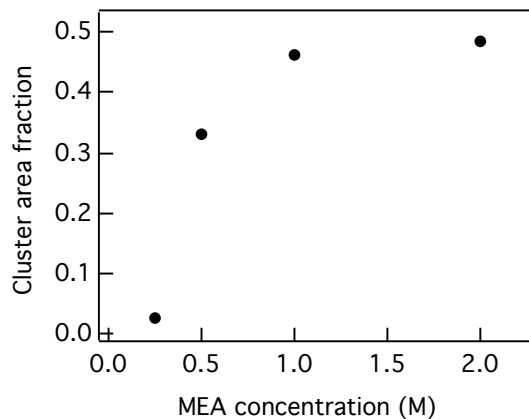


Fig. 2.3 Cluster area fraction vs MEA concentration in the precursor solution used to make MOE ZnO films, showing a positive correlation between the two parameters.

No data was shown for MEA concentrations below 0.25M because zinc acetate dihydrate did not fully dissolve at low stabilizer concentrations. Nevertheless, the ability to control cluster area fraction by varying MEA concentration allows us to systematically study the effect of cluster area fraction on device performance.

To understand the surface chemistry of MOE ZnO films, FTIR experiments were performed (**Fig. 2.4a**). MOE ZnO before pyrolysis (**Fig. 2.4a**, black) shows peaks at 1590 cm^{-1} and 1425 cm^{-1} , corresponding to asymmetric and symmetric stretching vibration of C=O mode of zinc acetate.⁷⁵ The low energy C=O peak is superimposed with the stretching vibration mode of NH group present in MEA ($\sim 1420\text{ cm}^{-1}$),⁷⁶ making a broad peak of organic species that include MEA. MOE ZnO after pyrolysis (**Fig. 2.4a**, blue, 45x amplitude) still exhibits both peaks, suggesting that most but not all of the organics were removed during pyrolysis at 300°C .

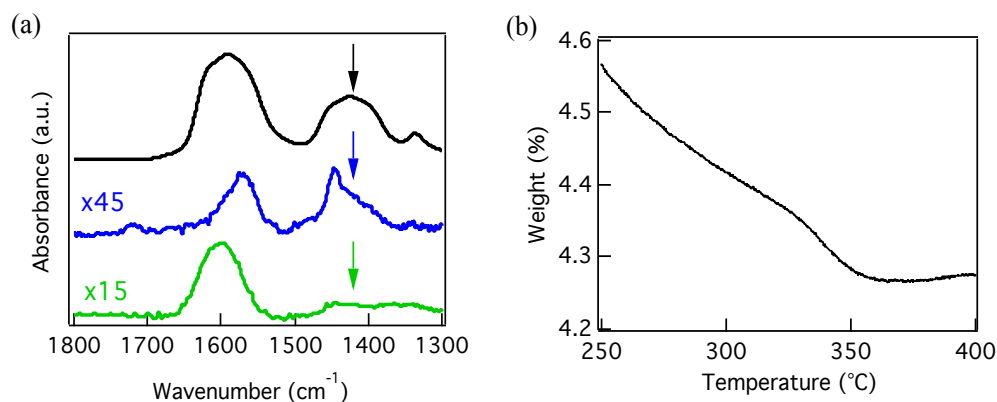


Fig. 2.4 (a) Comparison of FT-IR absorbance spectra for various MOE ZnO films: unpyrolyzed (black), pyrolyzed (blue, $\times 45$), pyrolyzed and rinsed (green, $\times 15$). The NH stretching mode at 1420 cm^{-1} is highlighted with an arrow. (b) TGA thermogram of MOE ZnO for temperature range $250\text{--}400\text{ }^\circ\text{C}$.

The presence of residual organics after the 300 °C pyrolysis of zinc acetate-MEA based ZnO sol-gel films has been reported by Fujihara et al.,⁷⁷ consistent with the TGA results (**Fig. 2.4b**) showing that weight loss continues up to 350 °C for complete decomposition of organics. However, annealing sol-gel ZnO on top of ITO up to 350°C leads to poor OPV performance due to ITO decomposition.⁷⁸ In comparison, MOE ZnO after 300°C pyrolysis and rinsing with MOE (**Fig. 2.4a**, green, 15x amplitude) shows no peaks near 1420 cm⁻¹, suggesting that MOE rinsing decreases residual organics level, most likely MEA, to below the detection limit of the MCT detector ($\sim 10^{-5}$).

Fig. 2.5 shows current density-voltage (J - V) characteristics at AM 1.5G 100 mW/cm² for devices made on top of MOE ZnO with cluster area fraction ranging from 0.01 to 0.46. Short circuit current density (J_{sc}), open circuit voltage (V_{oc}), fill factor (FF), and power conversion efficiency (PCE) values of these devices are summarized in **Table 2.1**. A clear reduction of performance in J - V curves of OPV devices as cluster area fraction increased can be seen. The black curve in **Fig. 2.5** is the device made on MOE ZnO ETL with rinsing to remove residual organics. The other devices are made on unrinsed MOE ZnO ETL. We found that PCBM clusters form in two regions: a low-density region with cluster area fraction ≤ 0.10 and a high-density region with cluster area fraction ≥ 0.30 . In all devices used in this study (~ 120), we did not observe PCBM cluster area fraction between 0.10 and 0.30, indicating two different cluster formation mechanisms. In the low-density region, cluster formation was probably triggered by surface imperfections or dusts located randomly on the ZnO film (**Fig. 2.1b** and **Fig. 2.1c**). In the high-density region, the cluster formation arose from a much more uniform distributed source,

possibly the residual organics (**Fig. 2.1a**). The gap between these two regions indicates an instability in the cluster formation.

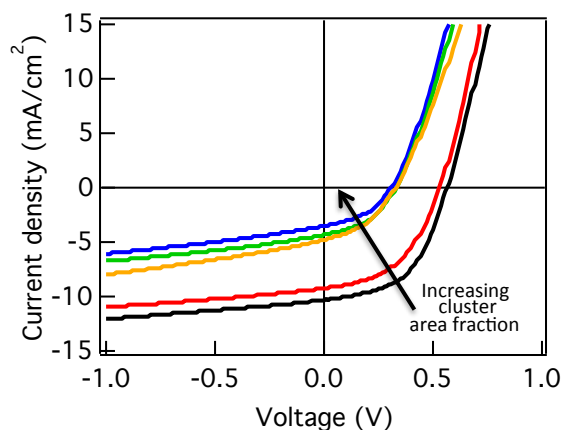


Fig. 2.5 J - V characteristics of solar cells under 100 mW/cm^2 AM 1.5G illumination for devices with different cluster area fraction: 0.01 (black), 0.06 (red), 0.34 (orange), 0.39 (green), and 0.46 (blue).

Table 2.1 Summary of the device performance parameter dependence on cluster area fraction obtained from J - V characteristics of solar cells taken under 100 mW/cm^2 AM 1.5G illumination. Series resistance (R_{se}) and shunt resistance (R_{sh}) were calculated from J - V characteristics measured in the dark.

Cluster area fraction	V_{oc} (V)	J_{sc} (mA/cm^2)	FF (%)	PCE (%)	R_{se} ($\Omega \text{ cm}^2$)	R_{sh} ($\Omega \text{ cm}^2$)
0.01	0.563 ± 0.005	10.32 ± 0.17	0.518 ± 0.022	3.01 ± 0.10	11 ± 2	5399 ± 476
0.06	0.532 ± 0.013	9.24 ± 0.33	0.474 ± 0.006	2.33 ± 0.16	9 ± 2	4807 ± 1631
0.34	0.328 ± 0.038	4.79 ± 0.89	0.402 ± 0.006	0.64 ± 0.21	19 ± 4	2871 ± 1173
0.39	0.330 ± 0.037	4.32 ± 0.92	0.424 ± 0.012	0.62 ± 0.22	14 ± 3	15088 ± 935
0.46	0.310 ± 0.014	3.51 ± 0.22	0.416 ± 0.015	0.45 ± 0.05	18 ± 4	4930 ± 1168

The performance of EtOH ZnO devices is similar to rinsed MOE ZnO devices. **Fig. 2.6** represents J - V characteristics of rinsed MOE ZnO (**Fig. 2.6**, black) and EtOH ZnO devices (**Fig. 2.6**, blue). The OPV parameters for both devices are summarized in **Table 2.2**. However, the EtOH ZnO ETL is less reliable due to poor stability of zinc acetate dehydrate in EtOH without stabilizer, which limits maximum solubility to 0.053M and causes precipitation over a period of

several hours, making it difficult to reproducibly deposit of a ZnO films with suitable thickness (~40 nm) without pinholes or aggregates.

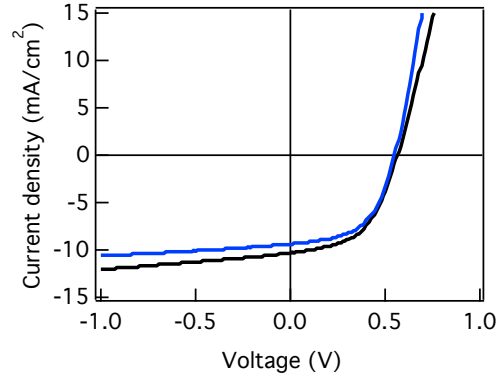


Fig. 2.6 Comparison between MOE ZnO rinsed (black) and EtOH ZnO (blue) on J - V characteristics of solar cells under 100 mW/cm^2 AM 1.5G illumination.

Table 2.2 Summary of the device performance parameter of rinsed MOE ZnO and EtOH ZnO obtained from J - V characteristics of solar cells measured under 100 mW/cm^2 AM 1.5G illumination.

Sample	V_{oc} (V)	J_{sc} (mA/cm ²)	FF (%)	PCE (%)	R_{se} ($\Omega \text{ cm}^2$)	R_{sh} ($\Omega \text{ cm}^2$)
rinsed MOE ZnO	0.563 ± 0.005	10.32 ± 0.17	0.518 ± 0.022	3.01 ± 0.10	11 ± 2	5399 ± 476
EtOH ZnO	0.550 ± 0.000	9.36 ± 0.27	0.543 ± 0.023	2.80 ± 0.13	7 ± 2	5937 ± 1976

The dependence of J_{sc} , V_{oc} , FF, PCE, R_{se} , and R_{sh} on cluster area fraction is depicted in **Fig. 2.7**. As noticed before, the dependence of device parameters on cluster area fraction can be divided into the same low and high cluster area fraction regions. Note that for cluster area fraction between 0.30 and 0.40, the results show larger standard deviation within a sample as well as sample-to-sample variation. This is consistent with cluster formation being unstable and minute differences leading to large variations in cluster area fraction. Despite some variations in the results, a clear trend is observed: the performance of the devices reflected on all four parameters decreases with increasing cluster area fraction. For cluster area fraction ≤ 0.1 , the devices work

well with average values of J_{sc} , V_{oc} , FF, and PCE of 9.7 ± 0.5 mA/cm², 0.55 ± 0.02 V, 0.47 ± 0.03 , and 2.5 ± 0.3 %, respectively, over 25 devices.

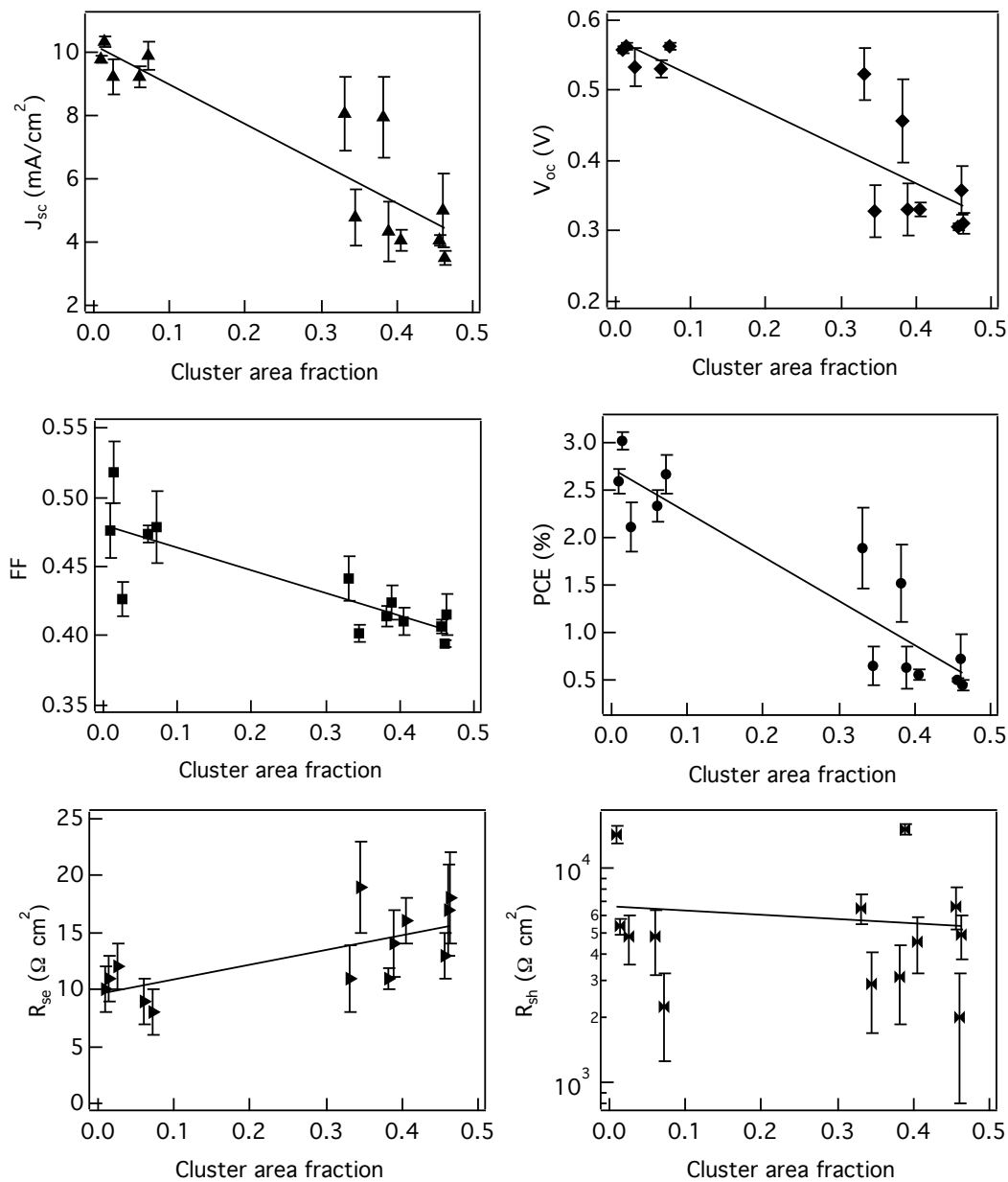


Fig. 2.7 Influence of cluster area fraction on OPV device parameters.

OPV device parameters with the cluster area fraction ≥ 0.3 show reductions of up to 45% in J_{sc} , up to 35% in V_{oc} , up to 15% in FF, and up to 65% in PCE compared to devices with cluster area fraction ≤ 0.1 . R_{se} increases gradually with respect to cluster area fraction, whereas there is a very little correlation between R_{sh} and cluster area fraction. Similar reductions in the OPV device parameters has been reported by van Bavel et al. for BHJ devices with PCBM clusters forming due to high PCBM concentrations,⁶⁶ although their analysis is complicated by the effect of PCBM concentration on performance.

Fig. 2.8 shows J_{sc} values at 100 mW/cm² integrated from EQE spectra ($J_{sc}(EQE^*)$) measured at different white-light bias intensities⁷¹ for P3HT:PCBM devices on MOE ZnO with cluster area fraction of 0.01 (black, achieved by rinsing), 0.33 (red), and 0.46 (blue). $J_{sc}(EQE^*)$ represents the expected J_{sc} value of a device under AM1.5G 100 mW/cm² illumination for different levels of bimolecular recombination, which we control by varying the background white-light intensity and hence the carrier density inside the BHJ. It is evident that devices with high cluster area fraction (**Fig. 2.8**, red and blue) exhibit significantly lower $J_{sc}(EQE^*)$ compared to the device with low cluster area fraction (**Fig. 2.8**, black) even at low background intensities, where bimolecular recombination is negligible, indicating that the presence of PCBM clusters in BHJs decreases carrier generation. This is likely caused by a lower degree of interpenetration between P3HT and PCBM. When $J_{sc}(EQE^*)$ at 100 mW/cm² background intensity is compared to the average value of $J_{sc}(EQE^*)$ at low intensities (**Fig. 2.8**, dashed lines), a significantly greater reduction of performance is observed for devices with high cluster area fraction. For example, the device with 0.01 cluster area fraction exhibits a 2.6% decrease in $J_{sc}(EQE^*)$ at 100 mW/cm²,

while the devices with cluster area fractions of 0.33 and 0.46 exhibited decreases of 29% and 27%, respectively. This indicates that devices with high cluster area fraction experience higher bimolecular recombination, possibly caused by inefficient carrier transport in the non-aggregated regions of the active layer. We also found that after white-light biased EQE measurements, devices with high cluster area fraction degraded significantly, while devices with low cluster area fraction showed no significant change.

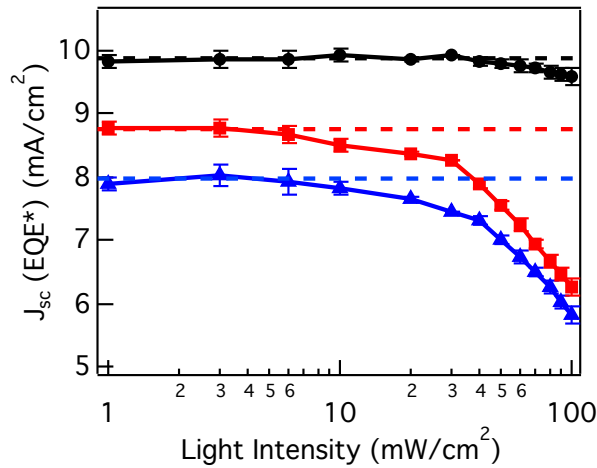


Fig. 2.8 Current density integrated from EQE spectra, J_{sc} (EQE^*), at different background intensities for P3HT:PCBM devices on MOE ZnO with cluster area fraction of 0.01 (black), 0.33 (red), and 0.46 (blue). Dashed lines represent average J_{sc} (EQE^*) value at < 10 mW/cm² background intensity for each device.

Fig. 2.9 depicts J - V characteristics of a 0.01 cluster area fraction device before (black lines) and after (black dashed lines) white-light biased EQE measurements, showing no change. In contrast, the 0.38 cluster area fraction device (**Fig. 2.9**, red) showed clear reduction in J_{sc} , V_{oc} , FF, and PCE after EQE measurement, indicating that these type of devices are susceptible to degradation.

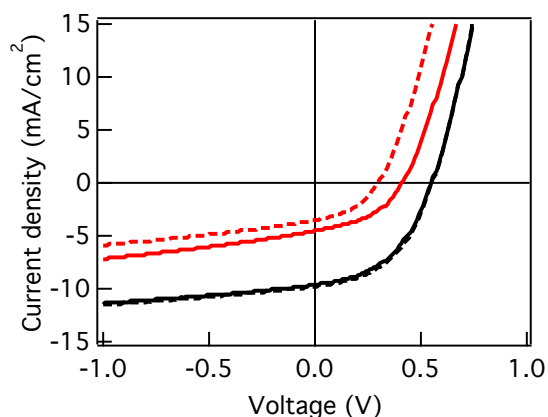


Fig. 2.9 Effect of cluster area fraction on performance reduction of solar cells taken under 100 mW/cm^2 AM 1.5G illumination: before (solid line) and after (dashed line) white-light biased EQE measurements for a 0.01 cluster area fraction device (black) and a 0.38 cluster area fraction device (red).

The OPV parameters for both devices before and after EQE measurements are summarized in **Table 2.3**. Thus, low cluster area fraction in P3HT:PCBM BHJs, which can be achieved by rinsing the pyrolyzed MOE ZnO surface to remove residual organics (**Fig. 2.8**, black), results in improved device performance and stability both from increased charge generation and reduced bimolecular recombination.

Table 2.3 Summary of the device performance parameter change before and after white-light EQE measurements for devices with two different cluster area fractions.

Sample	V_{oc} (V)	J_{sc} (mA/cm^2)	FF (%)	PCE (%)	R_{se} ($\Omega \text{ cm}^2$)	R_{sh} ($\Omega \text{ cm}^2$)
Before EQE	0.555 ± 0.005	9.77 ± 0.20	0.475 ± 0.020	2.57 ± 0.16	9 ± 2	3406 ± 1395
After EQE	0.553 ± 0.008	9.63 ± 0.24	0.463 ± 0.026	2.48 ± 0.21	9 ± 2	3326 ± 1471
Before EQE	0.414 ± 0.013	4.52 ± 0.31	0.430 ± 0.007	0.81 ± 0.07	10 ± 2	3800 ± 1443
After EQE	0.296 ± 0.011	3.51 ± 0.23	0.421 ± 0.013	0.44 ± 0.05	10 ± 2	3442 ± 370

2.4 Conclusions

In summary, we demonstrate the influence of the underlying layer on the BHJ layer morphology. We show that trace amount of organic species, most likely MEA, on the pyrolyzed MOE ZnO surface has a significant effect on the morphology of P3HT:PCBM BHJ films. When the active layer is deposited and annealed over a sol-gel ZnO ETL surface made from MEA containing precursor, PCBM clusters form during annealing, with cluster area fraction correlated with the MEA concentration in the precursor solution. This phase segregation leads to a reduction of interfacial area and lower PCBM concentrations outside of the clusters in the active layer, resulting in drastic reduction of OPV parameters due to both low charge generation and high bimolecular recombination. Rinsing the pyrolyzed MOE ZnO films with MOE or using a ZnO recipe without MEA significantly reduced the formation of PCBM clusters and produced devices with good performance and better stability.

CHAPTER 3
IN SITU CHEMICAL OXIDATION OF ULTRASMALL MoO_x
NANOPARTICLES IN SUSPENSION

Authors- Yun-Ju Lee, Diego Barrera, Kaiyuan Luo, and Julia W. P. Hsu
Department of Materials Science and Engineering, The University of Texas at Dallas,
800 West Campbell Rd., Richardson, TX 75080

The synthesis of new materials as transport layer suitable for low-temperature processing and large-area deposition is essential to continue the advance of the OPV technology. This chapter summarizes the results of our studies on the synthesis of MoO_x nanoparticle suspensions with controlled size and electronic properties using oxidative dissolution of organometallic powders with H₂O₂. This MoO_x nanoparticle suspension can potentially substitute its thermally evaporate counterpart enabling large-area deposition, one of the key assets of OPV.

The contents of this paper are adapted with permission from “**In Situ Chemical Oxidation of Ultrasmall MoO_x nanoparticles in suspension**” [Journal of Nanotechnology, 2012, 195761]. Copyright [2012], Hindawi. The authors are Yun-Ju Lee, Diego Barrera, Kaiyuan Luo, and Julia W. P. Hsu. My contribution was in synthesis and characterization of the material, and analyzing the data. Dr. Yun-Ju Lee provided careful guidance for the experiments and manuscript writing. Kaiyuan Luo contribution was data analysis and synthesis discussion. Prof. Julia W. P. Hsu provided the careful guidance for the experiments, analysis, and manuscript writing.

3.1 Introduction and motivation

Metal oxide nanoparticles represent a large class of materials with applications in areas such as energy conversion and storage,^{11,79} catalysis,^{80,81} sensing,⁸² and biomedicine.⁸³ Major advantages of metal oxide nanoparticle suspensions include compatibility with low-temperature, large-area solution processing, and versatile surface functionalization.⁷⁹ Molybdenum oxide (MoO_x) has attracted much interest as a HTL material in organic light emitting diodes and solar cells because of its high work function (Φ). By matching Φ of the HTL to the highest occupied molecular

orbital (HOMO) of the organic electron donor material,⁸ MoO_x films inserted between the active layer and the anode has been shown to improve performance of organic photovoltaic (OPV) devices.^{14,23,54,84-88} Most work in this area use thermally evaporated MoO_x films.^{54,84-86} While solution deposition of MoO_x HTL films has been reported, all approaches thus far have required a post-deposition processing step that must be performed either at high temperature (≥ 160 °C)^{14,87,88} and/or in an O₂-containing ambient²³ to obtain MoO_x films with high Φ . In addition, the solvents currently used for the solution deposition of MoO_x do not wet the organic layer to form a uniform thin film as required in an inverted OPV architecture, which shows superior stability in air compared to conventional devices.^{89,90} Recently, our group developed a microwave-assisted synthesis of MoO_x nanoparticles (npMoO_x) in n-butanol suspension, demonstrated formation of uniform thin films on P3HT:PCBM blends using room-temperature solution processing, and examined performance of inverted OPV devices using npMoO_x films as HTLs.⁹¹ Here we focus on *in situ* chemical oxidation to optimize the npMoO_x properties for HTL application. Specifically, we examined the effect of chemical oxidation conditions on the size and stability of the npMoO_x suspension to evaluate its suitability for the formation of uniform and pinhole free thin films. We also quantified the impact of chemical oxidation on Φ and stoichiometry MoO_x thin film, and demonstrated continuous tuning of Φ from 4.4 eV to 5.0 eV through precise control of the chemical oxidation conditions and Mo oxidation state. We show that *in situ* chemical oxidation of MoO_x nanoparticle is a versatile technique to synthesize stable suspensions of ultrasmall nanoparticles with desired stoichiometry and Φ for the formation of thin HTL on top of organic active layer without post processing.

3.2 Experiments

MoO_x nanoparticle (npMoO_x) suspensions were synthesized using nonhydrolytic sol-gel conversion of molybdenum dioxide bis(acetylacetonate) (Moacac) in anhydrous n-butanol as shown schematically in **Fig. 3.1**, following a microwave-assisted synthesis procedure modified from Bilecka and co-workers.⁹² We selected this approach because it has been shown to yield various metal oxide nanoparticles with low size polydispersity, good stability, and short reaction times down to 3 min. Furthermore, the procedure does not require additional ligands for nanoparticle stabilization, and thus should allow the deposition of nanoparticle films with good carrier transport properties without the need to remove electrically insulating ligands through a post synthesis step. We used n-butanol as the solvent because of the good solubility for Moacac, and because it wets, but does not dissolve or swell, hydrophobic organic films such as P3HT:PCBM. For the microwave synthesis, a test tube of Moacac solution in n-butanol was mixed in N₂ and placed in a microwave reactor (CEM Discovery) containing a single mode 2.54 GHz microwave cavity. A Moacac concentration of 0.1 M was selected to balance complete dissolution and strong absorption microwave to enable rapid heating to 200 °C within three minutes. The Moacac solution was maintained at 200 °C for 15 min to synthesize the brown npMoO_x suspension (**Fig. 3.1**). We chose to chemically oxidize npMoO_x in suspension using H₂O₂ for three reasons: H₂O₂ is a strong oxidizing agent, H₂O₂ is miscible with n-butanol, and byproducts of the reaction, e.g. H₂O and O₂, can be easily removed during subsequent processing. For chemical oxidation, a small amount of 30 wt.% H₂O₂ in H₂O (Fisher) was added to the npMoO_x suspension to achieve the desired concentration (for example, 10.2 μL of 30 wt.%

H₂O₂ in H₂O per mL of suspension for 0.1 M H₂O₂). The mixture was then stirred at room temperature for times ranging from 20 min to 24 h for oxidation to occur.

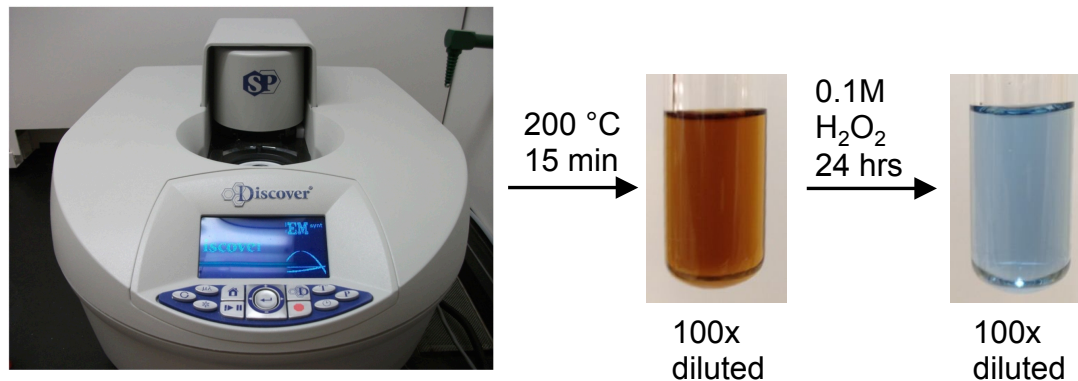


Fig. 3.1 Picture of microwave synthesis and chemical oxidation of MoO_x nanoparticles. A mixture of molybdenum oxide bis(acetylacetonate) in n-butanol was placed in a microwave reactor (CEM Discovery) and heated using 2.45 GHz radiation. When heated at 200 °C for 15 minutes, Moacac reacted, forming a brown suspension of nanoparticles. Chemical oxidation of the nanoparticle suspension with 0.1M H₂O₂ for 24 hours yielded a blue suspension of nanoparticles.

To determine the nanoparticle size and distribution, an aliquot of each npMoO_x suspension was diluted by a factor of 10 with n-butanol, agitated in an ultrasonic bath (Branson) for 5 min, and passed through a 0.2 μm PTFE syringe filter. The diluted suspension was analyzed by dynamic light scattering (DLS) under backscattering conditions using a Malvern Zetasizer. To form thin films for these measurements, the npMoO_x suspension without dilution was passed through a 0.2 μm PTFE syringe filter and spin coated at 1000 rpm on a cleaned ITO coated glass (20 Ω/□, Thin Film Devices). Φ of the MoO_x film was measured using the Kelvin probe technique, and oxidation state of the Mo cation was determined using X-ray photoelectron spectroscopy (XPS). Φ of the npMoO_x film was measured in air using an isoprobe electrostatic voltmeter (Model 244, Monroe Electronics), with Au as the reference material ($\Phi = 5.15$ eV). XPS of the npMoO_x film

was carried out using a Perkin-Elmer 5600 ESCA system with monochromated Al KR source (1486.7 eV). All spectra were collected at an angle of 45° to the sample normal, with a pass energy of 58.7 eV and energy step of 0.125 eV. All XPS spectra were fitted using commercial software (MultiPak, PHI) and aligned to the C 1s reference at 284.8 eV. A reference sample of 20 nm MoO₃ on ITO was made by thermal evaporation at a rate of 0.1 Å/s. A FWHM of 1.2 eV for each peak was used for peak fitting.

3.3 Results and Discussion

We found that microwave heating of Moacac resulted in a brown suspension of npMoO_x (**Fig. 3.1**). Even without added ligands, the suspension showed excellent stability and remain dispersed for more than 90 days. DLS of the as-synthesized npMoO_x suspension found a volume weighted mean diameter of 2.1 ± 0.9 nm (**Fig. 3.2a**, dashed line), in good agreement with the size determined using small-angle x-ray scattering (SAXS).⁹¹ Storage of the as-synthesized npMoO_x in air for up to 120 hours led to no change in size, as confirmed by DLS (data not shown). In contrast, we found that chemical oxidation with H₂O₂ modified the size of the resulting nanoparticles in a complex way (**Fig. 3.2a**). For example, 0.1M (**Fig. 3.2a**, blue) and 0.3M (**Fig. 3.2a**, red) H₂O₂ at short reaction times ranging from 20 min to 3 h decreased the npMoO_x diameter to ~ 1 nm. In comparison, a further increase in reaction time to 24 h caused the nanoparticle size to increase back to 2 nm. The increase in size with longer reaction time is consistent with our previous observation that the average diameter of chemically oxidized npMoO_x from SAXS had increased to 4 nm after ~ 15 days of chemical oxidation,⁹¹ and indicates that Ostwald ripening for these nanoparticles only occurs with the addition of H₂O₂. Nevertheless, the nanoparticles are still small enough to form multilayer films with thickness of

~ 10 nm. Indeed, we previously showed using atomic force microscopy that a chemically oxidized MoO_x suspension spin coated on top of P3HT:PCBM formed a pinhole-free film that planarized the roughness of the underlying P3HT:PCBM layer.⁹¹ Thus, while npMoO_x size increases after chemical oxidation with H₂O₂, it remains sufficiently small to form uniform films on top of organic layers at thickness values that are relevant for HTL in OPV devices.

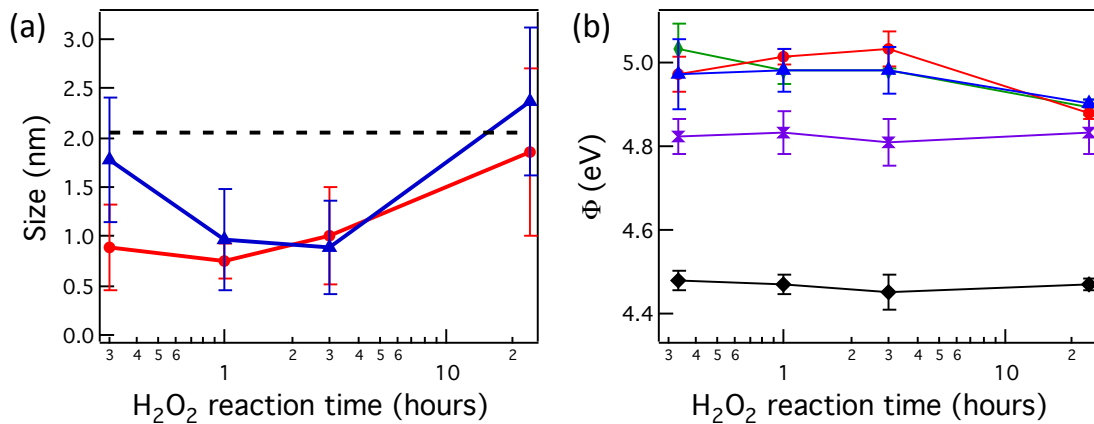


Fig. 3.2 Effect of chemical oxidation with H₂O₂ on MoO_x nanoparticle properties. a) Dependence of nanoparticle size on chemical oxidation time (up to 24 h), showing that compared to as-synthesized nanoparticles (dashed line), both 0.1M H₂O₂ (blue) and 0.3M caused npMoO_x size to decrease to 1 nm (up to 3 h) and then increase back to 2 nm (24 h). b) Dependence of nanoparticle film Φ versus chemical oxidation conditions, showing Φ of as-synthesized npMoO_x (black) was increased from 4.48 eV to 4.85 eV with 0.05M H₂O₂ (purple) and that the increase was independent of the reaction time between 20 min and 24 hr. In contrast, 0.1M (blue), 0.2M (green), and 0.3M (red) H₂O₂ all caused work function to increase to 5.0 eV with a reaction time of up to 3 hr. However, a further increase in reaction time to 24 h decreased Φ to 4.9 eV.

Chemical oxidation of the MoO_x nanoparticles significantly altered the electronic properties of npMoO_x films, as measured by their Φ values in air. The as-synthesized npMoO_x films exhibited a low Φ of 4.48 ± 0.02 eV. Addition of 0.05M H₂O₂ for 20 min caused Φ to increase to 4.82 ± 0.04 eV, and longer reaction times did not significantly increase Φ (**Fig. 3.2b**, purple). Increasing

H₂O₂ concentration to 0.1M and above caused Φ to increase to 4.94 ± 0.01 eV after 1 h, and the value remained unchanged when increasing the reaction time to 3 h (**Fig. 3.2b**). However, a further increase in reaction time to 24 h caused Φ to decrease to 4.90 ± 0.01 eV. We note that the decrease in Φ corresponded to the change of the nanoparticle suspension color from brown to blue (**Fig. 3.1**).

To quantitatively understand the origin of the change in Φ with chemical oxidation, we examined the stoichiometry of npMoO_x films with different H₂O₂ reaction conditions using XPS. As a reference, we measured an evaporated MoO₃ film and found that the Mo 3d XPS spectra can be fitted to doublet peaks at 232.3 eV and 235.4 eV, corresponding to Mo 3d_{5/2} and Mo 3d_{3/2} peaks for Mo⁶⁺, plus very weak doublet peaks at 231.0 eV and 233.8 eV corresponding to Mo 3d_{5/2} and Mo 3d_{3/2} peaks for Mo⁵⁺.⁹¹⁻⁹³ The Mo⁶⁺ fraction, defined as the area under the Mo⁶⁺ peaks divided by the total peak area, was 0.95, indicating that the reference sample was almost pure MoO₃. The FWHM of the fitted peaks was 1.2 eV, and this value was used for all peaks when fitting XPS spectra of npMoO_x films where there are significant contributions to the overall signal from multiple oxidation states, in order to quantify the atomic fraction from each oxidation state. For example, the Mo 3d XPS spectra of as-synthesized npMoO_x contain peaks at 232.4 eV and 235.5 eV from Mo⁶⁺, 231.4 eV and 234.5 eV from Mo⁵⁺, and 229.8 eV and 232.9 eV from Mo⁴⁺ (**Fig. 3.3a**). The Mo⁶⁺ fraction was 0.21, showing that as-synthesized npMoO_x is mostly reduced. Reaction with 0.05M H₂O₂ for 1 h caused the Mo⁶⁺ peaks to increase in intensity at the expense of the Mo⁵⁺ and Mo⁴⁺ peaks (**Fig. 3.3b**), so that the Mo⁶⁺ fraction increased to 0.60. Nevertheless, the XPS spectra clearly show that 0.05M H₂O₂ only partially oxidized the as

synthesized MoO_x nanoparticles to MoO_3 . Increasing the H_2O_2 concentration to 0.1M resulted in Mo 3d XPS spectra consisting almost entirely of peaks at 232.6 eV and 235.7 eV from Mo^{6+} , with a miniscule contribution from Mo^{5+} peaks at 230.9 eV and 234.1 eV (**Fig. 3.3c**).

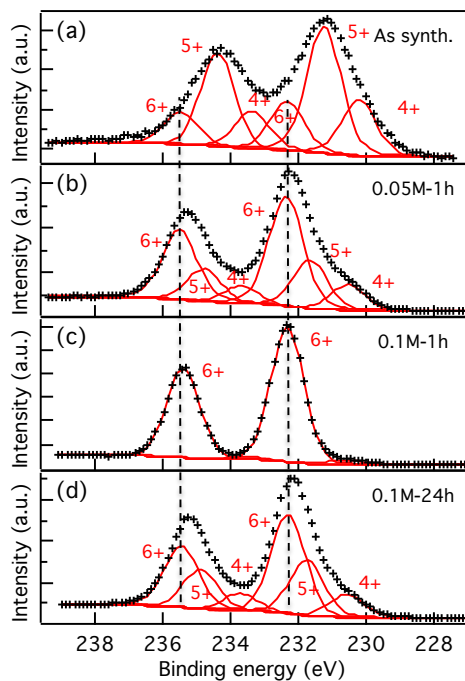


Fig. 3.3 Effect of chemical oxidation conditions on MoO_x nanoparticle stoichiometry. a) Mo 3d XPS spectra of as-synthesized npMoO_x on ITO (crosses) and curve fit (solid), showing mixed oxidation states with contributions from Mo^{5+} , Mo^{4+} , and a small amount of Mo^{6+} . b) Mo 3d XPS spectra of npMoO_x after chemical oxidation with 0.05M H_2O_2 for 1 h, showing mixed oxidation states with a majority of Mo^{6+} oxidation state. c) Mo 3d XPS spectra of npMoO_x after chemical oxidation with 0.1M H_2O_2 for 1 h, showing almost complete oxidation to Mo^{6+} oxidation state. d) Mo 3d XPS spectra of npMoO_x after chemical oxidation with 0.1M H_2O_2 for 24 h, showing mixed oxidation states with a majority of Mo^{6+} oxidation state.

The corresponding Mo^{6+} fraction of 0.97 indicates that 0.1M H_2O_2 for 1 h oxidized npMoO_x to the extent similarly to the evaporated MoO_3 film. Increasing the reaction time to 24 h at 0.1M H_2O_2 caused the Mo^{5+} and Mo^{4+} peaks to reappear in the Mo 3d XPS spectra (**Fig. 3.3d**), decreasing the Mo^{6+} fraction to 0.55. We believe the partial reduction of npMoO_x with increased

H₂O₂ reaction time can be explained by the electrochromism of MoO₃. MoO₃ is known to change to a blue coloration upon the insertion of small cations such as H⁺, following the reaction⁹⁴



In our case, H⁺ is supplied by the H₂O in the 30 wt% H₂O₂ solution, and e⁻ may be supplied by oxidation of neighboring Mo⁴⁺ and Mo⁵⁺ atoms. This reaction scheme is consistent with the observation that the change in npMoO_x coloration from brown to blue was only observed after 24 hr reaction with 0.1M and 0.3M H₂O₂. The onset of color change, and by reference the proton insertion, also coincides with the increase in nanoparticle size and reduction in Φ. Thus, analysis of XPS spectra reveals that chemical oxidation with H₂O₂ consists of two concurrent processes, a fast oxidation that is complete at 0.1M and higher H₂O₂ concentrations within ~ 1 h, and a slow reduction caused by H⁺ insertion that occurs after ~ 24 h, highlighting the importance of the chemical oxidation conditions on the stoichiometry of the resulting npMoO_x.

Fig. 3.4 shows the O 1s and C 1s regions of the XPS spectra for npMoO_x films with different H₂O₂ reaction conditions. Deconvolution of the O 1s XPS spectra of as-synthesized npMoO_x contains a strong peak attributed to oxides at 530.4 eV, and a second peak at 531.9 eV attributed to adsorbed oxygen species.⁹³ Both peaks attributed to oxides and chemisorbed oxygen remained constant for all synthesis conditions. In the C 1s XPS spectra, the as-synthesized npMoO_x exhibited a strong peak at 284.8 eV from C- C and C-H bonds, likely due to hydrocarbon contamination from air exposure. Also, a small contribution from the carbon-oxygen bond at ~ 285.7 eV.⁹³ All npMoO_x films in this study had the same, or very similar C1s binding energies

regardless of the oxidation conditions, indicating that increasing the H_2O_2 concentration was not reflected on the carbon content of the npMoO_x films, as expected.

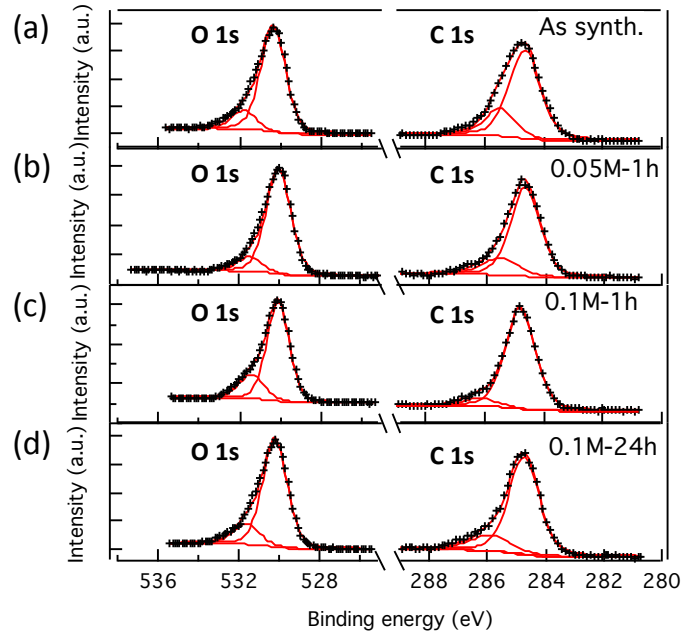


Fig. 3.4 O 1s and C 1s regions of XPS spectra for MoO_x nanoparticle films with different H_2O_2 reaction conditions: a) as-synthesized npMoO_x . b) npMoO_x after chemical oxidation with 0.05M H_2O_2 for 1 h. c) npMoO_x after chemical oxidation with 0.1M H_2O_2 for 1 h. d) npMoO_x after chemical oxidation with 0.1M H_2O_2 for 24 h.

Fig. 3.5 depicts Φ and Mo^{6+} fraction that can be achieved using the *in situ* H_2O_2 chemical oxidation approach. For npMoO_x films that were chemically oxidized at different H_2O_2 concentrations for 1 h (**Fig. 3.5**, circles) and at 0.1M H_2O_2 for 24 h (**Fig. 3.5**, triangle), the data show a strong correlation between the two parameters, suggesting that a clear relationship exists between MoO_x nanoparticle stoichiometry and electronic properties. A continuous tuning of the Mo^{6+} fraction between 0.2 and 1.0, and Φ from 4.4 eV to 5.0 eV was achieved. Such control should allow us to systematically study the effect of MoO_x composition on device performance in various applications.

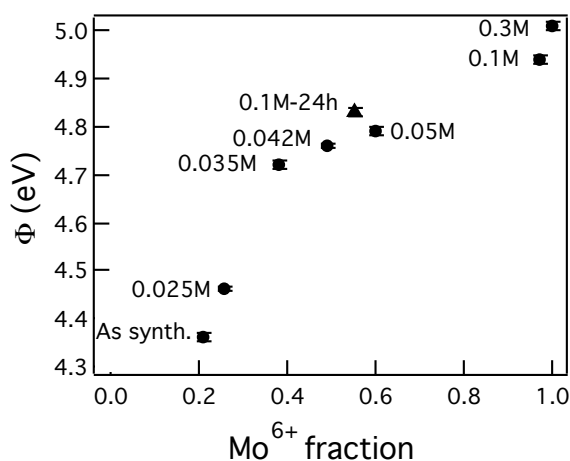


Fig. 3.5 Φ versus Mo^{6+} fraction for npMoO_x as synthesized and chemically oxidized at 0.025M, 0.035M, 0.042M, 0.05M, 0.1M, and 0.3M H_2O_2 concentrations for 1 h (circles) and at 0.1M H_2O_2 for 24 h (triangle), showing a positive correlation between the two parameters.

3.4 Conclusions

In conclusion, through a systematic study of the effect of H_2O_2 concentration and reaction time on nanoparticle size, Φ , and stoichiometry, we demonstrate that *in situ* chemical oxidation of MoO_x nanoparticle suspensions with H_2O_2 is a simple but versatile method to control their stoichiometry and electronic properties. Starting from suspensions of ultrasmall ($d \sim 2$ nm) MoO_x nanoparticles in n-butanol synthesized by a one-step microwave heating procedure, we found that short time (≤ 3 h) reactions at room temperature with sufficiently high (≥ 0.1 M) concentration of H_2O_2 result in ≤ 1 nm MoO_x nanoparticles with high Φ and almost entirely MoO_3 , properties which are desirable for HTL material in OPV devices. However, long chemical oxidation times (≥ 24 h) increase nanoparticle size and reduce Mo oxidation state and film's work function. By comparing Kelvin probe results and XPS spectra of npMoO_x films that have been chemically oxidized under various conditions, we established a clear correlation between

the Φ and the Mo^{6+} fraction of the npMoO_x , and achieved a continuous tuning of Φ values from 4.4 to 5.0 eV and Mo^{6+} fraction from 0.2 to 1.0. Such precise control of MoO_x stoichiometry and properties is crucial for the optimization of npMoO_x as a solution processible material for various applications. Moreover, the simplicity of the chemical oxidation procedure should be generally applicable in synthesizing other transition oxide nanomaterials with tunable stoichiometry and properties.

CHAPTER 4
SOLUTION SYNTHESIS OF FEW-LAYER
2H MX₂ (M= Mo,W; X= S,Se)

Authors- Diego Barrera, Qingxiao Wang, Yun-Ju Lee, Lanxia Cheng, Moon J. Kim, Jiyoung

Kim, and Julia W. P. Hsu

Department of Materials Science and Engineering, The University of Texas at Dallas,

800 West Campbell Rd., Richardson, TX 75080

Two-dimensional transition metal dichalcogenides (TMDs) exhibit a wide range of properties depending on the chemistry of the transition metal element and the chalcogen, making them promising candidates for electronic applications. Current TMD thin films are either derived from bulk minerals, hence limited by the impurities, defects, and the availability of raw materials, or deposited using high vacuum or high reaction temperature processes. This chapter summarizes the results of our efforts using a versatile method used to synthesize few-layer 2H MoS₂, MoSe₂, WS₂, and WSe₂ flakes from thermolysis of organometallic precursor in the presence of chalcogen. We study how the concentration of reducing agent, 1,2-hexadecanediol, affects the TMDs' chemical composition using X-ray photoelectron spectroscopy (XPS).

The contents of this paper are submitted as a paper entitled “**Solution synthesis of few-layer 2H MX₂ (M= Mo,W; X= S,Se)**”, currently under review. The authors are Diego Barrera, Qingxiao Wang, Yun-Ju Lee, Lanxia Cheng, Moon J. Kim, Jiyoung Kim, and Julia W. P. Hsu. My contribution was in planning and executing the synthesis and characterization of the materials, analyzing the data, and writing the manuscript. Qingxiao Wang performed the scanning transmission electron microscopy (STEM) characterization of the TMDs. Dr. Yun-Ju Lee provided careful guidance for the experiments and fruitful discussions. Lanxia Cheng performed the Raman characterization on the materials. Prof. Moon J. Kim and Prof. Jiyoung Kim provided insightful discussion on STEM and Raman results. Prof. Julia W. P. Hsu oversaw the project and provided the careful guidance for the experiments, analysis, and manuscript writing.

4.1 Introduction and motivation

Two-dimensional (2D) TMDs are highly anisotropic layered, graphene-like compounds that have attracted great interest in basic and applied research due to a wide range of electronic, optical, mechanical and thermal properties. These materials have the formula MX_2 , where M is a transition metal element from group IV, V, or VI, and X is a chalcogen (S, Se or Te). They form layered structures of the form X-M-X, with the chalcogen atoms in two hexagonal planes separated by a plane of metal atoms. TMD materials exist in bulk form as stacks of strongly in-plane bonded layers with weak van der Waals-like interlayer attraction at the X-X interface, allowing exfoliation into atomically thin layers.³⁰ Researchers are now turning to TMDs as ultrathin materials with tunable bandgaps and extraordinary conductivity, making them highly applicable in solar cells,⁹⁵⁻⁹⁷ catalysis,⁹⁸ transistors,^{29,99-103} and photodetectors.^{34,104}

The common methods to obtain mono- and few-layer TMDs are exfoliation from bulk crystals,^{29,30,34,95,105-110} growth on substrates,^{99,100,111-116} and colloidal synthesis from metal and chalcogenide precursors.^{38,117-120} Liquid exfoliation enables preparation of atomically thin TMDs, but this method is incompatible with most solvents^{105,108} and generally leads to a polydisperse distribution of flakes.¹²⁰ In addition, the quality of films deposited from this method depends strongly on the impurities, defects, and limited availability of starting materials.¹²¹ On the other hand, the mechanical exfoliation method is labor intensive and cannot be scaled up.^{29,30} The growth on substrates strategy creates films with high crystallinity and controlled thickness, but the deposition typically requires high vacuum and/or high reaction temperature processes.^{112,114,115} Colloidal synthesis method allows the preparation of large amounts of mono- and few-layer TMDs with good crystallinity and relative monodispersity, making it the favorable

approach for low-cost large-area applications. Recently, synthesis of MoS₂ has drawn substantial effort, however reports on colloidal synthesis of other layered TMDs are meager.^{38,120,122}

In this study, we demonstrate a general method to synthesize few-layer crystalline flakes of TMD (M= Mo, W; X= S, Se) in solution at low temperature (< 300 °C), in the presence of oleylamine as a capping ligand^{117,123,124} and a long-chain 1,2-hexadecanediol (HDD) as reducing agent^{123,125,126} using microwave-assisted heating. Specifically, we quantified the effect of HDD concentration on the composition of TMD films. Sufficiently high HDD concentrations were found to be necessary to produce films with high M⁴⁺ content, representing MX₂, and minimum oxides presence. The microwave-assisted one-pot synthesis of TMD flakes represents a simple and effective method to obtain few-layer TMDs under mild reaction conditions (280 °C), short reaction times (<1.5 h), using readily available precursors.

4.2 Experiments

4.2.1 Materials and sample preparation

TMD flakes suspensions in oleylamine were synthesized using a modified version of a published recipe for FeS₂.¹²⁷ MoCl₃ and WCl₄ were purchased from Sigma Aldrich and were used as received as the metal precursor. Sulfur flakes (99.99%, Strem), Sulfur powder (99.99%, Alfa Aesar), carbon disulfide (CS₂, >99%, Sigma Aldrich), selenium powder (99.99%, Alfa Aesar), and tellurium powder (99.99%, Sigma Aldrich) were used as the chalcogen source for the synthesis of sulfides, selenides, tellurides respectively. Commercial MoS₂ powder (99.99%, Alfa Aesar) and liquid exfoliated MoS₂ (refer to Chapter 5.2.1) were used as reference for ionization energy measurements. For the synthesis, 0.17 mmol metal precursor was dissolved under N₂ in

3.33 mL of oleylamine (Sigma Aldrich) in presence of 1,2-hexadecanediol (>98%, TCI America) at different concentrations, ranging from 0 to 0.5 M. 1.66 mL of chalcogen precursor dissolved in pure oleylamine (50 mg/mL) was then added to the test tube containing the metal precursor solution. The test tube was placed in a single-mode 2.54 GHz microwave reactor (CEM Discovery). The solution was maintained at 100 °C for 1h to achieve complete dissolution, followed by a synthesis step at 280 °C for 15 min to synthesize the TMD suspension. We selected this synthesis temperature because it was the maximum operation temperature allowed by the microwave reactor for short time reactions (≤ 15 minutes) and produced the most generalizable and reproducible results. After the solution was cooled to room temperature, the TMD flakes were washed with 20 mL of anhydrous ethanol and precipitated by centrifugation at 10,000 rpm for 10 minutes. The solid product was redispersed in dichloromethane.

4.2.2 Characterization

For Raman spectroscopy and tapping-mode AFM of individual flakes, TMD flake dispersions were diluted to 0.5 mgmL^{-1} and spin-coated at 2000 rpm on p-doped silicon substrates (Prime Wafers) previously cleaned with IPA rinse, H₂O rinse, and 15 min UV-O₃ treatment (BioForce Nanosciences). For XPS and Raman spectroscopy on films, TMD flakes were drop-casted from dichloromethane dispersion on Si substrates previously cleaned. The Raman characterization was carried out under ambient conditions with a Renishaw inVia confocal spectrometer. The laser excitation wavelength is at 532 nm with 2400 line/mm grating and NA=0.85 (laser spot size of $\sim 0.7 \text{ }\mu\text{m}$), which allow a spectra acquisition at 0.5 cm^{-1} resolution and $\sim 1 \text{ cm}^{-1}/\text{pixel}$ spectra dispersion. Spectra acquisitions were done with a laser power of $\sim 0.22 \text{ mW}$ and 1 s exposure to avoid local laser heating that can cause sample damage and unwanted Raman thermal shifts.

Each spectrum is an average of 20 acquisitions to minimize the noise-to-signal ratio. The high resolution Raman mappings were collected at step size of ~ 100 nm with spatial resolution of ~ 300 nm. The topography was studied using an Asylum MFP-3D atomic force microscope under tapping mode. XPS was measured using a Ulvac-PHI VersaProbe2 with monochromated Al K_{α} source (1486.8 eV). All spectra were collected at an angle of 45° to the sample surface with energy step of 0.2 eV and pass energy of 23.5 eV, and were fitted using commercial software (MultiPak, Ulvac-PHI). Mo^{4+} fraction for each TMD represents an average and standard deviation of measurements performed on two or more samples.

The crystal structure and composition of the samples were analysed by STEM, SAED and XPS. The samples for the TEM analysis were prepared by drop-casting the TMD dispersion samples onto lacey carbon film supported TEM grids (018990, Ted Pella). STEM imaging was performed on a Probe-corrected JEM-ARM200F (JEOL USA, Inc.) equipped with a Probe Cs-Corrector (CEOS GmbH) operated at 80 kV. The convergence semi-angle of the incident electron beam is 25 mrad and the collection angle for the ADF detector is 70-200 mrad. The third order spherical aberration C_s is set to 0.2 μm , resulting a resolution better than 2 \AA . SAED diffraction patterns were obtained using a low-voltage transmission electron microscopy (LVTEM-5, Delong Instruments) with 5 keV electron energy. Φ was measured in air using a scanning Kelvin probe (SKP 5050, KP Technology), with Au as the reference material ($\Phi=5.15$ eV). PESA analysis was performed on TMD films to measure ionization energy using a RKI Instruments Model AC-2 system with 100 nW deuterium lamp power and energy scanning between 4.5 and 5.5 eV with a step of 0.05 eV. The uncertainty of the PESA measurements was found to be 0.05 eV.

4.3 Results and Discussion

We chose MoS₂ to study the effect of synthesis conditions on TMD quality. We examined the effect of the HDD concentration in the precursor solution on the resulting TMD film composition using X-ray photoelectron spectroscopy (XPS) (**Fig. 4.1**). Deconvolution of the Mo 3d XPS spectra of MoS₂ flakes synthesized without HDD reveals the presence of Mo⁴⁺ and Mo⁶⁺. Doublet peaks at 228.8 eV and 231.9 eV are assigned to Mo⁴⁺ species in MoS₂,¹²⁸ and correspond to Mo 3d_{5/2} and Mo 3d_{3/2}, respectively. Additional peaks at 232.3 eV and 235.3 eV from Mo⁶⁺ are associated with the presence of MoO₃.^{93,129} Smaller peaks at 230.2 eV and 233.3 eV are also evident (**Fig. 4.1a**). To identify the origin of these intermediate peaks, we compare the values of spin-orbit components Mo 3d_{5/2} and Mo 3d_{3/2} for MoO_x nanoparticles (Chapter 3) and MoS₂ flakes synthesized under non-HDD condition (**Table 4.1**). The binding energies of these extra peaks found in MoS₂ flakes synthesized under non-HDD condition (**Fig. 4.1a** orange, 230.2 eV and 233.3 eV) are not consistent with the binding energies of MoO₂ (229.8 eV and 232.9 eV) or Mo₂O₅ (231.4 eV and 234.5 eV) species from the MoO_x nanoparticles. The intermediate peak positions match published values for molybdenum oxysulfide films (MoO_yS_z),^{130,131} suggesting that some molybdenum is present in a mixed oxygen-sulfur species. This mixed species is possibly originated from oxidation of the MoS₂ during atmosphere exposure for sample preparation. HAADF STEM images showed presence of vacancies in the atomic structure of MoS₂ flakes (**Fig. 4.2a**). Sulfur vacancies in transition metal disulfides have been proven to be oxygen chemisorption sites.¹³²

The Mo^{4+} fraction, defined as the area under the Mo^{4+} peaks divided by the total Mo peaks area, was 0.56 ± 0.07 . The ratio of sulfur to molybdenum from MoS_2 (X/M^{4+}) obtained for the MoS_2 with no HDD was 1.57 ± 0.09 , indicating that MoS_2 flakes synthesized under non-HDD condition are S deficient.

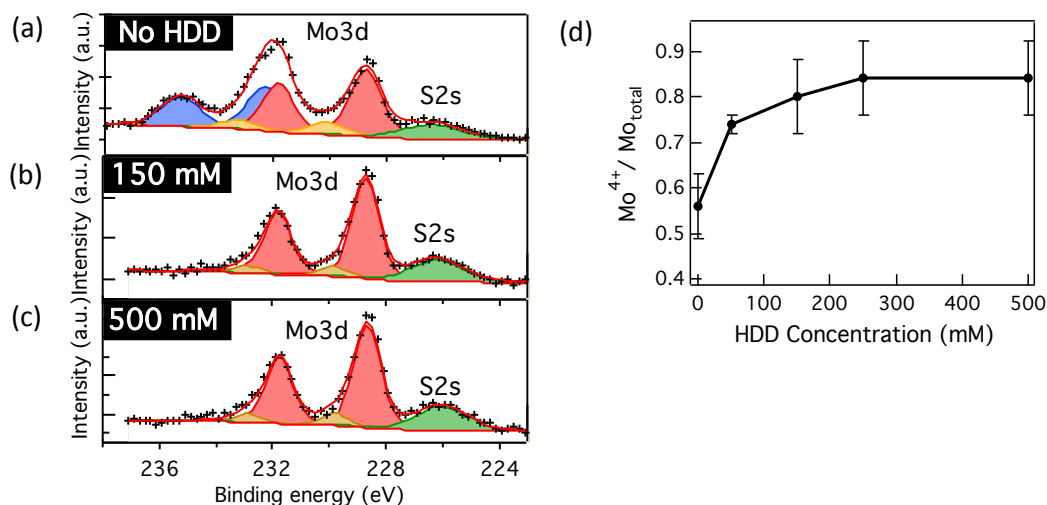


Fig. 4.1 Mo 3d XPS spectra of MoS_2 synthesized with different HDD concentrations: (a) No HDD, (b) 150 mM, and (c) 500 mM. The Mo 3d peaks were deconvoluted to show Mo^{4+} and Mo^{6+} oxidation states contributions, represented by red and blue areas, respectively. The orange areas represent an oxysulfide species contribution. (d) Mo^{4+} fraction in the MoS_2 films, area under the Mo^{4+} peaks divided by the total Mo peaks area, vs HDD concentration.

Table 4.1 XPS binding energy values comparison for MoO_x nanoparticles as synthesized and MoS_2 flakes synthesized without HDD.

MoO_x nanoparticles as synth.				MoS_2 flakes synth. under non-HDD			
	Peak Position (eV)		Distance from Mo^{6+} 5/2		Peak Position (eV)		Distance from Mo^{6+} 5/2
	5/2	3/2			5/2	3/2	
MoO_2	229.8	232.9	2.6	MoS_2	228.8	231.9	3.5
Mo_2O_5	231.4	234.5	1	MoO_yS_z	230.2	233.3	2.1
MoO_3	232.4	235.5	—	MoO_3	232.3	235.3	—

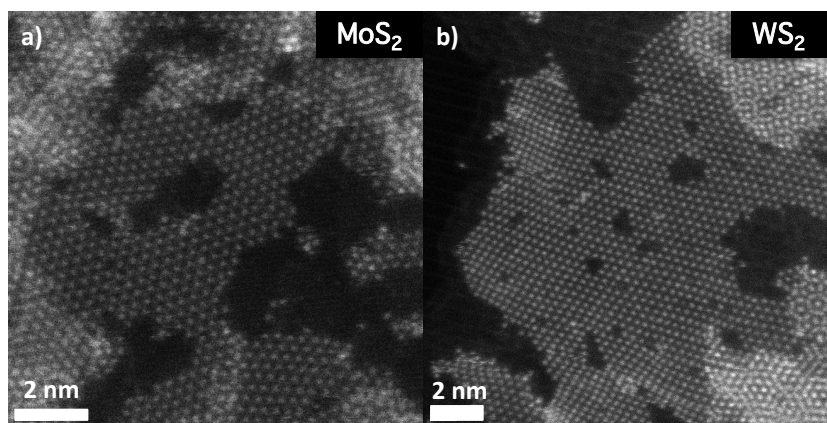


Fig. 4.2 HAADF images of synthesized few-layer TMD flakes: a) MoS₂ and b) WS₂.

Adding 150 mM HDD to the precursor solution caused the Mo⁴⁺ fraction and X/M⁴⁺ to increase to 0.80 ± 0.08 and 2.03 ± 0.11 , respectively. The absence of a prominent Mo⁶⁺ peak at around 235 eV indicates that oxidation to Mo⁶⁺ is minimal (**Fig. 4.1b**). Increasing the HDD concentration to 500 mM did not significantly modify the Mo⁴⁺ fraction (0.84 ± 0.08) nor X/Mo⁴⁺ (1.99 ± 0.06) (**Fig. 4.1c**). Nevertheless, the oxysulfide species (**Fig. 4.1**, orange) is still present in all samples and the binding energies were independent of HDD concentration. **Fig. 4.1d** shows Mo⁴⁺ fraction of the MoS₂ flakes as function of HDD concentration in the precursor solution ranging from 0 to 500 mM. The data show a strong correlation between the amount of HDD in the precursor solution and the formation of MoS₂. A saturation of Mo⁴⁺ fraction is achieved for HDD concentration ≥ 150 mM, which is necessary to ensure oxide formation in the thermolysis process.

Fig. 4.3 shows the O 1s, C 1s, and S 2p region of the XPS spectra for MoS₂ containing no HDD, 150 mM, and 500mM HDD in the precursor solution. Deconvolution of the O 1s XPS spectra of

MoS₂ flakes synthesized without HDD reveals the presence of peaks attributed to oxides at 530.5 eV, and a second peak at 532.3 eV attributed to adsorbed oxygen species (OH⁻ or H₂O).⁹³ The 530.5 eV peak associated with oxide species decreased drastically when 150 mM HDD was used for the synthesis of the MoS₂ flakes and remained the same for 500 mM HDD. The peak attributed to chemisorbed oxygen remained constant for all synthesis conditions. In the C 1s XPS spectra stayed the same regardless of the HDD concentration, indicating that increasing the HDD concentration was not reflected on the carbon content of the MoS₂. We believe that the excess of organics is removed during the washing. The MoS₂ exhibited a strong peak at 284.8 eV from C-C and C-H bonds, likely due to hydrocarbon contamination from air exposure. Also, a small contribution from the carbon-oxygen bond at ~ 286 eV.⁹³ The S 2p region of the spectra can be fitted to doublet peaks at 161.9 eV and 163.3 eV corresponding to S 2p_{3/2} and S 2p_{1/2}¹³³ and the peak positions remained the same for all synthesis conditions. The MoS₂ flakes synthesized under non-HDD condition exhibited a broader full width at half maximum (FWHM) of the S 2p peaks (2.1 eV) compared to the MoS₂ flakes synthesized using 150 mM and 500 mM HDD (1.8 eV). The broadening of the S 2p peaks associated with the formation of new peaks has been reported previously for MoS₂ samples with presence of high oxide content.^{130,131} However, the addition of doublet peaks resulted in an unrealistically poor fit.

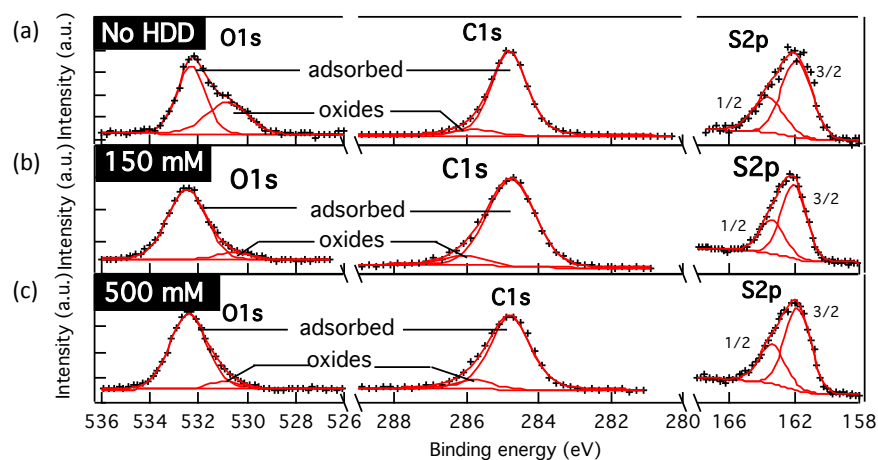


Fig. 4.3 O 1s, C 1s, and S 2p of XPS spectra for synthesized MoS₂ at different HDD concentrations: (a) No HDD, (b) 150 mM, and (c) 500 mM.

Using the HDD concentration of 150 mM with different metal and chalcogen precursors, TMD flakes of MoSe₂, WS₂, and WSe₂ flakes were synthesized following the same solvothermal method and conditions. **Fig. 4.4a** shows the Mo 3d and Se 3d regions of the XPS spectra for MoSe₂ flakes. The Mo 3d spectra can be fitted to doublet peaks at 228.9 eV and 232.1 eV, corresponding to Mo 3d_{5/2} and Mo 3d_{3/2} for Mo⁴⁺.⁹³ A broad peak attributed to Se 3s at 229.5 eV can also be distinguished.^{134,135} In addition, peaks at 230.8 eV and 232.9 eV can be distinguished. These additional peaks may be attributed to molybdenum in a mixed oxygen-selenium environment (MoO_ySe_z), following the same behavior as the molybdenum oxysulfide described previously. The Mo⁴⁺ fraction for MoSe₂ was 0.84 ± 0.01 and X/M⁴⁺ obtained was 2.03 ± 0.13 , same as X/M⁴⁺ ratio for MoS₂ synthesized with 150 mM HDD. The Se 3d region of the XPS can be fitted to doublet peaks at 54.7 eV and 55.6 eV corresponding to Se 3d_{5/2} and Se 3d_{3/2} reported for selenides.^{134,135}

Fig. 4.4b shows the W 4f and S 2p regions of the XPS spectra for WS₂ flakes. The W 4f XPS spectra of WS₂ flakes can be fitted to doublet peaks at 32.2 eV and 34.3 eV, corresponding to W 4f_{7/2} and W 4f_{5/2} of WS₂.¹³⁶ Additional doublet peaks at 33.1 eV and 35.2 eV can be distinguished, consistent with published values for tungsten oxysulfide films (WO_yS_z),^{137,138} implying presence of mixed oxygen-sulfur species. HAADF STEM images of synthesized WS₂ flakes also showed presence of vacancies in the atomic structure (**Fig. 4.2b**), consistent with the presence of chemisorbed oxygen. The W⁴⁺ fraction was 0.73 ± 0.02 and X/M⁴⁺ from WS₂ ratio obtained was 2.08 ± 0.07 . A broad peak corresponding W 5p_{3/2} can also be observed at 37.2 eV. The S 2p region of the XPS shows doublet peaks at 161.9 eV and 163.2 eV corresponding to S 2p_{3/2} and S 2p_{1/2},^{136,139} same as those found for MoS₂ (**Fig. 4.3**).

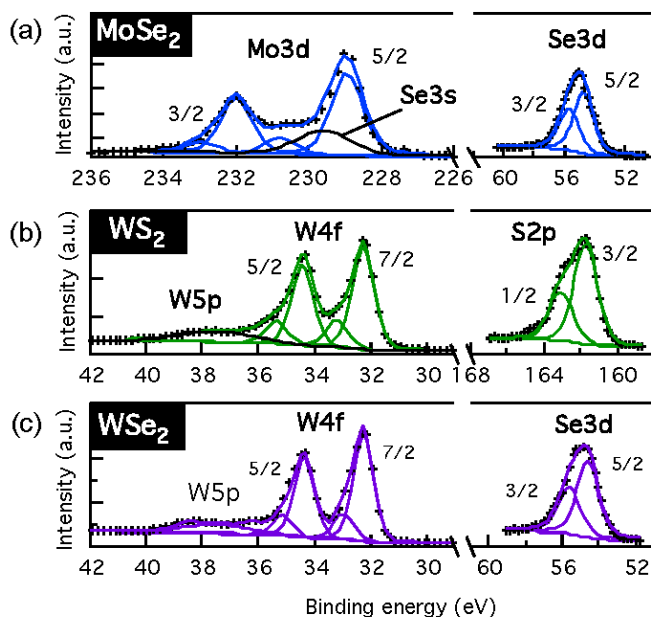


Fig. 4.4 XPS spectra of TMDs synthesized with 150mM HDD concentration: (a) MoSe₂, (b) WS₂ (c) WSe₂.

Fig. 4.4c shows the W 4f and Se 3d regions of the XPS spectra for WSe₂ flakes. The strongest peaks at 32.3 eV and 34.4 eV correspond to W 4f_{7/2} and W 4f_{5/2} of WSe₂ respectively.¹⁴⁰ The presence of the peaks at 33.0 eV and 35.1 eV can also be seen, associated with presence of WO_ySe_z. The W⁴⁺ fraction was 0.79 ± 0.02 and X/M⁴⁺ from WSe₂ ratio obtained was 2.03 ± 0.13 . The Se 3d_{5/2} and 3d_{3/2} peak positions are the same as those in MoSe₂ shown in **Fig. 4.4a**. The absence of prominent peaks around 530 eV (O 1s region) and 287 eV (C 1s region) is consistent with the absence of peaks associated with oxide species, confirming that the oxide impurities are minimal for all materials (**Fig. 4.5**). In addition, X/M⁴⁺ ratios for MoS₂, MoSe₂, WS₂, and WSe₂ synthesized using 150 mM HDD were close to the stoichiometric ratio.

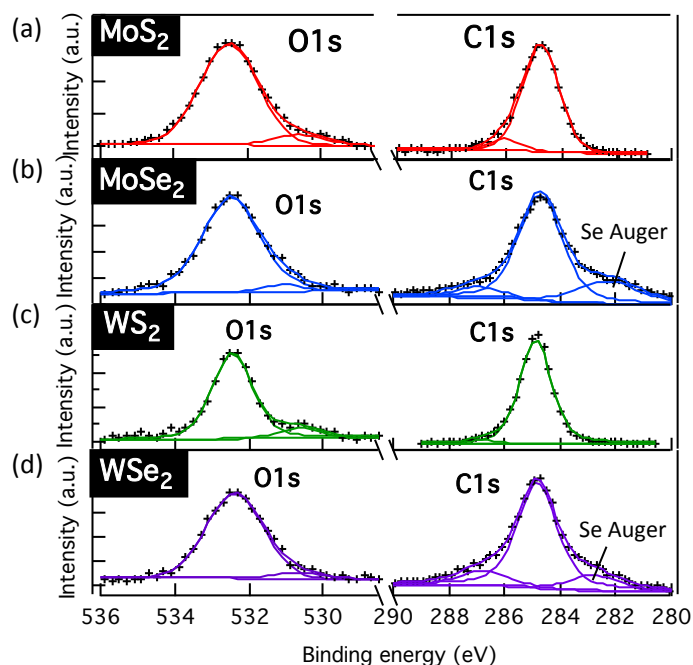


Fig. 4.5 O 1s and C 1s XPS spectra of synthesized TMDs using 150 mM HDD: (a) MoS₂, (b) MoSe₂, (c) WS₂, and (d) WSe₂.

To determine the thickness of these materials, we examined the TMD flakes using tapping-mode atomic force microscope (AFM). TMD dispersions were diluted and spin-coated over silicon substrates in order to isolate individual flakes. **Fig. 4.6** shows AFM topography images of individual MoS₂, MoSe₂, WS₂, and WSe₂ flakes. It is noteworthy to point out that all four synthesized materials have relative large lateral sizes of $\geq 2 \mu\text{m}$. We extracted height traces from the topography images and found a clear height uniformity in all materials with thicknesses ~ 2 nm. In addition to the large lateral size thin flakes, presence of thick flakes with smaller size can be observed for all TMDs (bright spots in **Fig. 4.6**).

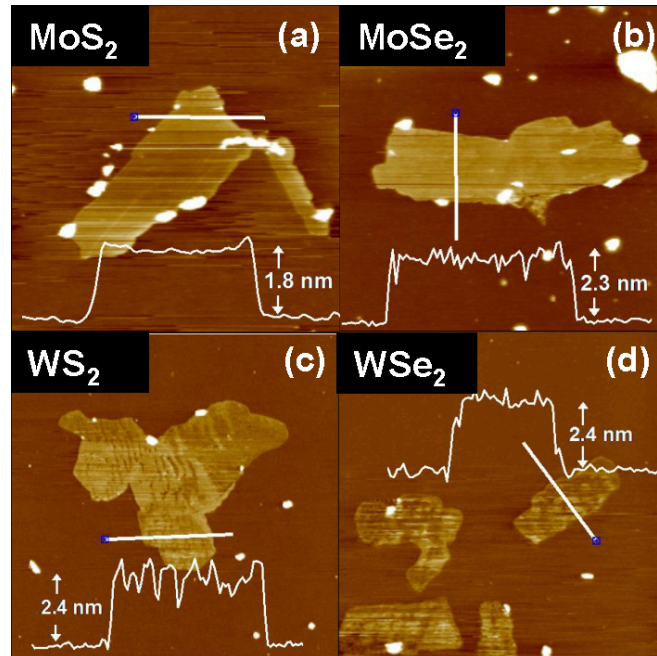


Fig. 4.6 $5 \times 5 \mu\text{m}$ AFM images of typical TMD flakes for (a) MoS₂, (b) MoSe₂, (c) WS₂, and (d) WSe₂. Inset: Height profile taken along the white line in the AFM image.

We believe that these thick flakes are originated during the sonication for the sample preparation, an AFM image of a thick MoS₂ flake is shown in **Fig. 4.7**. Also, TMDs are known to have low tensile strengths,¹¹⁰ and small pieces of TMD may detach and form stacks during deposition.

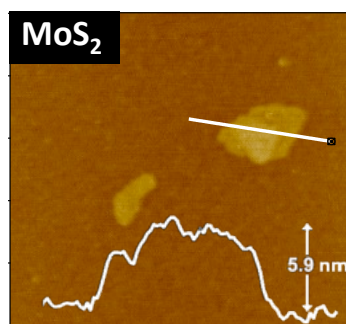


Fig. 4.7 1 x 1 μm AFM image of thick MoS₂ flakes with small lateral size. Inset: Height profile taken along the white line in the AFM image.

Raman spectroscopy was used to study the phase of the few-layer TMDs. The Raman spectra performed on drop casted films exhibit the typical in-plane E_{2g}^1 and out-of-plane A_{1g} vibration modes for MoS₂ and WS₂, the A_{1g} vibration mode of MoSe₂, and the overlap of E_{2g}^1 - A_{1g} modes for WSe₂ (**Fig. 4.8**). The peak positions are consistent with trigonal prismatic (2H) phase.¹⁴¹⁻¹⁴³

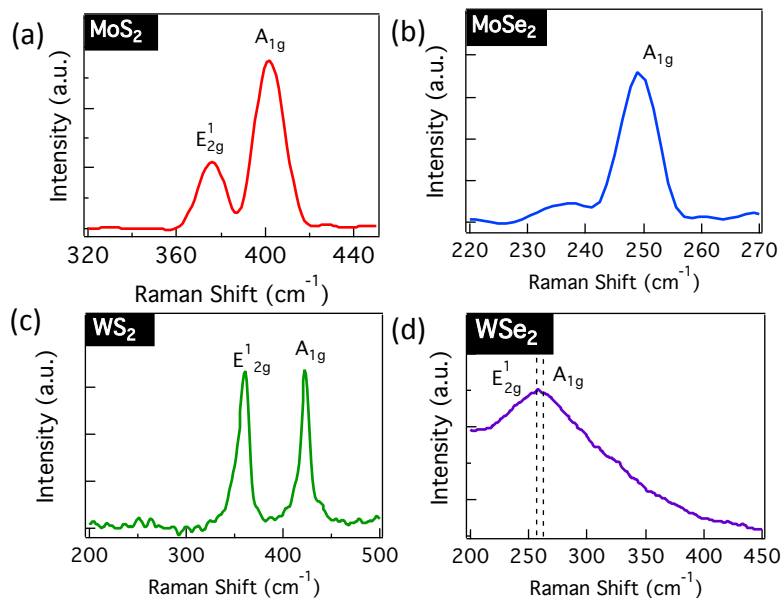


Fig. 4.8 Raman spectra of TMD films deposited on silicon substrates: (a) MoS₂, (b) MoSe₂, (c) WS₂, and (d) MoSe₂.

Fig. 4.9 shows an optical image (panel a) and Raman intensity mapping (panel b) of an individual MoS₂ flake deposited on silicon. The Raman mapping was performed at 401 cm⁻¹ (A_{1g} mode peak) and shows a uniform and strong intensity over the flake, implying that the MoS₂ exhibits high crystallinity consistent with STEM results (*vide infra*).

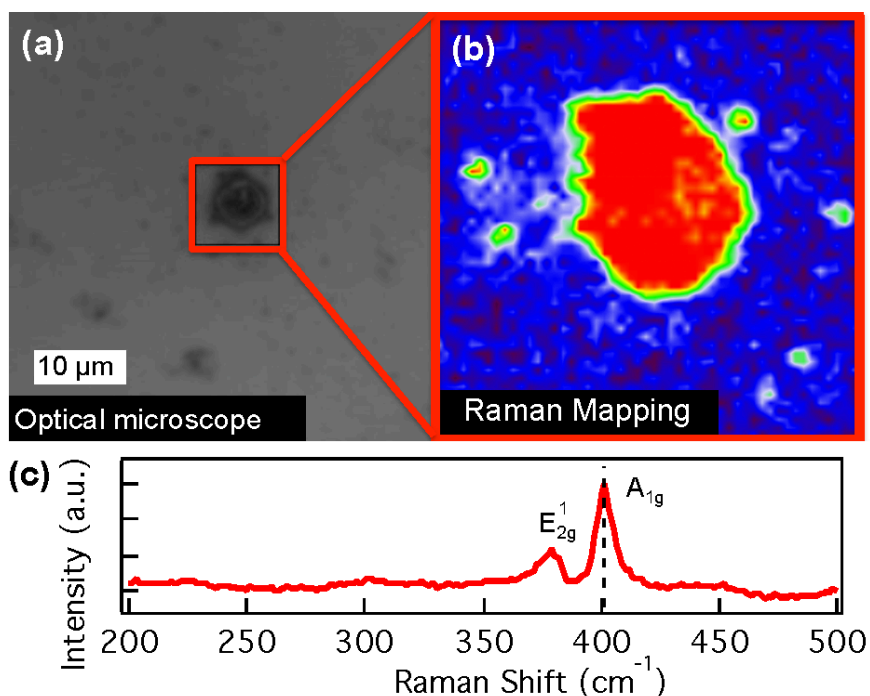


Fig. 4.9 Raman characterization for MoS₂ flakes. (a) Optical image and (b) Raman intensity mapping at 401 cm⁻¹ (A_{1g} mode peak, dashed line) of an individual MoS₂ nanoflake using 532 nm laser excitation. (c) Raman spectra of a typical MoS₂ nanoflake deposited on silicon substrate showed in (a).

The E_{2g}¹ and A_{1g} modes of in-plane and out-of-plane vibrations, respectively, that are typical for MoS₂ crystals can be observed on the Raman spectra collected from the flake (**Fig. 4.9c**). The distance between the peaks was observed to be 22 cm⁻¹, indicating two to three layers of MoS₂ and a thickness of 1 - 2 nm,¹⁴⁴ in good agreement with the thickness observed in the AFM measurements.

The crystalline structure of the synthesized TMD flakes has been further studied using high angle annular dark-field scanning transmission electron microscopy (HAADF-STEM). **Fig. 4.10a-d** shows the low magnification image of MoS₂, MoSe₂, WS₂, and WSe₂, respectively. The STEM images of the flakes clearly illustrate the monoatomic step edges, confirming that these materials are composed of few layers of highly crystalline TMDs. This result is consistent with Raman and AFM results. Extended defect formation within the flakes is visible, specially in WS₂, possibly formed during the synthesis, sample preparation, or originated from the electron beam irradiation damage.

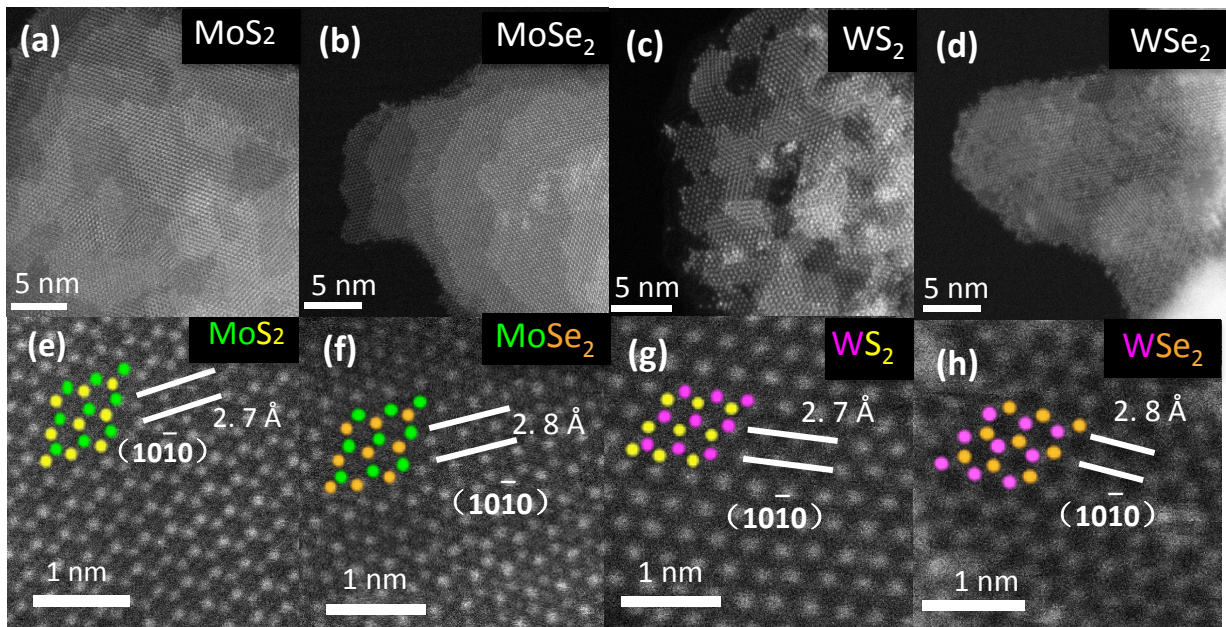


Fig. 4.10 HAADF images of synthesized few-layer TMD flakes: (a, e) MoS₂, (b, f) MoSe₂, (c, g) WS₂, and (d, h) WSe₂. In (g), W atomic positions have been resolved clearly while the intensity of S atoms is very weak. The atomic positions have been labeled in the high resolution HAADF images: Mo (green), W (magenta), S (Yellow), and Se (Orange). All the TMD flakes show 2H structure.

Fig. 4.10e-h shows top-view high-resolution STEM images, which show hexagonal lattices. The (10 $\bar{1}$ 0) lattice plane is marked by white lines and a *d*-spacing of 2.7 Å and 2.8 Å is found for

sulfides and selenides, respectively, consistent with JCPDF (01-077-1716), (00-072-1420), (00-008-0237), (00-038-1388). According to the high-resolution images, the crystal structure of all the synthesized materials has been confirmed to be 2H phase.

Φ and IE of TMD films drop casted on silicon is summarized in **Table 4.2**. Φ was found to be 4.65 eV for MoS₂, 4.63 eV for MoSe₂, 4.35 eV for WS₂, and 4.48 eV for WSe₂. IE of MoS₂, MoSe₂, WS₂, and WSe₂ were measured by photoelectron spectroscopy in air (PESA) yielding values of 4.74 eV, 4.72 eV, 4.53 eV, and 4.66 eV, respectively. The difference between Φ and IE for all synthesized TMDs was relatively small (< 0.2 eV). Given the band gaps from bulk TMDs reported in literature,^{28,145,146} the electronic levels of our solution synthesized TMDs suggest that these materials are p-type semiconductors.

Table 4.2 Electronic properties of synthesized TMDs using 150 mM HDD.

	Φ (eV)	IE (eV)
MoS ₂	4.65 ± 0.03	4.74 ± 0.05
MoSe ₂	4.63 ± 0.06	4.72 ± 0.05
WS ₂	4.35 ± 0.08	4.53 ± 0.05
WSe ₂	4.48 ± 0.03	4.66 ± 0.10

Table 4.3 compares the ionization energy values for MoS₂ films obtained from synthesized solution, liquid exfoliation solution, and commercial powder. The IE of the film deposited from liquid exfoliated MoS₂ is similar to that of the commercial MoS₂ powder, with values of 5.15 ±

0.05 eV and 5.27 ± 0.05 eV, respectively. In contrast, the IE of the synthesized MoS₂ film (4.75 ± 0.05 eV) is significantly lower than those measured for the other two MoS₂ films.

Table 4.3 Ionization energies of MoS₂ films obtained from synthesized solution, liquid exfoliation solution, and commercial powder.

MoS ₂ sample	IE (eV)
Synthesized	4.75 ± 0.05
Liq. Exfoliated	5.15 ± 0.05
Commercial pwd.	5.27 ± 0.05

There are three possible reasons for the lower IE of the synthesized MoS₂. The first possible reason is the change IE due to presence of MoO_yS_z or substoichiometric oxides (MoO_{3-x}) in the synthesized MoS₂ flake surface. However, the IE of commercial MoS₂ powder (5.27 ± 0.05 eV) and reported IE values for both MoO₂ and MoO₃ (> 6 eV)¹⁴⁷ are significantly higher, suggesting that the IE of substoichiometric oxides or oxysulfide should not be lower than 5.2 eV. The second possible reason is that the instrument could be measuring the IE of residual organics. Nevertheless, when we performed IE measurements on oleylamine and oleylamine in presence of HDD (150 mM), results showed no IE signal between 3.4 – 6.2 eV.

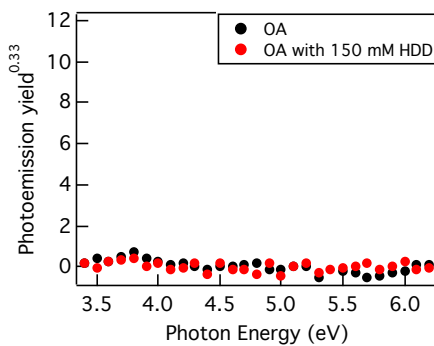


Fig. 4.11 Photoelectron spectrum for oleylamine and oleylamine in presence of HDD (150 mM).

The third possible reason is the formation of an interfacial dipole that modifies the ionization energy by adding an electrostatic dipole layer on the TMD surface.¹⁴⁸ To test the possible formation of interfacial dipole, the IE of films deposited from dispersions of commercial powder MoS₂ in several solvents was measured. The IE of the as-received powder is 5.27 ± 0.05 eV. Dispersing the MoS₂ powder into DCM or ethanol does not have significantly effect in IE, with 5.17 ± 0.05 eV and 5.27 ± 0.05 eV, respectively. If the MoS₂ powder is dispersed in oleylamine, followed by the washing with anhydrous ethanol, centrifuge, and dispersion in DCM steps described in Chapter 4.2, the IE drastically decreases to 4.53 ± 0.05 eV. The same IE value (4.55 ± 0.05 eV) is obtained when the MoS₂ powder is dispersed in oleylamine with presence of HDD (150 mM) prior washing, centrifuge, and redispersion in DCM steps, suggesting that the oleylamine is originating the interfacial dipole. The formation of interfacial dipoles using long chain amines, similar to oleylamine, has been reported previously for Ag substrates with a decrease of 0.45 eV in Φ ,¹⁴⁹ which is analogous to IE measurements in semiconductor materials.

Table 4.4 Ionization energies of commercial powder MoS₂ measured directly on the powder and films deposited from commercial powder MoS₂ dispersion in DCM following different preparation methods.

MoS ₂ sample	IE (eV)
MoS ₂ commercial pwd.	5.27 ± 0.05
MoS ₂ commercial pwd. in DCM	5.17 ± 0.05
MoS ₂ commercial pwd. in EtOH	5.27 ± 0.05
MoS ₂ commercial pwd. OA EtOH DCM	4.53 ± 0.05
MoS ₂ commercial pwd. (OA+HDD) EtOH DCM	4.55 ± 0.05
MoS ₂ commercial pwd. OA DCM	4.30 ± 0.05

A greater decrease in IE (4.30 ± 0.05 eV) is found when MoS₂ powder is dispersed in oleylamine, centrifuged and redispersed in DCM without previous washing steps with anhydrous

ethanol, implying that the presence of more organics leads to stronger dipole effect. These results confirm that the decrease in IE of the synthesized TMDs originates from the interfacial dipole due to oleylamine, as represented in **Fig. 4.12**.

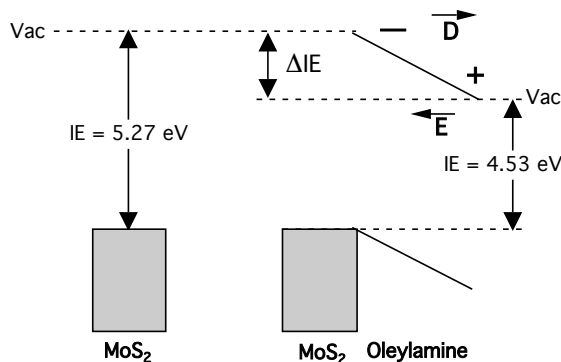


Fig. 4.12 Schematic representation of the impact of the formation of an interface dipole on the ionization energy at the oleylamine-MoS₂ interface denoting a shift of vacuum level at the interface due to dipole layer formation.

4.4 Synthesis of tellurides

Motivated by the attractive properties of the synthesized TMDs and the versatility of the synthesis method, we explored the synthesis of telluride TMDs (MoTe₂ and WTe₂). Telluride flake suspensions in oleylamine were synthesized using the same sulfides and selenides synthesis method, with 150 mM as HDD concentration. MoCl₃ or WCl₄ from Sigma Aldrich were used as received as the metal precursor and tellurium powder was used as the chalcogen source. However, the synthesis of tellurides did not result in the formation of desired TMD. Only a small quantity of precursors formed tellurides, producing mostly metal oxides instead (*vide infra*).

We examined the stoichiometry on the resulting flakes composition using XPS (**Fig. 4.13**). In **Fig. 4.13a**, deconvolution of the Mo 3d XPS spectra of MoTe₂ flakes reveals the presence of only Mo⁶⁺ species and the mixed species. The presence of a strong doublet peaks at 232.0 eV and 235.1 eV from Mo⁶⁺, associated with MoO₃,^{93,129} indicates that the sample is mostly oxidized (**Fig. 4.13a**).

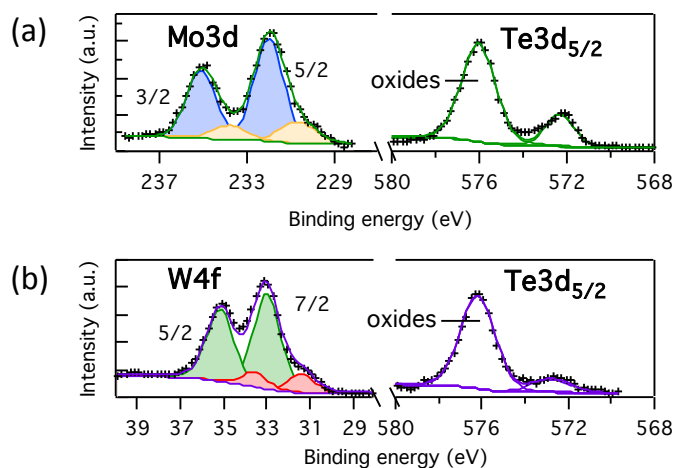


Fig. 4.13 XPS spectra of tellurides synthesized using 150mM HDD: (a) MoTe₂, (b) WTe₂.

The absence of doublet peaks assigned to Mo⁴⁺ species of MoTe₂ at ~228 eV¹⁵⁰ implies that the TMD produced after the reaction is minimal compared to oxide species. The Te 3d_{5/2} region of the XPS spectra shows two contributions, the main one situated at 576.0 eV, associated with TeO₂,¹⁵¹ and other small one at 572.3 eV associated with Mo-Te bond of MoTe₂.¹⁵⁰

Similar results were found for WTe₂ (**Fig. 4.13b**). The W 4f XPS spectra of WTe₂ shows doublet peaks at 33.0 eV and 35.2 eV associated with mixed environment species. The small contribution of doublet peaks assigned to W⁴⁺ species of MoTe₂ at 31.4 eV and 33.6 eV, corresponding to W

$4f_{7/2}$ and W $4f_{5/2}$ of WTe_2 ¹⁵² implies that the TMD produced after the reaction is minimal compared to oxide species. The Te $3d_{5/2}$ region of the XPS shows a strong peak at 576.1 eV corresponding to TeO_2 ,¹⁵¹ and an additional smaller contribution at 572.6 eV associated with W-Te bond of WTe_2 ,¹⁵² same as the found for $MoTe_2$ (**Fig. 4.13a**). The small contributions from Mo-Te and W-Te bonds in the Te $3d_{5/2}$ regions is in agreement with the absence of Mo^{4+} species in the Mo 3d region and the weak signal of W^{4+} species in the W 4f region of the XPS spectra. In addition, the presence of a strong TeO_2 peaks is consistent with the production of molybdenum oxide and tungsten oxide species during the synthesis.

4.5 Alternative sulfur precursors

We also investigated the TMD synthesis method using alternative sulfur precursor agents, including sulfur powder and carbon disulfide (CS_2) in order to obtain MoS_2 and WS_2 . We followed the same synthesis method described in section 4.2.1 without modifying synthesis conditions such as temperature, reaction time or precursor/HDD concentrations. Recently Jeong *et al.* reported the generation of highly reactive radicals from elemental sulfur (i.e. sulfur flakes and sulfur powder) during the reaction, which promoted degradation of the structural integrity of 2-D layered crystals.³⁸ To avoid reactive radical formation, they used CS_2 as alternative chalcogen precursor because no radical species are formed when CS_2 is heated in oleylamine.^{37,38} Hence, we first explored the synthesis of sulfides using $MoCl_3$ or WCl_4 as the metal precursor and sulfur powder as sulfur source and examined the effect of the chalcogen precursor solution on the resulting TMD film composition using XPS. We then explored the synthesis of sulfides using CS_2 as sulfur precursor and compared resulting TMD film composition to that using sulfur powder as chalcogen precursor.

Deconvolution of the Mo 3d XPS spectra of MoS₂ flakes synthesized with sulfur powder reveals the presence of Mo⁴⁺ and Mo⁶⁺ (**Fig. 4.14**). Doublet peaks at 228.4 eV and 231.5 eV are assigned to Mo⁴⁺ species in MoS₂,¹²⁸ and correspond to Mo 3d_{5/2} and Mo 3d_{3/2}, respectively. Additional peaks at 232.3 eV and 235.3 eV from Mo⁶⁺,^{93,129} are associated with the presence of MoO₃ (**Fig. 4.14a**).^{93,129}

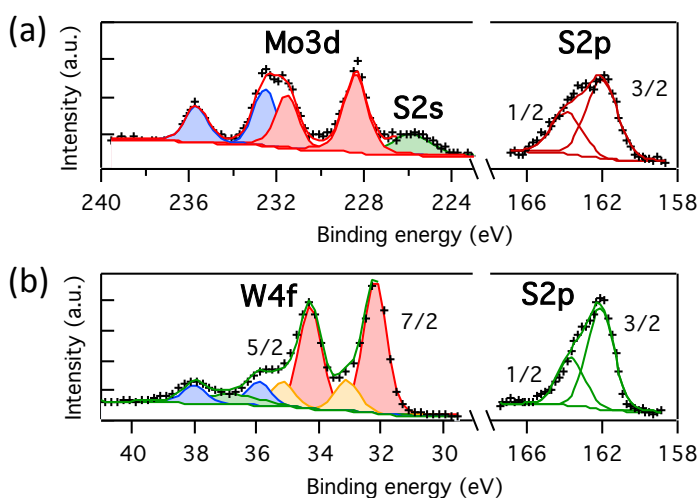


Fig. 4.14 XPS spectra of sulfides synthesized with sulfur powder as chalcogen precursor: (a) MoS₂, (b) WS₂. The Mo 3d and W 4f peaks were deconvoluted to show different oxidation states contributions, represented by red, orange, and blue areas.

The Mo⁴⁺ fraction was 0.6, indicating that MoS₂ flakes synthesized using sulfur powder contain MoO₃, similar to MoS₂ flakes synthesized with sulfur flakes as chalcogen precursor and no HDD in the precursor solution (**Fig. 4.1a**). The ratio of sulfur to molybdenum from MoS₂ obtained for the MoS₂ with no HDD was 2.2. The S 2p region of the spectra shows broad doublet peaks (FWHM = 2.3 eV), consistent with high-oxide content MoS₂ flakes, at 161.9 eV and 163.6 eV corresponding to S 2p_{3/2} and S 2p_{1/2}.¹³³

Fig. 4.14b shows the W 4f and S 2p regions of the XPS spectra for WS₂ flakes synthesized with sulfur powder. The W 4f XPS spectra of WS₂ flakes can be fitted to doublet peaks at 32.2 eV and 34.3 eV, corresponding to W 4f_{7/2} and W 4f_{5/2} of WS₂.¹³⁶ The W spectra also shows doublet peaks at 33.1 eV and 35.2 eV associated with tungsten oxysulfide films (WO_yS_z).^{137,138} In addition, strong doublet peaks at 36.0 eV and 38.0 eV, corresponding to W 4f_{7/2} and W 4f_{5/2} of WO₃.¹⁵³ The WS₂ fraction was 0.70 and X/M⁴⁺ from WS₂ ratio obtained was 2.12. A weak contribution of a broad peak corresponding W 5p can also be observed at 37.0 eV. The S 2p region of the XPS shows doublet peaks at 162.0 eV and 163.5 eV corresponding to S 2p_{3/2} and S 2p_{1/2},^{136,139} same as those found for MoS₂ synthesized with sulfur flakes (**Fig. 4.4b**).

Fig. 4.15 shows the effect of CS₂ as chalcogen precursor solution on TMD film composition using XPS. **Fig. 4.15a** depicts the Mo 3d and S2p regions of XPS spectra for MoS₂ synthesized with CS₂. The weak signal in both XPS regions implies that molybdenum and sulfur species present in the product film are below the detection limit of the instrument (< 1.0 at%). We believe that only a small amount of precursors reacted during the synthesis, while the remaining was removed during the washing. **Fig. 4.15b** shows the W 4f and S 2p regions of the XPS spectra for WS₂ flakes synthesized with sulfur powder. We observed six characteristic peaks at 32.2 eV, 34.3 eV, 33.1 eV 35.2 eV, 36.0 eV and 38.0 eV corresponding to W 4f_{7/2} of WS₂,¹³⁶ W 4f_{5/2} of WS₂,¹³⁶ W 4f_{7/2} of WO_yS_z,^{137,138} W 4f_{5/2} of WO_yS_z,^{137,138} W 4f_{7/2} of WO₃,¹⁵³ and W 4f_{5/2} of WO₃,¹⁵³ respectively. The WS₂ fraction was 0.55 and X/M⁴⁺ from W to S ratio obtained was 1.78. The S 2p region of the XPS shows doublet peaks at 162.0 eV and 163.3 eV corresponding

to S 2p_{3/2} and S 2p_{1/2},^{136,139} same as those found for WS₂ synthesized with sulfur flakes and sulfur powder (**Fig. 4.4b** and **Fig. 4.14b**, respectively).

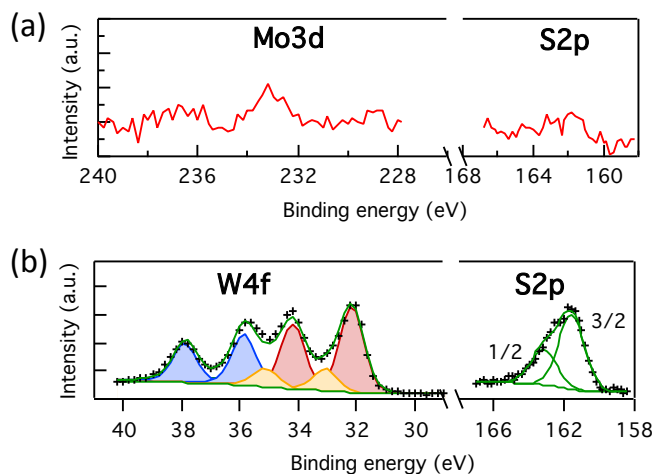


Fig. 4.15 XPS spectra of sulfides synthesized with CS₂ as chalcogen precursor: (a) MoS₂, (b) WS₂. The W 4f peaks were deconvoluted to show different oxidation states contributions, represented by red, orange, and blue areas.

The results indicate that MoS₂ flakes synthesized using sulfur powder are highly oxidized to MoO₃. In addition, WS₂ flakes synthesized using CS₂ are also highly oxidized to WO₃ and sulfur deficient, undesired characteristics for electronic oriented high quality TMDs. Synthesis of MoS₂ flakes using CS₂ as chalcogen precursor did not result in desired product.

4.6 Alternative molybdenum precursor

We also explored the TMD synthesis method using an alternative molybdenum precursor agent, molybdenum (V) chloride (MoCl₅) in order to obtain MoS₂ and MoSe₂. We followed the same synthesis method described in section 4.2.1 under identical synthesis conditions such as temperature, reaction time or precursor concentration. Sulfur flakes and selenium powder were

used as chalcogen precursor agents and 150 mM was selected as HDD concentration. We examined the effect of the molybdenum precursor on the resulting TMD film composition using XPS.

Fig. 4.16a shows Deconvolution of the Mo 3d XPS spectra of MoS₂ flakes synthesized with MoCl₅ reveals the presence of Mo⁴⁺. Doublet peaks at 228.4 eV and 231.5 eV are assigned to Mo⁴⁺ species in MoS₂,¹²⁸ and correspond to Mo 3d_{5/2} and Mo 3d_{3/2}, respectively. Smaller peaks at 230.0 eV and 233.1 eV assigned to MoO_yS_z^{130,131} are also evident (**Fig. 4.16a**). The Mo⁴⁺ fraction, defined as the area under the Mo⁴⁺ peaks divided by the total Mo peaks area, was 0.86. The ratio of sulfur to molybdenum from MoS₂ obtained for the MoS₂ synthesized with MoCl₅ was 2.22. The absence of a prominent Mo⁶⁺ peak at around 235 eV indicates that oxidation to Mo⁶⁺ is minimal, similar to results were obtained for MoS₂ flakes synthesized using MoCl₃ as molybdenum precursor on identical conditions (**Fig. 4.1b**). The S 2p region of the spectra can be fitted to doublet peaks at 161.9 eV and 163.6 eV corresponding to S 2p_{3/2} and S 2p_{1/2}.¹³³ Selected area electron diffraction was used to investigate the crystallinity of the MoS₂ flakes synthesized with MoCl₅ as molybdenum precursor and compared to MoS₂ flakes synthesized with MoCl₃ (**Fig. 4.17**). SAED diffraction pattern for MoS₂ flakes synthesized using MoCl₅ as molybdenum precursor shows absence of any diffraction typical of MoS₂, suggesting that the MoS₂ flakes consisted of amorphous phase (**Fig. 4.17a**). In contrast, SAED diffraction pattern for MoS₂ flakes synthesized under identical conditions but using MoCl₃ as molybdenum precursor, reveals clear presence of crystalline domains (**Fig. 4.17b**).

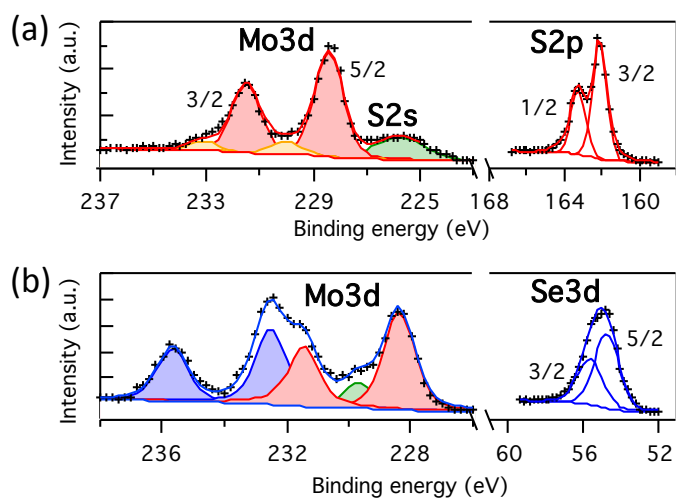


Fig. 4.16 XPS spectra of TMD flakes synthesized with MoCl_5 as molybdenum precursor: (a) MoS_2 , (b) MoSe_2 . The Mo 3d peaks were deconvoluted to show Mo^{4+} and Mo^{6+} oxidation states contributions, represented by red and blue areas, respectively.

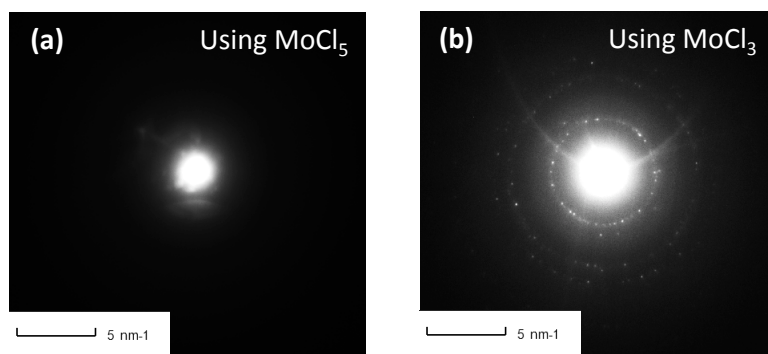


Fig. 4.17 SAED diffraction pattern of MoS_2 flakes synthesized with 150 mM HDD, using different molybdenum precursor: (a) MoCl_5 and (b) MoCl_3 .

Deconvolution of the Mo 3d XPS spectra of MoSe_2 flakes synthesized with MoCl_5 reveals the presence of Mo^{4+} and Mo^{6+} (**Fig. 4.16b**). Doublet peaks at 228.4 eV and 231.5 eV are assigned to Mo^{4+} species in MoSe_2 ,¹²⁸ at the same binding energies as those in MoSe_2 synthesized with MoCl_3 as molybdenum precursor (**Fig. 4.4a**). Additional strong peaks at 232.5 eV and 235.5 eV from Mo^{6+} ,^{93,129} associated with the presence of MoO_3 .^{93,129} The Mo^{4+} fraction was 0.48,

indicating that MoSe₂ flakes synthesized using MoCl₅ contain MoO₃. The ratio of selenium to molybdenum obtained was 2.0. The Se 3d region of the XPS (**Fig. 4.16b**), can be fitted to doublet peaks at 54.7 eV and 55.6 eV corresponding to Se 3d_{5/2} and Se 3d_{3/2} reported for selenides.^{134,135}

The results indicate that MoS₂ flakes synthesized using MoCl₅ as molybdenum precursor produce films with high Mo⁴⁺ content, representing MoS₂, and minimum oxides presence. However, MoS₂ flakes synthesized using MoCl₅ are not crystalline like the MoS₂ flakes synthesized using MoCl₃. In addition, MoSe₂ flakes synthesized using MoCl₅ are highly oxidized to MoO₃. Both low crystallinity and high oxides presence are undesired characteristics for electronic oriented high quality TMDs.

4.7 Conclusions

In this study, we used a microwaved-assisted method to synthesize TMD flakes of transition metal sulfides and selenides directly from precursors in solution. We demonstrate that the reducing agent, 1,2-hexadecanediol is critical to ensure TMD formation and eliminate corresponding metal oxide. Raman spectroscopy and transmission electron microscopy confirmed that all TMDs are highly crystalline and exhibit 2H phase. Atomic force microscopy indicated that these flakes are a few layers thick (~ 2 nm) with relatively large lateral sizes (> 2 μm), consistent with TEM results. Owing to their electronic levels, these TMDs showed to be p-type semiconductors. This versatile one-pot synthesis approach is promising for low-cost, large-area electronic applications of TMD thin films.

CHAPTER 5
INVERTED OPVs WITH MoS₂ HOLE TRANSPORT LAYER
DEPOSITED BY SPRAY COATING

Authors- Diego Barrera,^a Ali Jawaid,^b Trey B. Daunis,^a Lanxia Cheng,^a Qingxiao Wang,^a Yun-Ju Lee,^a Moon J. Kim,^a Jiyoung Kim,^a Richard A. Vaia,^b and Julia W. P. Hsu^a

^aDepartment of Materials Science and Engineering, The University of Texas at Dallas,
800 West Campbell Rd., Richardson, TX 75080

^bMaterials and Manufacturing Directorate, Air Force Research Laboratory,
Wright-Patterson AFB, OH 45433

Molybdenum disulfide (MoS_2) exhibits high work function and high mobility, making it a promising candidate for electronic applications. Currently, most applications require high vacuum or high reaction temperature processes to deposit MoS_2 . This chapter summarizes our results on organic photovoltaic devices made by room-temperature spray-coating of liquid-exfoliated MoS_2 suspension to form hole transport layer (HTL) on top of P3HT:PCBM bulk heterojunction. Such an approach is compatible with large area applications. Current-voltage data showed that FF of devices with MoS_2 HTL is similar to the devices using PEDOT:PSS HTL. However, V_{oc} and J_{sc} are reduced and the amount of J_{sc} reduction depends strongly on active layer thickness. These results can be understood by the strong absorption of light by MoS_2 , reducing/eliminating the back reflection from the top silver electrode. The experimental results are corroborated by calculations using transfer matrix method.

The contents of this paper are submitted as a paper entitled “**Inverted OPVs with MoS_2 hole transport layer deposited by spray coating**”, currently under review. The authors are Diego Barrera, Ali Jawaid, Trey B. Daunis, Lanxia Cheng, Qingxiao Wang, Yun-Ju Lee, Moon J. Kim, Jiyoung Kim, Richard A. Vaia, and Julia W. P. Hsu. My contribution was in fabrication and characterization of devices, analyzing the data, and writing the manuscript. Ali Jawaid contributed with the MoS_2 suspensions via liquid-exfoliation and fruitful discussions about the MoS_2 films deposition. Trey B. Daunis performed the ellipsometry of the MoS_2 films. Lanxia Cheng performed the Raman characterization on the MoS_2 films. Qingxiao Wang performed the STEM characterization of the liquid-exfoliated MoS_2 . Dr. Yun-Ju Lee provided careful guidance for the experiments and results discussions. Moon Prof. J. Kim and Prof. Jiyoung Kim provided insightful discussion on STEM and Raman results, respectively. Dr. Richard A. Via contributed

with guidance and fruitful discussions about MoS₂ exfoliation and deposition methods. Prof. Julia W. P. Hsu oversaw the project and provided the careful guidance for the experiments, analysis, and manuscript writing.

5.1 Introduction and motivation

MoS₂ is a two-dimensional (2D) semiconducting transition metal dichalcogenide (TMD) that has recently attracted much interest of the scientific community. Its structure consists of one layer of molybdenum atoms sandwiched between two layers of sulfur atoms with strong in-plane chemical bonds and weak out-of-plane van der Waals bonds that allow the material to be easily exfoliated into flakes with nanometer scale thicknesses.^{25,107,154} Because of its 2D nature, tunable bandgap,²⁸ and high electron mobility (~ 200 cm²/V s),²⁹ MoS₂ has been used in transistors,^{29,31} self-switching diodes,³² light-emitting diodes,³³ and photodetectors.³⁴ In addition, its high work function (~ 5.20 eV)^{121,154} makes MoS₂ a promising candidate to replace the acidic and hygroscopic poly(3,4-ethylenedioxythiophene):poly(styrenesulfonate) (PEDOT:PSS),⁷³ or the vacuum-deposited MoO₃⁵⁴ as hole transport layer for organic photovoltaics (OPVs).

A popular method for obtaining large quantities of TMD flakes is liquid exfoliation. In contrast to other wet chemistry exfoliation methods like ion intercalation, or dry methods such as micromechanical exfoliation and chemical vapor deposition, liquid exfoliation method^{107,108} is not time-consuming, does not lead to structural deformation of TMD, reduces the use of hazardous chemicals, and eliminates the necessity of high vacuum and high temperature processes. Thus, liquid exfoliation is a promising method towards large-area applications and scalable production. However, the surface tension of the commonly used solvents to exfoliate MoS₂,^{105,108} e.g. N-methyl-2-pyrrolidone (NMP), is relatively high ($\gamma \sim 40$ mJ/m²); hence,

subsequent MoS₂ film deposition requires complicated solvent exchange. In addition, while spin-coated films of liquid exfoliated MoS₂ has been demonstrated,^{155,156} spin-coating is not compatible with high volume roll-to-roll manufacturing.

Spray-coating is a high throughput and low waste method for thin film deposition, where a flowing carrier gas is used to disperse the source liquid into microscopic droplets, depositing the material on the substrate upon evaporation of the solvent.^{157,158} Complete coverage is achieved after a large number of coats, resulting in thick films with high roughness.¹⁵⁹ Nonetheless, functional organic photovoltaics (OPVs) have been obtained by spray-coating the bulk heterojunction (BHJ) active layer and/or hole transport layers (HTLs) of ~ 200 nm thicknesses, or ~ 3-4 times the surface roughness.¹⁶⁰

Several groups have reported utilizing solution deposited MoS₂ as HTL in OPVs with the conventional architecture.^{95,96,161} However, these reports required additional processing steps such as surface modification by organic surfactants⁹⁵ or post-deposition oxidation to MoO₃^{96,161} to achieve good device performance. In addition, the conventional architecture, where the high work function HTL was located next to the bottom transparent electrode and the low work function electron transport layer (ETL) was located above the active layer, was used in most reports; this architecture has been shown to be less stable compared to inverted architecture with the reversed transport layer order.²⁰ Recently, X. Gu *et al.* used lithium intercalated MoS₂ suspension to spin-coat an ultra-thin film on top of different active layers and successfully demonstrated the possibility of utilizing MoS₂ thin film as HTL on inverted architectures.¹⁵⁵ However, their MoS₂ material contained both trigonal prismatic (2H, semiconductor) and octahedral (1T, metallic) phases.

Herein, we report the fabrication of inverted OPVs using liquid-exfoliated pure 2H MoS₂ suspension in ethanol, deposited *via* spray-coating, on top of poly(3-hexylthiophene):phenyl-C60-butyric acid methyl ester (P3HT:PCBM) BHJ active layer. The electronic and structural properties of MoS₂ remained unchanged upon exfoliation. The performance of the MoS₂ devices is much better in terms of the power conversion efficiency (PCE) as compared to the no HTL device. In addition, we achieve fill factor and device rectification comparable with the well-established conducting polymer poly(3,4-ethylenedioxythiophene):poly(styrene sulfonate) (PEDOT:PSS) HTL. However, open-circuit voltage (V_{oc}) and short-circuit current density (J_{sc}) are reduced and the amount of J_{sc} reduction depends strongly on active layer thickness. This can be understood by the strong absorption of sun light by MoS₂, reducing/eliminating the back reflection from the top silver electrode. The experimental results agree quantitatively to calculations using transfer matrix method.

5.2 Experiments

5.2.1 MoS₂ exfoliation

MoS₂ suspension in ethanol was obtained following a procedure previously reported¹⁰⁸ with minor modifications. A 50 mL round bottom flask was loaded with MoS₂ (160 mg, 1mmol) and 10 mL of acetonitrile under an argon atmosphere. The solution was equilibrated and maintained at 0 °C (c.a. 30 minutes) throughout the reaction. Cumene hydroperoxide (CHP) (500 mL, 3 mmol) was added dropwise over the course of 15 minutes. After 24 hrs, the stirring was stopped, and the MoS₂ flakes sedimented. The yellow supernatant was reduced to 4 mL in volume, and the stirring was resumed. 100 mL of ice cold NaBH₄ (0.100 M) was added quickly to the MoS₂

slurry every hour until a total of 400 mL of NaBH₄ was added. The solution turned from gray to dull green in color, indicating exfoliation of MoS₂. After NaBH₄ addition was completed, the temperature was equilibrated to 25 °C and allowed to stir for 3 hrs. Subsequently, the suspension was transferred to a centrifuge tube and sedimented at 10,000 revolutions per minute (rpm). The supernatant containing excess NaBH₄ and CHP was removed and fresh, anhydrous ethanol was added to the MoS₂ flakes. The mixture was homogenized with a vortexer and briefly bath sonicated (c.a. 60 seconds). The suspension was then centrifuged at 1500 rpm to sediment out unexfoliated materials. The supernatant contains few-layer MoS₂ flakes, which is then centrifuged again at a 10,000 rpm to pellet the exfoliated flakes. After removing the supernatant, the flakes are then re-suspend in fresh ethanol at a final concentration of ~ 3 mg/mL.

5.2.2 Device fabrication

All processing were performed in N₂ unless otherwise noted. Inverted BHJ devices were fabricated on patterned indium tin oxide (ITO; 20 Ω/square, Xinyan). ZnO nanoparticle films deposited in air were used as ETL.¹⁶² 0.1 M zinc acetylacetonate hydrate (Gelest) and 0.01 M diethanolamine (DEA, Fisher) in anhydrous *n*-butanol were heated to 200 °C for 15 min in a single-mode 2.54 GHz microwave reactor (CEM Discovery SP) to obtain the ZnO nanoparticle suspension,¹⁶² which was spin-coated twice at 1000 rpm for 80 s to form the ETL on ITO. For the BHJ, P3HT (RMI-001E, Rieke Metals, Inc.) and PCBM (Solenne BV) were dissolved at 1:1 weight ratio in anhydrous chlorobenzene (Sigma-Aldrich). To achieve active layer thicknesses of 210 nm or less, 23:23 mg/mL of BHJ solution was spin-coated at different spin-speeds ranging from 1200- 4000 rpm. For thicker active layers, 36:36 mg/mL of BHJ solution was spin-coated at spin-speeds ranging from 800-4000 rpm. The thickness of the active layer was calculated by

UV-vis absorption based on calibration using profilometry. All the BHJ films were annealed at 170 °C for 10 min. MoS₂ films were spray-coated from the MoS₂ suspension in ethanol on top of the BHJ in air using a commercial airbrush (PointZero) with gravity-fed reservoir operated at ~30 psi of air pressure. The airbrush was placed perpendicular to the substrate at a distance of 10 cm at room temperature, and the air stream was engaged for ~5 s, after which the substrate was allowed to dry for ~60 s. To ensure a continuous MoS₂ film, 16 cycles of spray coats were performed. For reference devices, PEDOT:PSS (Clevios P VP AI 4083, Heraeus) was mixed with isopropanol in a 7:3 volume ratio, 0.35 vol.% of Dynol 604 (Air Products and Chemicals Inc.) was added, and the solution was stirred for 30 min. The PEDOT:PSS solution was then spin-coated in air at 4000 rpm for 30 s on top of the BHJ prior to the annealing of the BHJ in N₂. Finally, 100 nm of Ag electrode were thermally evaporated (Angstrom Engineering) to complete the devices, with area of 0.11 cm² each.

5.2.3 Materials characterization

Work function (Φ) was measured in air using a scanning Kelvin probe (SKP 5050, KP Technology), with Au as the reference material ($\Phi = 5.15$ eV). Photoelectron spectroscopy in air (PESA) analysis was performed to measure ionization energy (IE) using a RKI Instruments Model AC-2 with 100 nW deuterium lamp power and energy scanning between 4.5 and 5.5 eV with a step of 0.05 eV. The uncertainty of the PESA measurements was found to be 0.05 eV. MoS₂ film topography was studied using an Asylum MFP-3D atomic force microscope (AFM) under tapping mode. Raman measurements (Reinshaw inVia confocal spectrometer) was conducted using a 532 nm laser excitation with 2400 line/mm grating and NA=0.85 (laser spot size of ~0.7 μm), which allow a spectra acquisition at 0.5 cm⁻¹ resolution and ~1 cm⁻¹/pixel

spectra dispersion. Spectra acquisitions were done with low laser power (~ 0.22 mW) and 1 s exposure to avoid local laser heating caused lattice damage and unwanted Raman thermal shifts. The high resolution Raman mapping was collected at step size of ~ 100 nm with spatial resolution of ~ 300 nm. XPS was measured using a Ulvac-PHI VersaProbe 2 with monochromated Al K_{α} source (1486.8 eV). All spectra were collected at an angle of 45° to the sample surface with energy step of 0.2 eV and pass energy of 23.5 eV, and were fitted using commercial software (MultiPak, Ulvac-PHI). STEM imaging was performed on a JEM-ARM200F (JEOL USA, Inc.) equipped with a probe Cs-corrector (CEOS GmbH) operated at 120 kV. The convergence semi-angle of the incident electron beam is 25 mrad and the collection angle for the ADF detector is 70-200 mrad. The third order spherical aberration Cs is set to 0.2 μm , resulting a resolution better than 2 \AA .

5.2.4 Device characterization and modeling

For 1D transfer matrix method (TMM) calculation,¹⁶³ optical constants and thicknesses of each layer in the OPV device were measured by spectroscopic ellipsometry (J.A. Woollam) and remain fixed in the calculation, with the exception of the active layer thickness, which was varied from 50 to 550 nm. Absorption as a function of light wavelength and position within the device stack was calculated. Absorption within the active layer is integrated with the AM1.5G solar spectral intensity to derive the photogenerated current density for each device. The current density-voltage (J-V) curves were measured in N_2 under a class AAA solar simulator (Sun 3000, Abet Technologies) with an AM 1.5G filter at 100 mW/cm^2 using a low noise source meter (2635A, Keithley). The simulator intensity was set using a Si photodiode with KG5 filter (RR_227 KG5, Abet Technologies). A 2.5 mm diameter aperture was placed in front of each

device to rigorously define the illumination area to 0.049 cm². All data shown represent the average of at least four devices.

5.3 Results and Discussions

The inverted architecture used for our OPVs is shown in **Fig. 5.1a**. We measured the IE and Φ of these MoS₂ films to be 5.20 eV and 5.01 eV, respectively. **Fig. 5.1b** depicts the band alignment of the MoS₂ inverted devices, using previously measured energy levels for P3HT:PCBM¹⁶⁴ and ZnO.¹⁶² XPS and Raman characterization performed of the MoS₂ films indicated that the MoS₂ does not exhibit any oxidation and maintained the same 2H phase as the bulk MoS₂ crystal. **Fig. 5.2a** shows the XPS spectra for Mo 3d and S 2p regions. Deconvolution of the Mo 3d XPS spectra of MoS₂ films reveals the presence of a doublet peak at 228.9 eV and 232.1 eV, corresponding to Mo 3d_{5/2} and Mo 3d_{3/2} of Mo⁴⁺ species, assigned to MoS₂.^{108,133} The absence of a Mo⁶⁺ peak at around 235 eV indicates that MoO₃ is nonexistent. The S 2p region of the spectra can be fitted to doublet peaks at 161.9 eV and 163.3 eV corresponding to S 2p_{3/2} and S 2p_{1/2}, consistent with reported values for MoS₂.^{108,133}

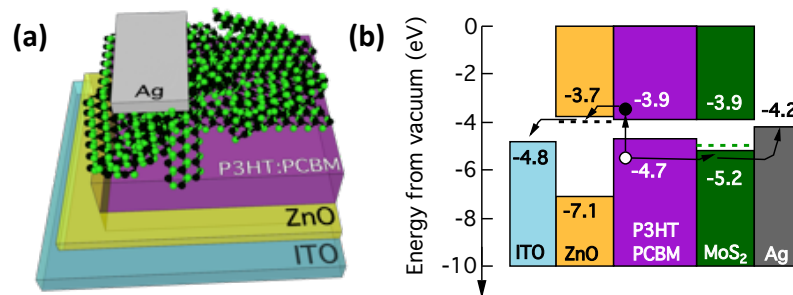


Fig. 5.1 Inverted organic photovoltaics with MoS₂ as the hole transport layer. (a) Schematic of the device architecture. (b) Energy diagram of the P3HT:PCBM active layer sandwiched between the ITO anode and the Ag cathode utilizing ZnO and MoS₂ as the electron transport layer and hole extraction layer, respectively.

Raman spectroscopy was used to study the phase of MoS₂ film. As expected, the Raman spectra exhibits the typical in-plane E_{2g}¹ and out-of-plane A_{1g} vibration modes for MoS₂ (**Fig. 5.2b**). The peak positions are consistent with trigonal prismatic (2H) phase, and suggest that the MoS₂ exhibits high crystallinity. The distance between the peaks was observed to be 24 cm⁻¹, suggestive of two to three atomic layers of MoS₂ with a thickness of 2 - 4 nm.¹⁴⁴

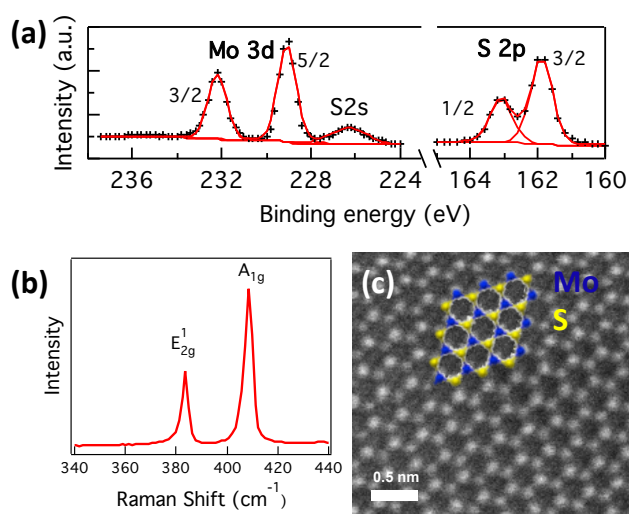


Fig. 5.2 Liquid-exfoliated MoS₂ characterization. (a) Mo 3d and S 2p XPS spectra. (b) Raman spectra at 532 nm excitation wavelength. (c) STEM images showing 2H structure.

The morphology of the liquid-exfoliated MoS₂ flakes has been further studied using high angle annular dark-field scanning transmission electron microscopy (HAADF-STEM). **Fig. 5.2c** exhibits a high-resolution STEM image of MoS₂, showing repeated atomic arrangement and lattice fringes of hexagonal patterns that confirm the crystal structure to be 2H phase.

A dense HTL was obtained through spray-coating from MoS₂ suspension on top of P3HT:PCBM active layer, as shown in the optical image in **Fig. 5.3a**. The thickness of the resulting MoS₂ film was evaluated by ellipsometry and found to be ~150 nm. To study the coverage of the HTL,

Raman mapping of the MoS₂ films, at 532 nm excitation wavelength, of the out-of-plane vibration mode (E_{2g}^1) at 384 cm⁻¹ was performed.

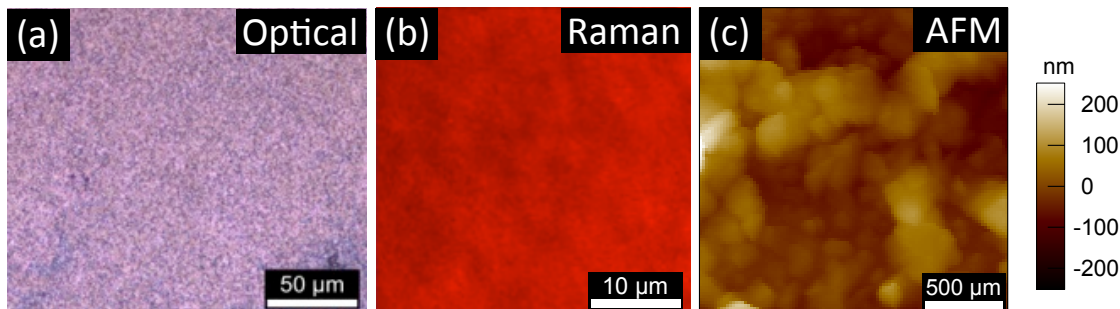


Fig. 5.3 Optical, Raman and AFM characterization for MoS₂ HTL films. (a) Optical microscopic image of a typical MoS₂ spray-coated on top of P3HT:PCBM. (b) Raman intensity mapping at 375 cm⁻¹ (E_{2g} mode peak) of the MoS₂ film on P3HT:PCBM, using 532 nm laser excitation showing complete coverage. (c) 2 x 2 μm tapping mode AFM of a typical MoS₂ film spray-coated on top of P3HT:PCBM.

Fig. 5.3b provide spatial maps of the E_{2g}^1 intensity, showing continuous and relatively uniform coverage of the BHJ by MoS₂ over the entire sampling area. The tapping mode AFM of the MoS₂ film also reveals a continuous film (**Fig. 5.3c**). The root mean square (RMS) roughness obtained from the AFM analysis was 47 nm. No obvious voids were detected, although we cannot rule out pinholes with dimensions smaller than the lateral resolution for Raman and AFM techniques (~300 nm and ~10 nm, respectively).

After verifying the surface morphology, we tested the OPVs to assess the performance of MoS₂ as HTL. The J - V curves in **Fig. 5.4a-b** compare the performance of devices with an active layer thickness of 210 nm, fabricated with MoS₂ (blue), PEDOT:PSS (red), and without HTL (black). The average short circuit current density (J_{sc}), open-circuit voltage (V_{oc}), fill factor (FF), PCE,

R_{se} , and R_{sh} values for each set of devices are summarized in **Table 5.1**. It can be seen that the device without HTL exhibits average power conversion efficiency of $0.05 \pm 0.01\%$ with nearly zero V_{oc} , caused by the low built-in field across the active layer created by the small difference between Φ of the Ag anode (4.2 eV) and Φ of the ZnO ETL (4.0 eV).^{165,166} The insertion of spray-coated MoS₂ films between P3HT:PCBM and Ag significantly increased the built-in field, resulting in a substantial increase in J_{sc} , V_{oc} , and FF, and an enhancement in the power conversion efficiency (η) to $2.00 \pm 0.04\%$. The η value is lower than that of the control device with PEDOT:PSS HTL at $2.96 \pm 0.09\%$, however. When we examine the other device parameters, we find that FF of the two devices are identical at 0.645, suggesting that the MoS₂ HTL does not lead to more shorts compared to PEDOT:PSS. A small decrease in V_{oc} for the MoS₂ device (0.502 ± 0.004 V) compared to the PEDOT:PSS device (0.568 ± 0.004 V) was observed, probably due to the lower Φ of MoS₂ when deposited on the P3HT:PCBM (4.80 eV).^{165,166} A larger contribution to the device performance difference results from the 23% lower J_{sc} of the MoS₂ device (6.18 ± 0.11 mA/cm²) compared to the PEDOT:PSS device (8.07 ± 0.17 mA/cm²). It is also noticeable that the device without HTL exhibits poor device rectification. The insertion of spray-coated MoS₂ films between P3HT:PCBM and Ag results in an enhancement in device rectification and a substantial reduction in R_{se} from 500.3 ± 370.1 Ω cm² to 9.5 ± 1.6 Ω cm². However, the R_{se} value is higher than that of the control device with PEDOT:PSS HTL at 5.3 ± 1.2 Ω cm². We also find that R_{sh} of the MoS₂ ($4.41E+05 \pm 6.19E+03$ Ω cm²) device is higher than PEDOT:PSS device ($2.04E+04 \pm 5.80E+03$ Ω cm²), suggesting that the MoS₂ HTL produces less leakage current compared to PEDOT:PSS.

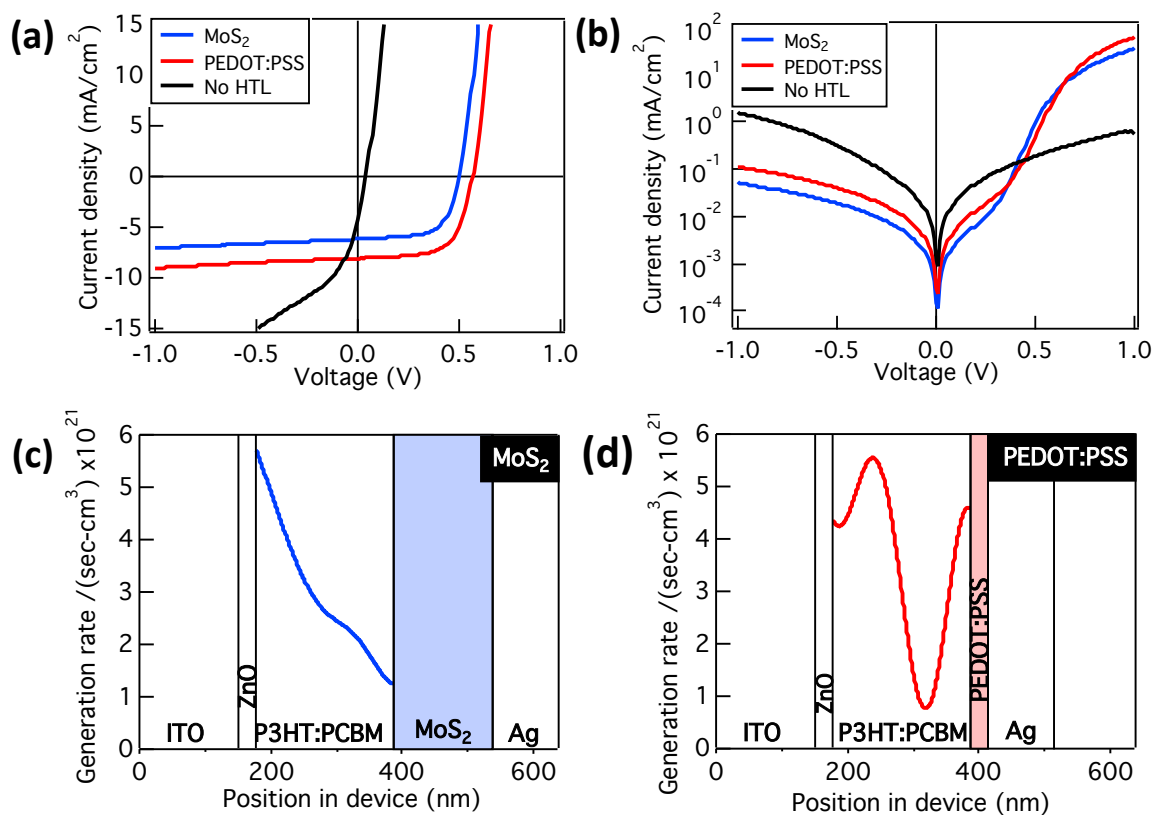


Fig. 5.4 J-V characteristics of solar cells under (a) 100 mW/cm² AM 1.5G illumination and (b) darkness for devices fabricated with MoS₂ (blue), PEDOT:PSS (red), and without HTL (black). Generation rate for photovoltaic devices fabricated with (c) MoS₂, and (d) PEDOT:PSS.

Table 5.1 Summary of the device performance obtained from J-V characteristics of organic photovoltaics taken under 100 mW/cm² AM 1.5G illumination and darkness.

Sample	HTL	V _{oc} (V)	J _{sc} (mA/cm ²)	FF ()	Eff (%)	R _{se} (Ω cm ²)	R _{sh} (Ω cm ²)
No HTL		0.043 ± 0.005	4.24 ± 0.30	0.262 ± 0.008	0.05 ± 0.01	500.3 ± 370.1	2.93E+04 ± 2.74E+04
MoS ₂		0.502 ± 0.004	6.18 ± 0.11	0.645 ± 0.006	2.00 ± 0.04	9.5 ± 1.6	4.41E+05 ± 6.19E+03
PEDOT:PSS		0.568 ± 0.004	8.07 ± 0.17	0.646 ± 0.010	2.96 ± 0.09	5.3 ± 1.2	2.04E+04 ± 5.80E+03

The J_{sc} discrepancy for MoS₂ and PEDOT:PSS is consistent with the fact that the 150 nm thick MoS₂ film absorbs significantly more visible light than the 25 nm thick PEDOT:PSS film. **Fig. 5.5** shows the UV-vis absorbance spectra for spray-coated MoS₂ (blue) and spin-coated

PEDOT:PSS (red) films deposited on glass. The strong absorption of the MoS₂ contrasts with the null absorption of the PEDOT:PSS. As a result, less light is back-reflected by the Ag electrode, and absorbed by the active layer, generating less photocurrent.

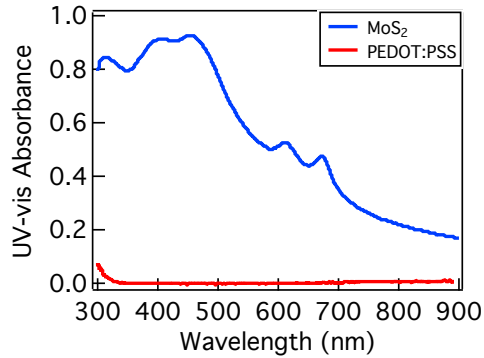


Fig. 5.5 UV-vis absorbance spectra for spray-coated MoS₂ (blue) and spin-coated PEDOT:PSS (red) films deposited on glass.

To confirm this, we calculated the generation rate in the active layer for MoS₂ and PEDOT:PSS devices using the 1D TMM,¹⁶³ in which the photovoltaic device is simulated as a multilayer stack interacting with a planar wave of light incident normal to the substrate. **Fig. 5.4c** and **Fig. 5.4d** show the calculated generation rate profiles within the active layer for MoS₂ HTL and PEDOT:PSS HTL devices, respectively. A clear reduction of the generation adjacent to the MoS₂ interface compared to the PEDOT:PSS device can be seen, confirming that the lower J_{sc} of a device with MoS₂ HTL compared to PEDOT:PSS HTL arises from the significantly reduced absorption of light within the active layer.

If this hypothesis is true, a smaller discrepancy in J_{sc} should be observed on thicker active layer devices where back-reflected light does not have as an important role on the photocurrent

generation. Thus, we fabricated and tested the performance of MoS₂ and PEDOT:PSS devices with different active layer thicknesses and compared their measured J_{sc} to predictions from TMM photocurrent generation profile (**Fig. 5.6**). Absorption as function of wavelength at each position within the device was calculated and integrated with the AM 1.5G spectral intensity to obtain the photogenerated current density as a function of active layer thickness. We note that TMM calculated current density will always be higher than measured J_{sc} , because it assumes 100% IQE with all carriers collected. To compare experimental and calculation results, we assume that the bulk recombination loss is the same in devices with the same active layer thickness and different HTLs, and take the ratio of the short circuit current densities for MoS₂ vs. PEDOT:PSS devices for each active layer thickness.

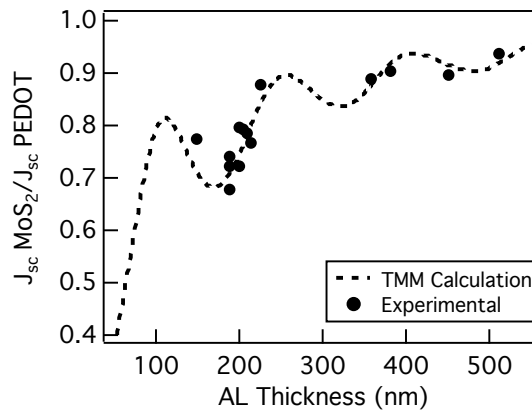


Fig. 5.6 Influence of the active layer thickness on the MoS₂ device performance. Photocurrent profile ratio between MoS₂ and PEDOT:PSS devices calculated from TMM (dashed line), and experimental results obtained from J_{sc} (solid markers).

The dashed curve in **Fig. 5.6** depicts the J_{sc} ratio for the two types of devices calculated using TMM, whereas the solid markers represent the experimental J_{sc} ratio. A clear agreement between simulated values and experimental results can be seen. A J_{sc} ratio closer to one for thicker active

layer devices confirms our hypothesis that J_{sc} reduction in the MoS₂ devices are due to differences in back-reflection. We have tried spray-coating thinner MoS₂ films using less concentrated MoS₂ suspensions, but OPVs using these thinner films exhibited shunt leakage problems. Thus, to further enhance the performance of the MoS₂ devices, we must further optimize the spray-coating procedure to deposit homogeneous HTLs using thinner films of MoS₂, or deposit HTLs of TMDs with greater transparency.

5.4 MoSe₂ Devices

We explored the use of other solution processed TMD as HTL and found that the performance of the devices fabricated with MoSe₂ are similar to MoS₂ devices. **Fig. 5.7** represents J - V characteristics of MoSe₂ (**Fig. 5.7**, green) and MoS₂ (**Fig. 5.7**, blue) devices. The OPV parameters for both devices are summarized in **Table 2.1**. The use of MoSe₂ films between P3HT:PCBM and Ag results in increased η of $2.27 \pm 0.06\%$ compared to $2.00 \pm 0.04\%$ of MoS₂ device. When we examine the other device parameters, we find that FF for both devices is identical at 0.645. A small increase in V_{oc} for the MoSe₂ device (0.510 ± 0.000 V) compared to the MoS₂ device (0.502 ± 0.004 V). A larger contribution to the device performance difference results from the 12% higher J_{sc} of the MoSe₂ device (6.95 ± 0.20 mA/cm²) compared to the MoSe₂ device (6.18 ± 0.11 mA/cm²). It is also noticeable that the MoSe₂ device exhibits lower reverse leakage current than the MoS₂ device (**Fig. 5.7b**) and a substantial reduction in R_{se} of 6.6 ± 1.3 Ω cm² compared to 9.5 ± 1.6 Ω cm².

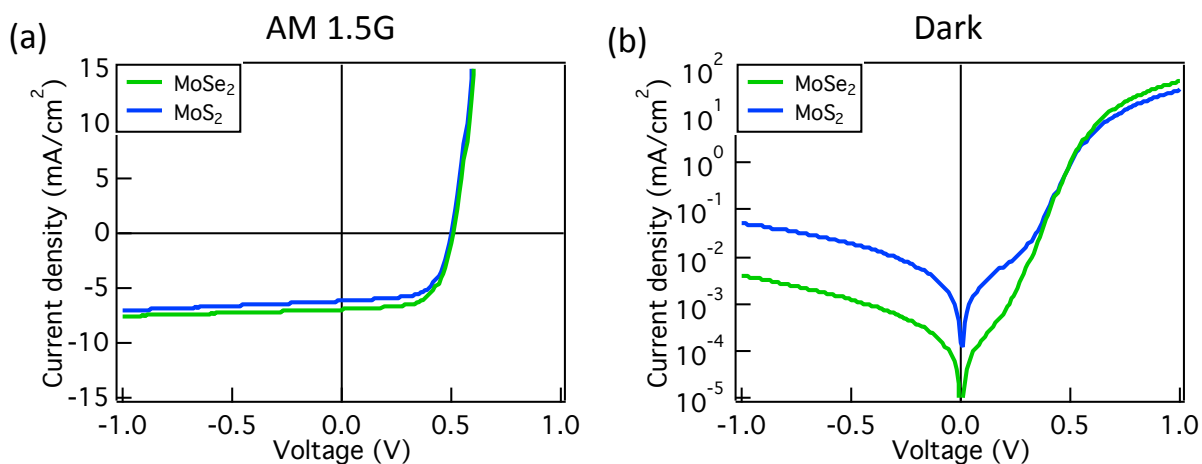


Fig. 5.7 J-V characteristics of solar cells under (a) 100 mW/cm² AM 1.5G illumination and (b) darkness for devices fabricated with MoSe₂ (green) and MoS₂ (blue).

Table 5.2 Summary of the device performance obtained from J-V characteristics of organic photovoltaics taken under 100 mW/cm² AM 1.5G illumination and darkness.

HTL	V _{oc} (V)	J _{sc} (mA/cm ²)	FF (%)	η (%)	R _{se} (Ω cm ²)	R _{sh} (Ω cm ²)
MoSe ₂	0.510 ± 0.000	6.95 ± 0.20	0.640 ± 0.005	2.27 ± 0.06	6.6 ± 1.3	2.04E+06 ± 1.92E+06
MoS ₂	0.502 ± 0.004	6.18 ± 0.11	0.645 ± 0.006	2.00 ± 0.04	9.5 ± 1.6	4.41E+05 ± 6.19E+05

However, the MoSe₂ deposition is less reliable due to low MoSe₂ concentration achievable in suspension, which is limited to ~2 mg/mL, making it difficult to reproducibly deposit of a MoSe₂ films with suitable thickness without pinholes.

5.5 Conclusions

In this study, we successfully implement the spray-coated MoS₂ in an organic photovoltaic device. Despite using a thick layer on top of the P3HT:PCBM active layer, we showed that the incorporation of MoS₂ as hole transport layer is possible without oxidizing or modifying its structural arrangement to octahedral phase. Electrical measurements on the devices showed that FF achieved using MoS₂ is identical to that using spin-coated PEDOT:PSS. TMM calculations

showed that the lower J_{sc} observed in MoS₂ devices is explained by reduced light absorption in the active layer region due to less back-reflected light in MoS₂ devices. The knowledge developed in our study should enable further optimization of TMD material properties and spray coating technique towards low cost and high performance applications of these novel materials.

CHAPTER 6

GENERAL CONCLUSIONS

This dissertation focused mainly on developing solution-processed materials as transport layers for organic photovoltaic (OPV) devices, and understanding their effect on device performance. We have demonstrated the influence of the underlying layer on the bulk heterojunction (BHJ) layer morphology. We showed that phase segregation leads to a reduction of interfacial area and lower phenyl-C60-butyric acid methyl ester (PCBM) concentrations outside of the clusters in the active layer, resulting in drastic reduction of OPV parameters due to both low charge generation and high bimolecular recombination. We found a simple solution, by rinsing the pyrolyzed monoethanolamine (MEA)-containing ZnO films with 2-methoxyethanol (MOE) or using a ZnO recipe without MEA which significantly reduced the formation of PCBM clusters and produced devices with good performance.

We demonstrated that *in situ* chemical oxidation of MoO_x nanoparticle suspensions with H₂O₂ is a simple but versatile method to control their stoichiometry and electronic properties. Our synthesis resulted in ≤ 1 nm MoO_x nanoparticles with high work function and almost entirely MoO₃, properties which are desirable for HTL material in OPV devices. We established a clear correlation between the work function and the Mo⁶⁺ fraction of the MoO_x, and achieved a tuning of work function over a large range. Moreover, the simplicity of the chemical oxidation procedure should be generally applicable to other transition metal oxide nanomaterials with tunable stoichiometry and properties.

We also demonstrated the ability to synthesize MoS₂, MoSe₂, WS₂, and WSe₂ flakes by solvothermal method using microwave heating. Spectroscopy techniques showed the presence of

2H phase and selected area electron diffraction (SAED) and transmission electron microscopy (TEM) confirmed the hexagonal structure for all materials. All transition metal dichalcogenide (TMD) flake thickness are consistent with a few-layer flakes. According to photoelectron spectroscopy in air (PESA) and Kelvin probe measurements, all four synthesized TMDs are p-type. The synthesis of layered materials, with optimal electronic properties contributes to the pursuit of materials suitable for electronic applications.

Finally, we successfully implemented the spray-coated MoS₂ in an organic photovoltaic device. We showed that the incorporation of liquid-exfoliated MoS₂ films as hole transport layer is possible without oxidizing or modifying its structural arrangement to octahedral phase. Electrical measurements on the devices showed that fill factor (FF) achieved using MoS₂ is identical to that using spin-coated PEDOT:PSS. Transfer matrix method (TMM) calculations showed that the lower short circuit current density (J_{sc}) observed in MoS₂ devices is explained by reduced light absorption in the active layer region due to less back-reflected light in MoS₂ devices.

Taken together, the investigations carried out in this dissertation contribute positively towards finding routes for low-temperature solution processing of metal-oxides and transition metal dichalcogenides, suitable to replace their vacuum processed analogues and building blocks in large-scale OPVs fabrication.

APPENDIX I

BAND STRUCTURE MEASUREMENTS ON BULK TRANSITION METAL DICHALCOGENIDES

In this appendix, a brief summary of electronic structure characterization employed to study the properties of freshly exfoliated surface of geological TMD crystals is presented. Several studies have shown that bulk MoS₂ is intrinsically an n-type semiconductor with an indirect bandgap of 1.2–1.3 eV for multilayers.¹⁶⁷⁻¹⁷⁰ However, p-type behavior has been also reported on bulk crystals.¹⁷¹⁻¹⁷⁴ In this study, we use Kelvin probe and photoelectron spectroscopy in air (PESA) measurements to investigate the origin of the variation in MoS₂ properties. Results indicate that the MoS₂ crystals that were prepared in an identical manner can exhibit either n- or p-type behavior.

The Φ variation of two different MoS₂ samples was measured in air by the Kelvin probe (SKP 5050, KP Technology) technique with Au as the reference material ($\Phi = 5.15$ eV), before and after exfoliation (**Table A.I.1**). Such surfaces are anticipated to be representative of those produced by exfoliation typically used for device fabrication. Prior to exfoliation, the Φ value is measured to be $\Phi (\text{MoS}_2\text{-A})_{\text{before}} = 5.19 \pm 0.01$ eV and $\Phi (\text{MoS}_2\text{-B})_{\text{before}} = 4.87 \pm 0.01$ eV. The Φ measured within 1 min of the exfoliation process decreases with time and then stabilizes after about 25 min (**Fig. A.I.1a**) in a laboratory ambient. The time dependent behavior could arise from the adsorption of contaminants from the atmosphere (e.g., hydrocarbons, water, etc.) or oxidation. The work function values stabilize close to the pre-exfoliated surface value after 30

min exposure to the ambient with the following values: Φ (MoS₂-A)_{after} = 5.16 ± 0.01 eV and Φ (MoS₂-B)_{after} = 4.85 ± 0.01 eV.

Table A.I.1 Φ and IE measurements on two different samples before and after 25 min from exfoliation.

MoS ₂ crystal exfoliation	MoS ₂ -A		MoS ₂ -B	
	before	after	before	after
ϕ (eV)	5.19 ± 0.01	5.16 ± 0.01	4.87 ± 0.01	4.85 ± 0.01
IE (eV)	5.68 ± 0.05	5.64 ± 0.05	5.66 ± 0.05	5.61 ± 0.05

Different samples examined under identical ambient conditions show significant variations in the Φ . The highest Φ value obtained on the air-exposed, as-exfoliated sample (>25 min) was measured at 5.33 eV and the lowest value at 4.45 eV. On yet another sample MoS₂-C (see **Fig. A.I.1b**), the Φ after exfoliation reaches the value prior to exfoliation only after a period of 7 days as shown in **Fig. A.I.1b**, which indicates that it takes much longer for the surface of this sample to be saturated with ambient contaminants; this sample also showed non-monotonic time dependence during the first 6 h after exfoliation.

To compare the time dependent variation on another van der Waals material, the Φ of highly ordered pyrolytic graphite (HOPG) was measured under the same ambient conditions for the first hour after exfoliation. **Fig. A.I.1c** shows that the Φ of HOPG is stable in air with a variation of only between 4.64 and 4.67 eV indicative of the chemical stability of the sp² surface and in good agreement with literature.¹⁷⁵ The reactivity of the MoS₂ surface with oxygen, and the impact on the electronic structure, has been recently studied using density functional theory.¹⁷⁶ Calculations

indicate that the air stability of MoS₂ and the electronic band gap are significantly impacted by the presence of surface defects and increasing oxygen concentration.¹⁷⁶

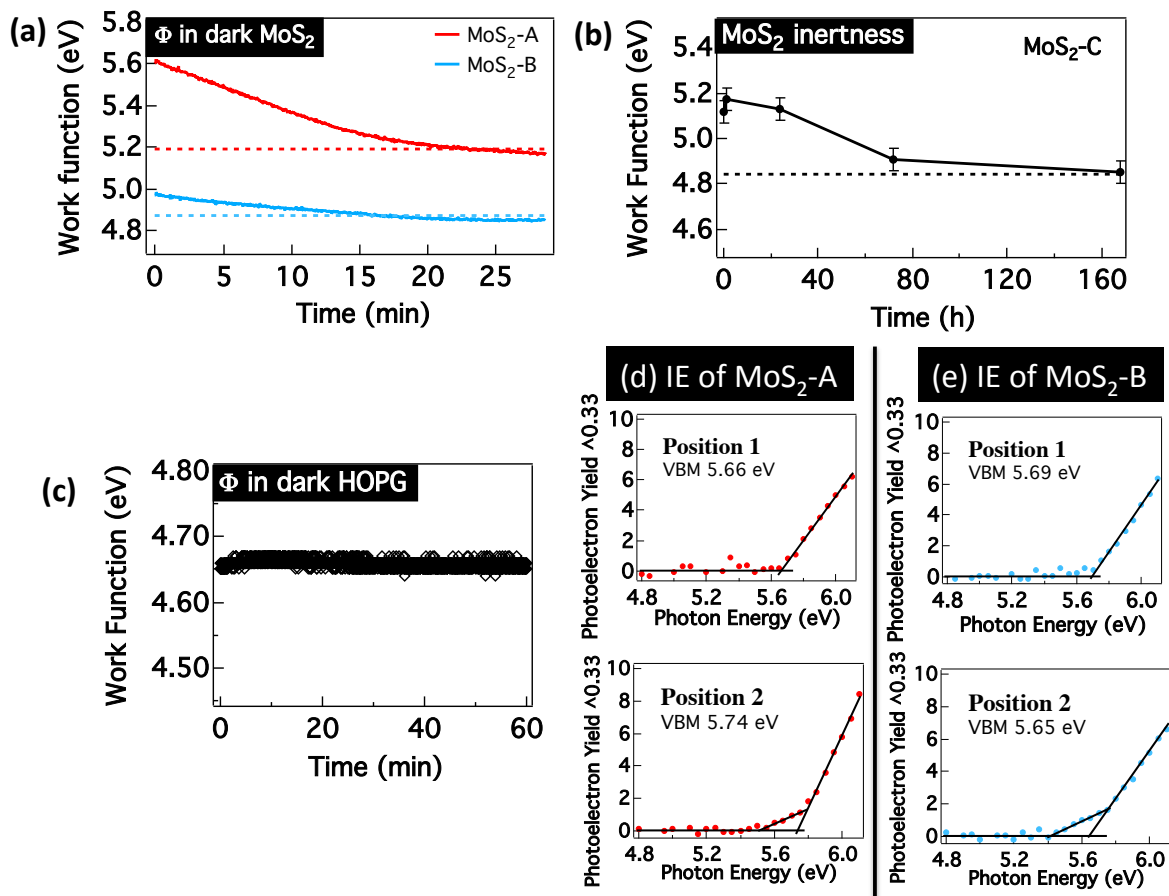


Fig. A.I.1 (a) Kelvin probe measurements of the Φ of two different samples MoS₂-A and MoS₂-B. (b) Φ evolution recorded on another (MoS₂-C) freshly exfoliated surface (0 h) until reaching the initial value (dashed line) after a week (168 h) in air. (c) Φ measurements on as-exfoliated HOPG. The HOPG Φ averaged from 3000 measurements during 1 h is 4.55 eV. Panels d and e show the IE measurement of MoS₂-A and MoS₂-B, respectively. The photoemission threshold energy for this second slope is 5.40 eV.

The ionization energy (IE) was measured by photoelectron spectroscopy in air (PESA) using RKI Instruments Model AC-2 system with 100 nW deuterium lamp power with a step of 0.05

eV. **Fig. A.I.1d-e** shows the PESA results for each sample at two different positions. Each IE value in **Table A.I.1** was obtained as an average from 7 measurements. The threshold of (photoelectron yield)^{1/3} as a function of the UV excitation energy is the IE, that is, valence band maximum (VBM) position, of the sample. The IE values measured before and after exfoliation are almost identical and within the uncertainty of the instrument. Also, the IE is similar for both MoS₂ samples corresponding to the value of 5.65 ± 0.05 eV which is similar to that reported by Schlaf et al.¹⁷⁷ The only variability observed in the IE measurements across a single crystal surface is the occasional presence of a second slope (position 2, **Fig. A.I.1d-e**). The presence of a second slope is in agreement with the spatial variation measured by photoemission and can also be explained by the presence of a surface layer with lower IE values (~ 5.40 eV).¹⁷⁸ Taking a bandgap of 1.3 eV measured by scanning tunneling spectroscopy,¹⁶⁸ the measured Φ indicates the presence of both polarities as sketched in **Fig. A.I.2**. The estimated electron affinity of about 4.35 ± 0.05 eV is in agreement with reported electron affinity.¹⁷²

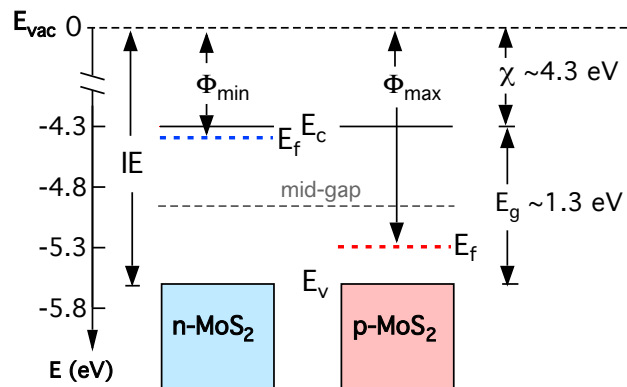


Fig. A.I.2 Band diagram constructed from the Φ measurements on two different MoS₂ crystals, and using the measured values of electron affinity ($\chi = 4.3$ eV) and bandgap ($E_g = 1.3$ eV).

Air stability characterization on other exfoliated TMDs

In order to analyze the air stability of different TMD surfaces, we used Kelvin probe and photoelectron spectroscopy in air (PESA) measurements to investigate the variation in air stability between geological MoS₂, MoSe₂, WS₂, and WSe₂. The IE variation of TMD samples was measured in air by PESA using a RKI Instruments Model AC-2 system with 100 nW deuterium lamp power with a step of 0.05 eV for as received samples (stored in air for various months) and immediately after exfoliation (**Table A.I.2**). Each IE value in **Table A.I.2** was obtained as an average from 3 measurements. The Φ air stability was measured in air by the Kelvin probe (SKP 5050, KP Technology) technique with Au as the reference material ($\Phi = 5.15$ eV). Both characterization techniques present an uncertainty below 0.05 eV.

The IE values measured before and after exfoliation are almost identical and within the uncertainty of the instrument (**Table A.I.2**), indicating that IE is not affected by the degree of contamination or oxidation of TMDs at that time scale.

Table A.I.2 IE measurements on MoS₂, MoSe₂, WS₂, and WSe₂ before and immediately after mechanical exfoliation.

	Ionization Energy (eV)			
	MoS ₂	MoSe ₂	WS ₂	WSe ₂
Before exfoliation	5.72 ± 0.05	5.51 ± 0.03	5.45 ± 0.03	5.62 ± 0.05
After exfoliation	5.69 ± 0.03	5.51 ± 0.05	5.43 ± 0.05	5.59 ± 0.03

Fig. A.I.3 shows the effect of Φ as function of time exposure in air for all TMDs. As described in previous section, the time dependent behavior could arise from the adsorption of contaminants

from the atmosphere or oxidation. The work function values stabilize close to the pre-exfoliated surface value after 24 h exposure to the ambient for all samples with the following values: Φ (MoS₂)_{after} = 5.18 eV, Φ (MoSe₂)_{after} = 4.60 eV, Φ (WS₂)_{after} = 4.66 eV and Φ (WSe₂)_{after} = 4.49 eV.

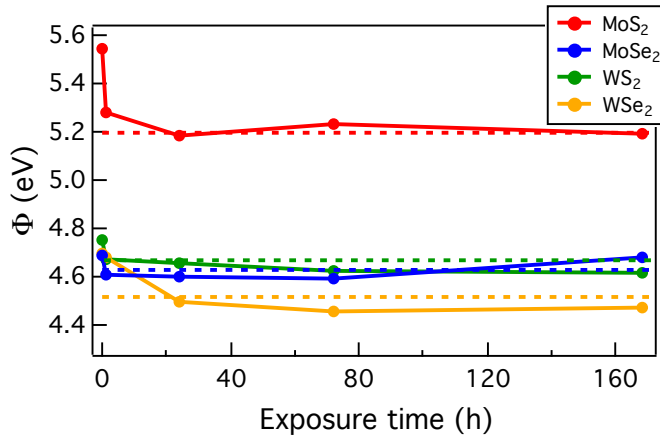


Fig. A.I.3 TMD stability as function of time exposure in air. The plot shows the Φ measured immediately after exfoliation (0 h) and after different exposure times in air (1 h, 24 h, 72 h, and 168 h). The pre-exfoliation Φ value is represented by the dashed lines for each sample, measured on as-received samples exposed to air for long periods of time (< 1 month).

Electronic characterization on other exfoliated 2-D materials

A brief summary of electronic structure characterization done in different exfoliated 2-D materials is presented in **Table A.I.3**. Φ was measured in air using a scanning Kelvin probe (SKP 5050, KP Technology) with Au as the reference material ($\Phi = 5.15$ eV). PESA was performed using a RKI Instruments Model AC-2 system with 100 nW deuterium lamp power with a step of 0.05 eV. Both characterization techniques present an uncertainty below 0.05 eV.

Table A.I.3 Electronic structure characterization done on geological and synthesized 2-D materials.

Sample	IE (eV)	Φ (eV)
^a MoSe ₂	5.62	4.44
^a WS ₂	5.51	4.93
^a WSe ₂	5.45	4.51
^b HfS ₂	5.45	4.84
^b HfSe ₂	5.50	4.77
^a SnS ₂	5.68	5.22
^c black phos.	5.29	4.46

a. Mineral provided by Prof. Wallace's group

b. Grown by Prof. Hinkle's group

c. Grown by Prof. Kloc's group

Conclusions

In summary, the results shown point out that the measured n- and p-type conductivity characteristics of exfoliated geological MoS₂ could be caused by adsorbed contaminants that can generate spatial variations in the conductivity. The presence of such impurities in geological MoS₂ induces discrepancies in the work function as measured by Kelvin probe. Therefore, it is indispensable to understand and to account for the fact that such variations are likely present in current device fabrication processes incorporating MoS₂. This represents an important limitation for flakes exfoliated from geological samples, for that reason Chapter CHAPTER 4 offers a different approach to obtain TMD flakes. In addition, the contamination and oxidation can alter the electronic properties of the TMD surfaces, with the corresponding impact on the electrical performance of any TMD-based device.

APPENDIX II
CONVENTIONAL OPVS USING NiO_x DEPOSITED
BY PLD AS HOLE TRANSPORT LAYER

In Chapters 1 and 3, the importance of obtaining new materials to substitute the highly acidic PEDOT:PSS hole transport layer (HTL) was stated. As a p-type metal oxide with wide bandgap ($E_g > 3$ eV)¹⁷⁹ and valence band energy close to the HOMO of various donor materials used in organic photovoltaic (OPV) bulk heterojunctions (BHJs),¹⁸⁰ NiO_x is an ideal candidate to replace poly(3,4-ethylenedioxythiophene):poly(styrenesulfonate) PEDOT:PSS.¹⁷⁹ Previously, p-type crystalline and amorphous NiO_x thin films have been deposited by pulsed-laser deposition (PLD),¹⁸¹ sputtering,^{182,183} and solution-deposition¹⁷⁹ as efficient HTLs in poly(3-hexylthiophene):phenyl-C60-butyric acid methyl ester (P3HT:PCBM) OPV devices, with device performance similar or superior to the one employing PEDOT:PSS. Here we explore the fabrication of OPV devices with conventional architectures using NiO_x films deposited by PLD at different oxygen partial pressures and post-deposition conditions as HTL.

To study the electronic properties of NiO_x, NiO_x films were deposited by PLD using a KrF laser ($\lambda = 248$ nm) on top of patterned ITO on glass (20 Ω /square, Xinyan). The laser frequency was 10 Hz, with an energy of 30 mJ, and the substrate temperature was kept at room temperature. Before deposition, the PLD chamber was evacuated to a pressure of $<10^{-6}$ Torr. The process was carried out at different oxygen partial pressures, ranging from 1 mT to 25 mT.

The ionization energy (IE) of NiO_x films, with 30 nm thickness, was measured by photoelectron spectroscopy in air (PESA) using RKI Instruments Model AC-2 system with 100 nW deuterium

lamp power with a step of 0.05 eV. PESA spectra for NiO_x films deposited at different oxygen partial pressures, ranging from 1 mT to 25 mT (**Fig. A.II.1a**). **Fig. A.II.1b** depicts α^2 from UV-vis absorption measurements performed for the NiO_x films used to obtain bandgap values. The calculated bandgap increase as the oxygen partial pressure increases. The Φ of the NiO_x films was also measured in air by the Kelvin probe (SKP 5050, KP Technology) technique with Au as the reference material ($\Phi = 5.15$ eV). The summary of IE, Φ , and bandgap measurements are presented in **Table A.II.1**. Each IE and Φ value was obtained as an average from 3 measurements. The IE and Φ values remained constant independent of deposition conditions at ~ 5.2 eV and ~ 4.9 eV, respectively, similar to those reported in literature.¹⁸¹

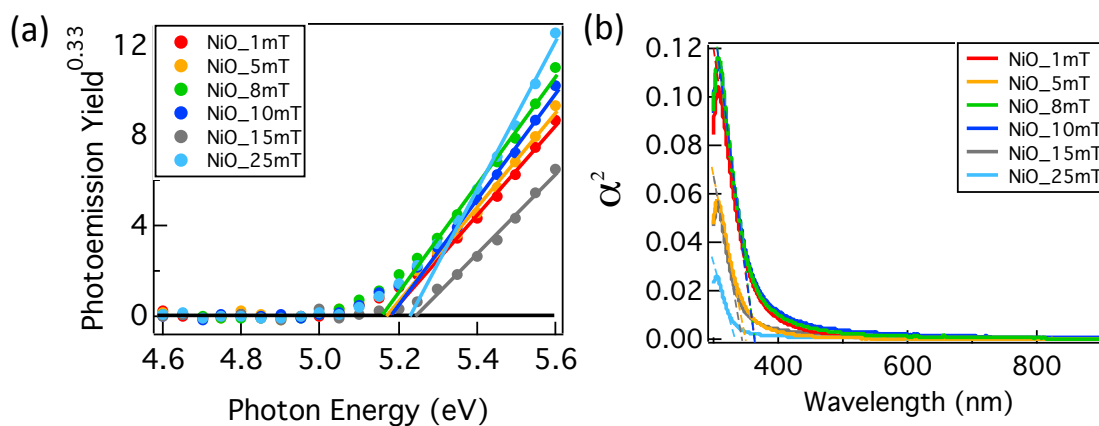


Fig. A.II.1 Electronic properties characterization for NiO_x films deposited by PLD using oxygen partial pressure of 1 mT (red), 5 mT (orange), 8 mT (green), 10 mT (blue), 15 mT (gray), and 25 mT (cyan). (a) Photoelectron spectroscopy in air and (b) UV-vis absorption. Dashed lines in (b) indicate the extrapolated bandgap values.

Table A.II.1 Summary of electronic properties of NiO_x films deposited at different oxygen partial pressures.

O ₂ Pressure (mT)	IE (eV)	Φ (eV)	E _g (eV)
1	5.18 ± 0.03	4.90 ± 0.03	3.42
5	5.17 ± 0.03	4.92 ± 0.01	3.53
8	5.16 ± 0.03	4.97 ± 0.02	3.42
10	5.18 ± 0.03	4.88 ± 0.02	3.41
15	5.24 ± 0.03	4.89 ± 0.01	3.59
25	5.23 ± 0.03	4.89 ± 0.01	3.72

*NiO_x films provided by Prof. Quevedo's group

Conventional P3HT:PCBM OPVs were fabricated using the NiO_x HTLs. After NiO_x films deposition, some NiO_x films were annealed at 300 °C for 2 h under O₂ atmosphere and air. P3HT (RMI-001E, Rieke Metals, Inc.) and PCBM (Solenne BV) were dissolved at 1:1 weight ratio in anhydrous chlorobenzene (Sigma-Aldrich). To achieve active layer thicknesses of 210 nm, 23:23 mg/mL of BHJ solution was spin-coated at 1200 rpm. The thickness of the active layer was calculated by UV-vis absorption based on calibration using profilometry. The BHJ films were annealed at 170 °C for 10 min. For reference devices, PEDOT:PSS (Clevios P VP AI 4083, Heraeus) was mixed with isopropanol in a 7:3 volume ratio, and the solution was stirred for 30 min. The PEDOT:PSS solution was then spin-coated in air at 4000 rpm for 30 s on top of the patterned ITO. Finally, 7 nm of Ca and 100 nm of Al electrode were thermally evaporated (Angstrom Engineering) to complete the devices, with area of 0.11 cm² each.

The performance of NiO_x films as HTL using conventional P3HT:PCBM OPVs (**Fig. A.II.2**) was measured using a class AAA solar simulator (Sun 3000, Abet Technologies) contained AM1.5G filter, with the intensity adjusted to 100 mW/cm² using a calibrated photodiode with KG5 filter (RR_227 KG5, Abet Technologies). The J-V measurement was performed in N₂ using a low-noise sourcemeter (2635A, Keithley) controlled by LabView (National Instruments). A 2.5

mm diameter aperture was placed in front of each device to rigorously define the illumination area to 0.049 cm^2 .

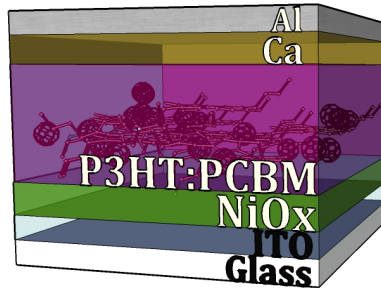


Fig. A.II.2 Conventional device architecture using NiO_x films as HTL.

Fig. A.II.3a,b shows that all devices with as-deposited NiO_x HTL perform poorly under AM 1.5G 100 mW/cm^2 illumination and under darkness conditions. The series resistance (R_{se}) is much higher in the as-deposited NiO_x devices as compared to PEDOT:PSS (**Table A.II.2**).

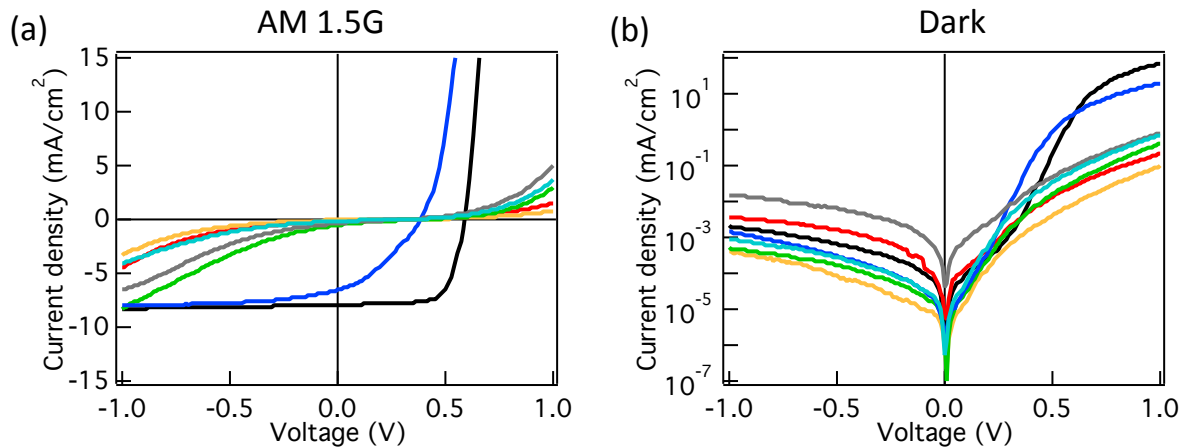


Fig. A.II.3 J-V response under (a) AM 1.5 100 mW/cm^2 and (b) darkness for conventional P3HT:PCBM OPVs with as-deposited NiO_x films deposited at different oxygen partial pressure as HTL, 1 mT (red), 5 mT (orange), 8 mT (green), 10 mT (blue), 15 mT (gray), and 25 mT (cyan).

A clear correlation can be observed between the resistivity (ρ) of the as-deposited NiO_x HTL films obtained from Hall effect measurements and the R_{se} of OPV devices using the as-deposited

NiO_x HTL (**Fig. A.II.4**). Both parameters, ρ and R_{se} , show a minimum at 10 mT. This correlation indicates that the high R_{se} obtained in the as-deposited NiO_x devices is mainly caused by the NiO_x HTL and not because the ITO/NiO_x and NiO_x/P3HT:PCBM interfaces.

Table A.II.2 Performance of conventional P3HT:PCBM OPVs with as-deposited NiO_x HTL under AM 1.5G 100 mW/cm² illumination.

HTL	V _{oc} (V)	J _{sc} (mA/cm ²)	FF (%)	Eff (%)	R _{se} (Ω cm ²)	R _{sh} (Ω cm ²)
PEDOT:PSS	0.590 ± 0.000	7.93 ± 0.08	0.713 ± 0.006	3.34 ± 0.04	4.7 ± 1.3	1.71E+06 ± 5.59E+03
NiO _x 1mT	0.318 ± 0.036	0.18 ± 0.08	0.232 ± 0.023	0.01 ± 0.01	2211.0 ± 2167.1	6.64E+06 ± 5.89E+06
NiO _x 5mT	0.288 ± 0.025	0.06 ± 0.04	0.158 ± 0.015	0.00 ± 0.00	2207.1 ± 822.8	8.36E+06 ± 3.75E+06
NiO _x 8mT	0.372 ± 0.096	0.52 ± 0.49	0.160 ± 0.016	0.04 ± 0.04	539.2 ± 230.8	6.34E+06 ± 2.26E+06
NiO _x 10mT	0.387 ± 0.006	6.53 ± 0.48	0.345 ± 0.030	0.88 ± 0.15	16.3 ± 3.5	2.99E+06 ± 2.48E+05
NiO _x 15mT	0.315 ± 0.036	0.35 ± 0.10	0.196 ± 0.005	0.02 ± 0.01	292.3 ± 101.2	2.46E+06 ± 2.94E+06
NiO _x 25mT	0.292 ± 0.010	0.16 ± 0.11	0.193 ± 0.010	0.01 ± 0.01	363.9 ± 164.4	6.35E+06 ± 2.47E+06

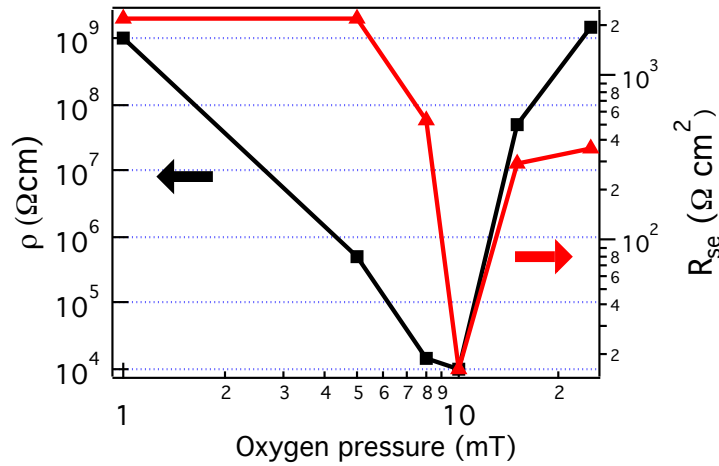


Fig. A.II.4 NiO_x films resistivity from Hall effect measurements (black), showing a positive correlation with R_{se} from OPVs fabricated with NiO_x HTL (red).

To reduce the resistivity, NiO_x films deposited at 10 mT oxygen partial pressure were subjected to a post-deposition annealing treatment at 300 °C for 2 hours under air and O₂ rich atmosphere. The summary of IE, Φ , and bandgap measurements performed on annealed NiO_x films are presented in **Table A.II.3**. As shown, the annealing process did not have an effect on the electronic properties of the NiO_x films compared to the as-deposited films.

Table A.II.3 Electronic properties of NiO_x films deposited at 10 mT at different annealing conditions.

Annealing cond.	IE (eV)	Φ (eV)	Eg (eV)
No annealing	5.18 ± 0.03	4.88 ± 0.02	3.41
air	5.17 ± 0.03	4.96 ± 0.03	3.40
O ₂	5.18 ± 0.03	4.96 ± 0.01	3.42

Fig. A.II.5 shows J-V curves under AM1.5G 100 mW/cm² illumination for devices fabricated with annealed NiO_x HTL. The J-V curve of the device fabricated with NiO_x annealed in air developed a distinct S-shape, significantly decreasing device FF (**Fig. A.II.5**, blue). S-shaped J-V curves have been attributed to inefficient collection of one type of carriers that can be caused by variable electric field distributions, or low transport layer conductivity.¹⁸⁴ By increasing the conductivity of the NiO_x HTL performing the annealing under O₂ atmosphere (**Fig. A.II.5**, red), a performance similar to that using PEDOT:PSS is achieved for conventional P3HT:PCBM OPVs. However, the η value is lower than that of the control device with PEDOT:PSS HTL at $2.93 \pm 0.69\%$. When we examine the other device parameters (**Table A.II.4**), we find that FF and J_{sc} of the annealed NiO_x in O₂ are only 5% lower compared to the PEDOT:PSS. A small decrease of 3% in V_{oc} for the NiO_x device (0.572 ± 0.004 V) compared to the PEDOT:PSS device (0.589 ± 0.004 V) was also observed. However, the R_{se} value is still higher than that of the control device with PEDOT:PSS HTL at $11.4 \pm 3.0 \Omega \text{ cm}^2$.

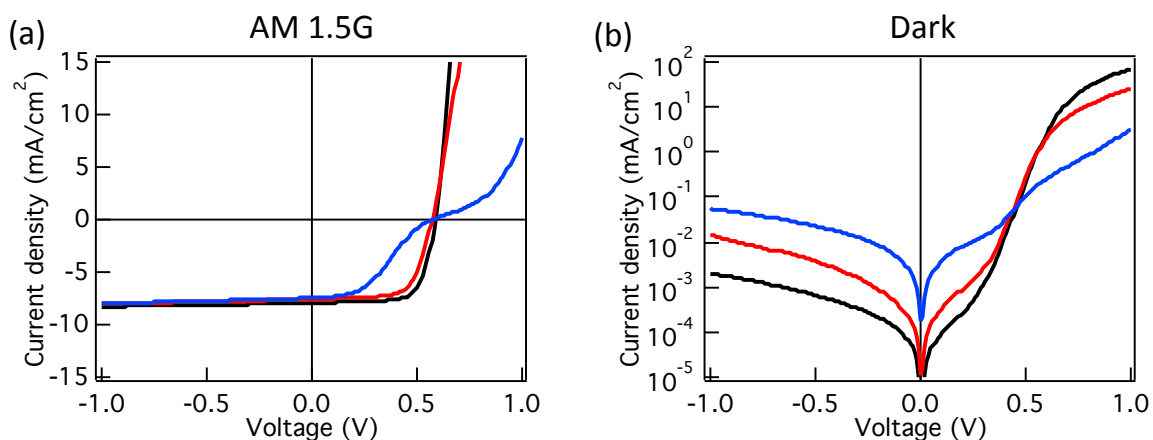


Fig. A.II.5 J-V response under (a) AM 1.5 100 mW/cm² and (b) darkness for conventional P3HT:PCBM OPVs with NiO_x films deposited 10 mT oxygen partial pressure, annealed at 300 °C for 2 h in air (blue) and under O₂ atmosphere (red) as HTL.

Table A.II.4 Performance of conventional P3HT:PCBM OPVs with annealed NiO_x HTL under AM 1.5G 100 mW/cm² illumination.

HTL	V _{oc} (V)	J _{sc} (mA/cm ²)	FF ()	Eff (%)	R _{se} (Ω cm ²)	R _{sh} (Ω cm ²)
PEDOT:PSS	0.589 ± 0.004	7.93 ± 0.28	0.713 ± 0.024	3.33 ± 0.19	4.8 ± 1.0	1.73E+06 ± 5.30E+03
NiO _x 300 °C in air	0.570 ± 0.012	7.44 ± 0.09	0.395 ± 0.033	1.68 ± 0.17	48.7 ± 12.1	1.13E+06 ± 1.51E+06
NiO _x 300 °C in O ₂	0.572 ± 0.004	7.57 ± 0.24	0.676 ± 0.016	2.93 ± 0.06	11.4 ± 3.0	5.76E+05 ± 4.78E+05

The results of this study so far indicate that NiO_x films deposited by PLD may be used in conventional BHJ OPV devices. Results showed similar efficiency for solar cells with NiO_x HTLs annealed at 300 °C for 2 h under O₂ rich atmosphere compared to PEDOT:PSS control. Further studies will evaluate the effect of annealed NiO_x films on the device specific mechanisms enabling high performance.

REFERENCES

- (1) Grossiord, N.; Kroon, J. M.; Andriessen, R.; Blom, P. W. Degradation Mechanisms in Organic Photovoltaic Devices. *Organic Electronics* **2012**, *13*, 432–456.
- (2) Ahmad, J.; Bazaka, K.; Anderson, L. J.; White, R. D.; Jacob, M. V. Materials and Methods for Encapsulation of OPV: a Review. *Renew. Sustainable Energy Rev.* **2013**, *27*, 104–117.
- (3) Brabec, C. J. Organic Photovoltaics: Technology and Market. *Sol. Energ. Mat. Sol. Cells* **2004**, *83*, 273–292.
- (4) Shaheen, S. E.; Ginley, D. S.; Jabbour, G. E. Organic-Based Photovoltaics: Toward Low-Cost Power Generation. *MRS Bull.* **2005**, *30* (01), 10–19.
- (5) Chaar, El, L.; Iamont, L. A.; Zein, El, N. Review of Photovoltaic Technologies. *Renew. Sustainable Energy Rev.* **2011**, *15*, 2165–2175.
- (6) Kippelen, B.; Brédas, J.-L. Organic Photovoltaics. *Energy Environ. Sci.* **2009**, *2* (3), 241–332.
- (7) Blom, P. W.; Mihailetschi, V. D.; Koster, L. J. A.; Markov, D. E. Device Physics of Polymer:Fullerene Bulk Heterojunction Solar Cells. *Adv. Mater.* **2007**, *19* (12), 1551–1566.
- (8) Steim, R.; Kogler, F. R.; Brabec, C. J. Interface Materials for Organic Solar Cells. *J. Mater. Chem.* **2010**, *20* (13), 2499–2512.
- (9) Yang, X.; Loos, J.; Veenstra, S. C.; Verhees, W. J. H.; Wienk, M. M.; Kroon, J. M.; Michels, M. A. J.; Janssen, R. A. J. Nanoscale Morphology of High-Performance Polymer Solar Cells. *Nano Lett.* **2005**, *5* (4), 579–583.
- (10) Bavel, S. S. V.; Sourty, E.; With, G. de; Loos, J. Three-Dimensional Nanoscale Organization of Bulk Heterojunction Polymer Solar Cells. *Nano Lett.* **2009**, *9* (2), 507–513.
- (11) Kamat, P. V. Meeting the Clean Energy Demand: Nanostructure Architectures for Solar Energy Conversion. *J. Phys. Chem. C* **2007**, *111* (7), 2834–2860.
- (12) Dimitrakopoulos, C. D.; Mascaro, D. J. Organic Thin-Film Transistors: a Review of Recent Advances. *IBM J. Res. Dev.* **2001**, *45* (1), 11–27.

- (13) Hoppe, H.; Sariciftci, N. S. Organic Solar Cells: an Overview. *J. Mater. Res.* **2004**, *19* (07), 1924–1945.
- (14) Liu, F.; Shao, S.; Guo, X.; Zhao, Y.; Xie, Z. Efficient Polymer Photovoltaic Cells Using Solution-Processed MoO₃ As Anode Buffer Layer. *Sol. Energ. Mat. Sol. Cells* **2010**, *94* (5), 842–845.
- (15) Ghasemi Varnamkhasti, M.; Fallah, H. R.; Mostajaboddavati, M.; Ghasemi, R.; Hassanzadeh, A. Comparison of Metal Oxides as Anode Buffer Layer for Small Molecule Organic Photovoltaic Cells. *Sol. Energ. Mat. Sol. Cells* **2012**, *98*, 379–384.
- (16) Spanggaard, H.; Krebs, F. C. A Brief History of the Development of Organic and Polymeric Photovoltaics. *Sol. Energ. Mat. Sol. Cells* **2004**, *83*, 125–146.
- (17) Kasap, S. O. *Principles of Electronic Materials and Devices*, 3rd ed.; McGraw-Hill: New York, 2007; Vol. 81.
- (18) Zilberberg, K.; Meyer, J.; Riedl, T. Solution Processed Metal-Oxides for Organic Electronic Devices. *J. Mater. Chem. C* **2013**, *1* (32), 4796.
- (19) Gilot, J.; Wienk, M. M.; Janssen, R. A. J. Double and Triple Junction Polymer Solar Cells Processed From Solution. *Appl. Phys. Lett.* **2007**, *90* (14), 143512–143512–3.
- (20) Hau, S. K.; Yip, H.-L.; Baek, N. S.; Zou, J.; O'Malley, K.; Jen, A. K. Y. Air-Stable Inverted Flexible Polymer Solar Cells Using Zinc Oxide Nanoparticles as an Electron Selective Layer. *Appl. Phys. Lett.* **2008**, *92* (25), 253301.
- (21) Hösel, M.; Søndergaard, R. R.; Jørgensen, M.; Krebs, F. C. Fast Inline Roll-to-Roll Printing for Indium-Tin-Oxide-Free Polymer Solar Cells Using Automatic Registration. *Energy Technology* **2013**, *1* (1), 102–107.
- (22) Li, N.; Stubhan, T.; Luechinger, N. A.; Halim, S. C.; Matt, G. J.; Ameri, T.; Brabec, C. J. Inverted Structure Organic Photovoltaic Devices Employing a Low Temperature Solution Processed WO₃ Anode Buffer Layer. *Organic Electronics* **2012**, *13*, 2479–2484.
- (23) Hammond, S. R.; Meyer, J.; Widjonarko, N. E.; Ndione, P. F.; Sigdel, A. K.; Garcia, A.; Miedaner, A.; Lloyd, M. T.; Kahn, A.; Ginley, D. S. Low-Temperature, Solution-Processed Molybdenum Oxide Hole-Collection Layer for Organic Photovoltaics. *J. Mater. Chem.* **2012**, *22* (7), 3249–3254.
- (24) Zilberberg, K.; Trost, S.; Schmidt, H.; Riedl, T. Solution Processed Vanadium Pentoxide as Charge Extraction Layer for Organic Solar Cells. *Adv. Energy Mater.* **2011**, *1* (3), 377–381.

- (25) Wang, Q. H.; Kalantar-Zadeh, K.; Kis, A.; Coleman, J. N.; Strano, M. S. Electronics and Optoelectronics of Two-Dimensional Transition Metal Dichalcogenides. *Nat. Nanotechnol.* **2012**, *7* (11), 699–712.
- (26) Yun, W. S.; Han, S. W.; Hong, S. C.; Kim, I. G.; Lee, J. D. Thickness and Strain Effects on Electronic Structures of Transition Metal Dichalcogenides: 2H-MX₂ Semiconductors (M= Mo, W; X= S, Se, Te). *Phys. Rev. B* **2012**, *85* (3), 033305.
- (27) Radisavljevic, B.; Whitwick, M. B.; Kis, A. Integrated Circuits and Logic Operations Based on Single-Layer MoS₂. *ACS Nano* **2011**, *5* (12), 9934–9938.
- (28) Kuc, A.; Zibouche, N.; Heine, T. Influence of Quantum Confinement on the Electronic Structure of the Transition Metal Sulfide TS₂. *Phys. Rev. B* **2011**, *83* (24), 245213.
- (29) Radisavljevic, B.; Radenovic, A.; Brivio, J.; Giacometti, V.; Kis, A. Single-Layer MoS₂ Transistors. *Nat. Nanotechnol.* **2011**, *6* (3), 147–150.
- (30) Novoselov, K. S.; Jiang, D.; Schedin, F.; Booth, T. J.; Khotkevich, V. V.; Morozov, S. V.; Geim, A. K. Two-Dimensional Atomic Crystals. *Proc. Natl. Acad. Sci. U.S.A.* **2005**, *102* (30), 10451–10453.
- (31) Wang, H.; Yu, L.; Lee, Y.-H.; Shi, Y.; Hsu, A.; Chin, M. L.; Li, L.-J.; Dubey, M.; Kong, J.; Palacios, T. Integrated Circuits Based on Bilayer MoS₂ Transistors. *Nano Lett.* **2012**, *12* (9), 4674–4680.
- (32) Al-Dirini, F.; Hossain, F. M.; Mohammed, M. A.; Hossain, M. S.; Nirmalathas, A.; Skafidas, E. Monolayer MoS₂ Self-Switching Diodes. *J. Appl. Phys.* **2016**, *119* (4), 044506.
- (33) Frey, G. L.; Reynolds, K. J.; Friend, R. H.; Cohen, H.; Feldman, Y. Solution-Processed Anodes From Layer-Structure Materials for High-Efficiency Polymer Light-Emitting Diodes. *J. Am. Chem. Soc.* **2003**, *125* (19), 5998–6007.
- (34) Choi, W.; Cho, M. Y.; Konar, A.; Lee, J. H.; Cha, G. B.; Hong, S. C.; Kim, S.; Kim, J.; Jena, D.; Joo, J.; Kim, S. High-Detectivity Multilayer MoS₂ Phototransistors with Spectral Response From Ultraviolet to Infrared. *Adv. Mater.* **2012**, *24* (43), 5832–5836.
- (35) Kuc, A.; Zibouche, N.; Heine, T. Influence of Quantum Confinement on the Electronic Structure of the Transition Metal Sulfide TS₂. *Phys. Rev. B* **2011**, *83* (24), 245213.

- (36) Alharbi, F.; Bass, J. D.; Salhi, A.; Alyamani, A.; Kim, H.-C.; Miller, R. D. Abundant Non-Toxic Materials for Thin Film Solar Cells: Alternative to Conventional Materials. *Renewable Energy* **2011**, *36* (10), 2753–2758.
- (37) Gupta, A.; Sakthivel, T.; Seal, S. Recent Development in 2D Materials Beyond Graphene. *Prog. Mat. Sci.* **2015**.
- (38) Jeong, S.; Yoo, D.; Jang, J.-T.; Kim, M.; Cheon, J. Well-Defined Colloidal 2-D Layered Transition-Metal Chalcogenide Nanocrystals via Generalized Synthetic Protocols. *J. Am. Chem. Soc.* **2012**, *134*, 18233–18236.
- (39) Yeh, T. C.; Zhu, Q.; Buchholz, D. B.; Martinson, AB; Chang, R.; Mason, T. O. Amorphous Transparent Conducting Oxides in Context: Work Function Survey, Trends, and Facile Modification. *Appl. Surf. Sci.* **2015**, *330*, 405–410.
- (40) Hsu, C.-W.; Wang, L.; Su, W.-F. Effect of Chemical Structure of Interface Modifier of TiO₂ On Photovoltaic Properties of Poly (3-Hexylthiophene)/TiO₂ Layered Solar Cells. *J. Colloid Interface Sci.* **2009**, *329* (1), 182–187.
- (41) Powell, R. J. Interface Barrier Energy Determination From Voltage Dependence of Photoinjected Currents. *J. Appl. Phys.* **1970**, *41* (6), 2424.
- (42) Bahadur, L.; Hamdani, M.; Koenig, J. F.; Chartier, P. Studies on Semiconducting Thin Films Prepared by the Spray Pyrolysis Technique for Photoelectrochemical Solar Cell Applications: Preparation and Properties of ZnO. *Sol. Energ. Mater.* **1986**, *14* (2), 107–120.
- (43) Znaidi, L.; Soler Illia, G.; Benyahia, S.; Sanchez, C.; Kanaev, A. V. Oriented ZnO Thin Films Synthesis by Sol–Gel Process for Laser Application. *Thin Solid Films* **2003**, *428* (1), 257–262.
- (44) Cheng, X. L.; Zhao, H.; Huo, L. H.; Gao, S.; Zhao, J. G. ZnO Nanoparticulate Thin Film: Preparation, Characterization and Gas-Sensing Property. *Sensor. Actuat. B-Chem.* **2004**, *102* (2), 248–252.
- (45) Li, H.; Wang, J.; Liu, H.; Zhang, H.; Li, X. Zinc Oxide Films Prepared by Sol–Gel Method. *J. Cryst. Growth* **2005**, *275* (1), 943–946.
- (46) Ohya, Y.; Saiki, H.; Takahashi, Y. Preparation of Transparent, Electrically Conducting ZnO Film From Zinc Acetate and Alkoxide. *J. Mater. Sci.* **1994**, *29* (15), 4099–4103.
- (47) Ohyama, M.; Kouzuka, H.; Yoko, T. Sol-Gel Preparation of ZnO Films with Extremely Preferred Orientation Along (002) Plane From Zinc Acetate Solution. *Thin Solid Films* **1997**, *306* (1), 78–85.

- (48) Nguyen, H. T.; Nguyen, N. D.; Lee, S. Application of Solution-Processed Metal Oxide Layers as Charge Transport Layers for CdSe/ZnS Quantum-Dot LEDs. *Nanotechnology* **2013**, *24* (11), 115201.
- (49) Park, J. S.; Lee, J. M.; Hwang, S. K.; Lee, S. H.; Lee, H.-J.; Lee, B. R.; Park, H. I.; Kim, J.-S.; Yoo, S.; Song, M. H. A ZnO/N-Doped Carbon Nanotube Nanocomposite Charge Transport Layer for High Performance Optoelectronics. *J. Mater. Chem.* **2012**, *22* (25), 12695–12700.
- (50) White, M. S.; Olson, D. C.; Shaheen, S. E.; Kopidakis, N.; Ginley, D. S. Inverted Bulk-Heterojunction Organic Photovoltaic Device Using a Solution-Derived ZnO Underlayer. *Appl. Phys. Lett.* **2006**, *89* (14), 143517.
- (51) Kuwabara, T.; Kawahara, Y.; Yamaguchi, T.; Takahashi, K. Characterization of Inverted-Type Organic Solar Cells with a ZnO Layer as the Electron Collection Electrode by Ac Impedance Spectroscopy. *ACS Appl. Mater. Interfaces* **2009**, *1* (10), 2107–2110.
- (52) Sun, Y.; Seo, J. H.; Takacs, C. J.; Seifert, J.; Heeger, A. J. Inverted Polymer Solar Cells Integrated with a Low-Temperature-Annealed Sol-Gel-Derived ZnO Film as an Electron Transport Layer. *Adv. Mater.* **2011**, *23* (14), 1679–1683.
- (53) Small, C. E.; Chen, S.; Subbiah, J.; Amb, C. M.; Tsang, S.-W.; Lai, T.-H.; Reynolds, J. R.; So, F. High-Efficiency Inverted Dithienogermole-Thienopyrrolodione-Based Polymer Solar Cells. *Nature Photon.* **2011**, *6* (2), 115–120.
- (54) Kyaw, A. K. K.; Sun, X. W.; Jiang, C. Y.; Lo, G. Q.; Zhao, D. W.; Kwong, D. L. An Inverted Organic Solar Cell Employing a Sol-Gel Derived ZnO Electron Selective Layer and Thermal Evaporated MoO₃ Hole Selective Layer. *Appl. Phys. Lett.* **2008**, *93* (22), 221107.
- (55) Amb, C. M.; Craig, M. R.; Koldemir, U.; Subbiah, J.; Choudhury, K. R.; Gevorgyan, S. A.; Jørgensen, M.; Krebs, F. C.; So, F.; Reynolds, J. R. Aesthetically Pleasing Conjugated Polymer:Fullerene Blends for Blue-Green Solar Cells via Roll-to-Roll Processing. *ACS Appl. Mater. Interfaces* **2012**, *4* (3), 1847–1853.
- (56) Lira-Cantu, M.; Krebs, F. C. Hybrid Solar Cells Based on MEH-PPV and Thin Film Semiconductor Oxides (TiO₂, Nb₂O₅, ZnO, CeO₂ And CeO₂-TiO₂): Performance Improvement During Long-Time Irradiation. *Sol. Energ. Mat. Sol. Cells* **2006**, *90* (14), 2076–2086.

- (57) Lloyd, M. T.; Peters, C. H.; Garcia, A.; Kauvar, I. V.; Berry, J. J.; Reese, M. O.; McGehee, M. D.; Ginley, D. S.; Olson, D. C. Influence of the Hole-Transport Layer on the Initial Behavior and Lifetime of Inverted Organic Photovoltaics. *Sol. Energ. Mat. Sol. Cells* **2011**, *95* (5), 1382–1388.
- (58) Lee, Y.-J.; Wang, J.; Cheng, S. R.; Hsu, J. W. P. Solution Processed ZnO Hybrid Nanocomposite with Tailored Work Function for Improved Electron Transport Layer in Organic Photovoltaic Devices. *ACS Appl. Mater. Interfaces* **2013**, *5* (18), 9128–9133.
- (59) Jo, S. B.; Lee, J. H.; Sim, M.; Kim, M.; Park, J. H.; Choi, Y. S.; Kim, Y.; Ihn, S.-G.; Cho, K. High Performance Organic Photovoltaic Cells Using Polymer-Hybridized ZnO Nanocrystals as a Cathode Interlayer. *Adv. Energy Mater.* **2011**, *1* (4), 690–698.
- (60) Choi, K. C.; Lee, E. J.; Baek, Y. K.; Kim, M. J.; Kim, Y. D.; Shin, P. W. Modifying Hydrogen Bonding Interaction in Solvent and Dispersion of ZnO Nanoparticles: Impact on the Photovoltaic Performance of Inverted Organic Solar Cells. *RSC Adv.* **2014**, *4*.
- (61) Ma, W.; Yang, C.; Gong, X.; Lee, K.; Heeger, A. J. Thermally Stable, Efficient Polymer Solar Cells with Nanoscale Control of the Interpenetrating Network Morphology. *Adv. Funct. Mater.* **2005**, *15* (10), 1617–1622.
- (62) van Bavel, S.; Sourty, E.; de With, G.; Veenstra, S.; Loos, J. Three-Dimensional Nanoscale Organization of Polymer Solar Cells. *J. Mater. Chem.* **2009**, *19* (30), 5388–5393.
- (63) Marsh, R. A.; Hodgkiss, J. M.; Albert-Seifried, S.; Friend, R. H. Effect of Annealing on P3HT:PCBM Charge Transfer and Nanoscale Morphology Probed by Ultrafast Spectroscopy. *Nano Lett.* **2010**, *10* (3), 923–930.
- (64) Oklobia, O.; Shafai, T. S. A Quantitative Study of the Formation of PCBM Clusters Upon Thermal Annealing of P3HT/PCBM Bulk Heterojunction Solar Cell. *Sol. Energ. Mat. Sol. Cells* **2013**, *117*, 1–8.
- (65) Savenije, T. J.; Kroeze, J. E.; Yang, X.; Loos, J. The Effect of Thermal Treatment on the Morphology and Charge Carrier Dynamics in a Polythiophene–Fullerene Bulk Heterojunction. *Adv. Funct. Mater.* **2005**, *15* (8), 1260–1266.
- (66) van Bavel, S. S.; Bärenklau, M.; de With, G.; Hoppe, H.; Loos, J. P3HT/PCBM Bulk Heterojunction Solar Cells: Impact of Blend Composition and 3D Morphology on Device Performance. *Adv. Funct. Mater.* **2010**, *20* (9), 1458–1463.

- (67) Chirvase, D.; Parisi, J.; Hummelen, J. C.; Dyakonov, V. Influence of Nanomorphology on the Photovoltaic Action of Polymer–Fullerene Composites. *Nanotechnology* **2004**, *15* (9), 1317.
- (68) Bertho, S.; Janssen, G.; Cleij, T. J.; Conings, B.; Moons, W.; Gadisa, A.; D’Haen, J.; Goovaerts, E.; Lutsen, L.; Manca, J. Effect of Temperature on the Morphological and Photovoltaic Stability of Bulk Heterojunction Polymer: Fullerene Solar Cells. *Sol. Energ. Mat. Sol. Cells* **2008**, *92* (7), 753–760.
- (69) Watts, B.; Belcher, W. J.; Thomsen, L.; Ade, H.; Dastoor, P. C. A Quantitative Study of PCBM Diffusion During Annealing of P3HT: PCBM Blend Films. *Macromolecules* **2009**, *42* (21), 8392–8397.
- (70) Li, Z.; Wong, H. C.; Huang, Z.; Zhong, H.; Tan, C. H. Performance Enhancement of Fullerene-Based Solar Cells by Light Processing. *Nat. Commun.* **2013**, *4*, 2227.
- (71) Cowan, S. R.; Wang, J.; Yi, J.; Lee, Y.-J.; Olson, D. C.; Hsu, J. W. P. Intensity and Wavelength Dependence of Bimolecular Recombination in P3HT:PCBM Solar Cells: a White-Light Biased External Quantum Efficiency Study. *J. Appl. Phys.* **2013**, *113* (15), 154504.
- (72) Lee, Y.-J.; Davis, R. J.; Lloyd, M. T.; Provencio, P. P.; Prasankumar, R. P.; Hsu, J. W. P. Open-Circuit Voltage Improvement in Hybrid ZnO-Polymer Photovoltaic Devices with Oxide Engineering. *IEEE J. Sel. Top. Quant. Electron.* **2010**, *16* (6), 1587–1594.
- (73) Waldauf, C.; Morana, M.; Denk, P.; Schilinsky, P.; Coakley, K.; Choulis, S. A.; Brabec, C. J. Highly Efficient Inverted Organic Photovoltaics Using Solution Based Titanium Oxide as Electron Selective Contact. *Appl. Phys. Lett.* **2006**, *89* (23), 233517.
- (74) Reese, M. O.; Sigdel, A. K.; Berry, J. J.; Ginley, D. S.; Shaheen, S. E. A Simple Miniature Controlled-Atmosphere Chamber for Optoelectronic Characterizations. *Sol. Energ. Mat. Sol. Cells* **2010**, *94* (7), 1254–1258.
- (75) Kamalasanan, M. N.; Chandra, S. Sol-Gel Synthesis of ZnO Thin Films. *Thin Solid Films* **1996**, *288* (1-2), 112–115.
- (76) Bandyopadhyay, S.; Paul, G. K.; Roy, R.; Sen, S. K.; Sen, S. Study of Structural and Electrical Properties of Grain-Boundary Modified ZnO Films Prepared by Sol–Gel Technique. *Mater. Chem. Phys.* **2002**, *74* (1), 83–91.
- (77) Fujihara, S.; Sasaki, C.; Kimura, T. Crystallization Behavior and Origin of C-Axis Orientation in Sol–Gel-Derived ZnO: Li Thin Films on Glass Substrates. *Appl. Surf. Sci.* **2001**, *180* (3), 341–350.

- (78) Bach, H.; Krause, D. *Thin Films on Glass*, 1st ed.; Springer: Berlin, 1997.
- (79) Aricò, A. S.; Bruce, P.; Scrosati, B.; Tarascon, J.-M.; van Schalkwijk, W. Nanostructured Materials for Advanced Energy Conversion and Storage Devices. *Nat. Mater.* **2005**, *4* (5), 366–377.
- (80) Rolison, D. R. Catalytic Nanoarchitectures--the Importance of Nothing and the Unimportance of Periodicity. *Science* **2003**, *299* (5613), 1698–1701.
- (81) Fernández-García, M.; Martínez-Arias, A.; Hanson, J. C.; Rodriguez, J. A. Nanostructured Oxides in Chemistry: Characterization and Properties. *Chem. Rev.* **2004**, *104* (9), 4063–4104.
- (82) Franke, M. E.; Koplín, T. J.; Simon, U. Metal and Metal Oxide Nanoparticles in Chemiresistors: Does the Nanoscale Matter? *Small* **2006**, *2*, 36–50.
- (83) Gupta, A. K.; Gupta, M. Synthesis and Surface Engineering of Iron Oxide Nanoparticles for Biomedical Applications. *Biomaterials* **2005**, *26* (18), 3995–4021.
- (84) Shrotriya, V.; Li, G.; Yao, Y.; Chu, C.-W.; Yang, Y. Transition Metal Oxides as the Buffer Layer for Polymer Photovoltaic Cells. *Appl. Phys. Lett.* **2006**, *88* (7), 073508–073508–3.
- (85) Kim, D. Y.; Subbiah, J.; Sarasqueta, G.; So, F.; Ding, H.; Gao, Y. The Effect of Molybdenum Oxide Interlayer on Organic Photovoltaic Cells. *Appl. Phys. Lett.* **2009**, *95* (9), 093304–1–093304–3.
- (86) Kröger, M.; Hamwi, S.; Meyer, J.; Riedl, T.; Kowalsky, W.; Kahn, A. Role of the Deep-Lying Electronic States of MoO₃ In the Enhancement of Hole-Injection in Organic Thin Films. *Appl. Phys. Lett.* **2009**, *95* (12), 123301.
- (87) Meyer, J.; Khalandovsky, R.; Görrn, P.; Kahn, A. MoO₃ Films Spin-Coated From a Nanoparticle Suspension for Efficient Hole-Injection in Organic Electronics. *Adv. Mater.* **2011**, *23* (1), 70–73.
- (88) Girotto, C.; Voroshazi, E.; Cheyns, D.; Heremans, P.; Rand, B. P. Solution-Processed MoO₃ Thin Films as a Hole-Injection Layer for Organic Solar Cells. *ACS Appl. Mater. Interfaces* **2011**, *3* (9), 3244–3247.
- (89) Jørgensen, M.; Norrman, K.; Krebs, F. C. Stability/Degradation of Polymer Solar Cells. *Sol. Energ. Mat. Sol. Cells* **2008**, *92* (7), 686–714.

- (90) Lloyd, M. T.; Olson, D. C.; Lu, P.; Fang, E.; Moore, D. L.; White, M. S.; Reese, M. O.; Ginley, D. S.; Hsu, J. W. P. Impact of Contact Evolution on the Shelf Life of Organic Solar Cells. *J. Mater. Chem.* **2009**, *19* (41), 7638–7642.
- (91) Lee, Y.-J.; Yi, J.; Gao, G. F.; Koerner, H.; Park, K.; Wang, J.; Luo, K.; Vaia, R. A.; Hsu, J. W. P. Low-Temperature Solution-Processed Molybdenum Oxide Nanoparticle Hole Transport Layers for Organic Photovoltaic Devices. *Adv. Energy Mater.* **2012**, *2* (10), 1193–1197.
- (92) Bilecka, I.; Djerdj, I.; Niederberger, M. One-Minute Synthesis of Crystalline Binary and Ternary Metal Oxide Nanoparticles. *Chem. Commun.* **2008**, No. 7, 886.
- (93) Choi, J. G.; Thompson, L. T. XPS Study of as-Prepared and Reduced Molybdenum Oxides. *Appl. Surf. Sci.* **1996**, *93*, 143–149.
- (94) Arnoldussen, T. C. Electrochromism and Photochromism in MoO₃ Films. *J. Electrochem. Soc.* **1976**, *123* (4), 527–531.
- (95) Liu, W.; Yang, X.; Zhang, Y.; Xu, M.; Chen, H. Ultra-Stable Two-Dimensional MoS₂ Solution for Highly Efficient Organic Solar Cells. *RSC Adv.* **2014**, *4* (62), 32744–32748.
- (96) Yang, X.; Fu, W.; Liu, W.; Hong, J.; Cai, Y.; Jin, C.; Xu, M.; Wang, H.; Yang, D.; Chen, H. Engineering Crystalline Structures of Two-Dimensional MoS₂ Sheets for High-Performance Organic Solar Cells. *J. Mater. Chem. A* **2014**, *2* (21), 7727–7733.
- (97) Tsai, M. L.; Su, S. H.; Chang, J. K.; Tsai, D. S.; Chen, C. H.; Wu, C. I. Monolayer MoS₂ Heterojunction Solar Cells. *ACS Nano* **2014**, *8*, 8317–8322.
- (98) Jaramillo, T. F.; Jorgensen, K. P.; Bonde, J.; Nielsen, J. H.; Horch, S.; Chorkendorff, I. Identification of Active Edge Sites for Electrochemical H₂ Evolution From MoS₂ Nanocatalysts. *Science* **2007**, *317* (5834), 100–102.
- (99) Lee, Y.-H.; Zhang, X. Q.; Zhang, W.; Chang, M.-T.; Lin, C. T.; Chang, K. D.; Yu, Y. C.; Wang, J. T.-W.; Chang, C.-S.; Li, L.-J.; Lin, T. W. Synthesis of Large-Area MoS₂ Atomic Layers with Chemical Vapor Deposition. *Adv. Mater.* **2012**, *24* (17), 2320–2325.
- (100) Wang, X.; Feng, H.; Wu, Y.; Jiao, L. Controlled Synthesis of Highly Crystalline MoS₂ Flakes by Chemical Vapor Deposition. *J. Am. Chem. Soc.* **2013**, *135*, 5304–5307.

- (101) Xi, Y.; Serna, M. I.; Cheng, L.; Gao, Y.; Baniasadi, M.; Rodriguez-Davila, R.; Kim, J.; Quevedo-Lopez, M. A.; Minary-Jolandan, M. Fabrication of MoS₂ Thin Film Transistors via Selective-Area Solution Deposition Methods. *J. Mater. Chem. C* **2015**, *3* (16), 3842–3847.
- (102) Radisavljevic, B.; Kis, A. Mobility Engineering and a Metal–Insulator Transition in Monolayer MoS₂. *Nat. Mater.* **2013**, *12* (9), 815–820.
- (103) Kappera, R.; Voiry, D.; Yalcin, S. E.; Branch, B.; Gupta, G.; Mohite, A. D.; Chhowalla, M. Phase-Engineered Low-Resistance Contacts for Ultrathin MoS₂ Transistors. *Nat. Mater.* **2014**, *13*, 1128–1134.
- (104) Wang, X.; Zhi, L.; Müllen, K. Transparent, Conductive Graphene Electrodes for Dye-Sensitized Solar Cells. *Nano Lett.* **2008**, *8* (1), 323–327.
- (105) Coleman, J. N.; Lotya, M.; O’Neill, A.; Bergin, S. D.; King, P. J.; Khan, U.; Young, K.; Gaucher, A.; De, S.; Smith, R. J. Two-Dimensional Nanosheets Produced by Liquid Exfoliation of Layered Materials. *Science* **2011**, *331* (6017), 568–571.
- (106) Eda, G.; Yamaguchi, H.; Voiry, D.; Fujita, T.; Chen, M.; Chhowalla, M. Photoluminescence From Chemically Exfoliated MoS₂. *Nano Lett.* **2011**, *11* (12), 5111–5116.
- (107) O’Neill, A.; Khan, U.; Coleman, J. N. Preparation of High Concentration Dispersions of Exfoliated MoS₂ With Increased Flake Size. *Chem. Mater.* **2012**, *24*, 2414–2421.
- (108) Jawaid, A.; Nepal, D.; Park, K.; Jespersen, M.; Qualley, A.; Mirau, P.; Drummy, L. F.; Vaia, R. A. Mechanism for Liquid Phase Exfoliation of MoS₂. *Chem. Mater.* **2015**, *28*, 337–348.
- (109) Ibrahim, M. A.; Lan, T.; Huang, J. K.; Chen, Y. Y.; Wei, K. H. High Quantity and Quality Few-Layers Transition Metal Disulfide Nanosheets From Wet-Milling Exfoliation. *RSC Adv.* **2013**, *3*, 13193–13202.
- (110) Lotya, M.; Rakovich, A.; Donegan, J. F.; Coleman, J. N. Measuring the Lateral Size of Liquid-Exfoliated Nanosheets with Dynamic Light Scattering. *Nanotechnology* **2013**, *24* (26), 265703.
- (111) Ganorkar, S.; Kim, J.; Kim, Y. H.; Kim, S. Effect of Precursor on Growth and Morphology of MoS₂ Monolayer and Multilayer. *J. Phys. Chem. Solids* **2015**, *87*, 32–37.

- (112) Choudhary, N.; Park, J.; Hwang, J. Y.; Chung, H.-S.; Dumas, K. H.; Khondaker, S. I.; Choi, W.; Jung, Y. Centimeter Scale Patterned Growth of Vertically Stacked Few Layer Only 2D MoS₂/WS₂ Van Der Waals Heterostructure. *Sci. Rep.* **2016**, *6*, 25456.
- (113) Gong, Y.; Lin, J.; Wang, X.; Shi, G.; Lei, S.; Lin, Z.; Zou, X.; Ye, G.; Vajtai, R.; Yakobson, B. I.; Terrones, H.; Terrones, M.; Tay, B. K.; Lou, J.; Pantelides, S. T.; Liu, Z.; Zhou, W.; Ajayan, P. M. Vertical and in-Plane Heterostructures From WS₂/MoS₂ Monolayers. *Nat. Mater.* **2014**, *13* (12), 1135–1142.
- (114) Ishihara, S.; Hibino, Y.; Sawamoto, N.; Suda, K.; Ohashi, T.; Matsuura, K.; Machida, H.; Ishikawa, M.; Sudoh, H.; Wakabayashi, H.; Ogura, A. Properties of Single-Layer MoS₂ Film Fabricated by Combination of Sputtering Deposition and Post Deposition Sulfurization Annealing Using (T-C₄H₉)₂S₂. *Jpn. J. Appl. Phys.* **2016**, *55* (6S1), 06GF01.
- (115) Loh, T. A. J.; Chua, D. H. C. Pulsed Laser Fabricated Few-Layer MoS₂ on Silver. *Chem. Phys. Lett.* **2014**, *610-611*, 284–287.
- (116) Serna, M. I.; Yoo, S. H.; Moreno, S.; Xi, Y.; Oviedo, J. P.; Choi, H.; Alshareef, H. N.; Kim, M. J.; Minary-Jolandan, M.; Quevedo-Lopez, M. A. Large-Area Deposition of MoS₂ By Pulsed Laser Deposition with *In Situ* Thickness Control. *ACS Nano* **2016**, *10* (6), 6054–6061.
- (117) Altavilla, C.; Sarno, M.; Ciambelli, P. A Novel Wet Chemistry Approach for the Synthesis of Hybrid 2D Free-Floating Single or Multilayer Nanosheets of MS₂@Oleylamine (M= Mo, W). *Chem. Mater.* **2011**, *23* (17), 3879–3885.
- (118) Thripuranthaka, M.; Kashid, R. V.; Rout, C. S.; Late, D. J. Temperature Dependent Raman Spectroscopy of Chemically Derived Few Layer MoS₂ And WS₂ Nanosheets. *Appl. Phys. Lett.* **2014**, *104* (8), 081911.
- (119) Nagaraju, G.; Tharamani, C. N.; Chandrappa, G. T.; Livage, J. Hydrothermal Synthesis of Amorphous MoS₂ Nanofiber Bundles via Acidification of Ammonium Heptamolybdate Tetrahydrate. *Nanoscale Res Lett* **2007**, *2* (9), 461–468.
- (120) Mahler, B.; Hoepfner, V.; Liao, K.; Ozin, G. A. Colloidal Synthesis of 1T-WS₂ And 2H-WS₂ Nanosheets: Applications for Photocatalytic Hydrogen Evolution. *J. Am. Chem. Soc.* **2014**, *136*, 14121–14127.
- (121) Addou, R.; McDonnell, S.; Barrera, D.; Guo, Z.; Azcatl, A.; Wang, J.; Zhu, H.; Hinkle, C. L.; Quevedo-Lopez, M.; Alshareef, H. N.; Colombo, L.; Hsu, J. W. P.; Wallace, R. M. Impurities and Electronic Property Variations of Natural MoS₂ Crystal Surfaces. *ACS Nano* **2015**, *9*, 9124–9133.

- (122) Harpeness, R.; Gedanken, A.; Weiss, A. M.; Slifkin, M. A. Microwave-Assisted Synthesis of Nanosized MoSe₂. *J. Mater. Chem.* **2003**, *13* (10), 2603–2606.
- (123) Xu, Z.; Shen, C.; Hou, Y.; Gao, H.; Sun, S. Oleylamine as Both Reducing Agent and Stabilizer in a Facile Synthesis of Magnetite Nanoparticles. *Chem. Mater.* **2009**, *21* (9), 1778–1780.
- (124) Jung, W.; Lee, S.; Yoo, D.; Jeong, S.; Miró, P.; Kuc, A.; Heine, T.; Cheon, J. Colloidal Synthesis of Single-Layer MSe₂ (M = Mo, W) Nanosheets via Anisotropic Solution-Phase Growth Approach. *J. Am. Chem. Soc.* **2015**, *137* (23), 7266–7269.
- (125) Sun, S.; Murray, C. B.; Weller, D.; Folks, L.; Moser, A. Monodisperse FePt Nanoparticles and Ferromagnetic FePt Nanocrystal Superlattices. *Science* **2000**, *287*, 1989–1992.
- (126) Elkins, K. E.; Vedantam, T. S.; Liu, J. P.; Zeng, H.; Sun, S. Ultrafine FePt Nanoparticles Prepared by the Chemical Reduction Method. *Nano Lett.* **2003**, *3*, 1647–1649.
- (127) Lin, Y.-Y.; Wang, D.-Y.; Yen, H.-C.; Chen, H.-L.; Chen, C.-C.; Chen, C.-M.; Tang, C.-Y.; Chen, C.-W. Extended Red Light Harvesting in a Poly (3-Hexylthiophene)/Iron Disulfide Nanocrystal Hybrid Solar Cell. *Nanotechnology* **2009**, *20* (40), 405207.
- (128) Alstrup, I.; Chorkendorff, I.; Candia, R.; Clausen, B. S.; Topsøe, H. A Combined X-Ray Photoelectron and Mössbauer Emission Spectroscopy Study of the State of Cobalt in Sulfided, Supported, and Unsupported Co-Mo Catalysts. *J. Catal.* **1982**, *77* (2), 397–409.
- (129) Anwar, M.; Hogarth, C. A.; Bulpett, R. Effect of Substrate Temperature and Film Thickness on the Surface Structure of Some Thin Amorphous Films of MoO₃ Studied by X-Ray Photoelectron Spectroscopy (ESCA). *J. Mater. Sci.* **1989**, *24* (9), 3087–3090.
- (130) Benoist, L.; Gonbeau, D.; Pfister-Guillouzo, G.; Schmidt, E.; Meunier, G.; Levasseur, A. XPS Analysis of Oxido-Reduction Mechanisms During Lithium Intercalation in Amorphous Molybdenum Oxysulfide Thin Films. *Solid State Ion.* **1995**, *76* (1-2), 81–89.
- (131) Benoist, L.; Gonbeau, D.; Pfister-Guillouzo, G.; Schmidt, E.; Meunier, G.; Levasseur, A. X-Ray Photoelectron Spectroscopy Characterization of Amorphous Molybdenum Oxysulfide Thin Films. *Thin Solid Films* **1995**, *258*, 110–114.
- (132) Davis, S. M.; Carver, J. C. Oxygen Chemisorption at Defect Sites in MoS₂ And ReS₂ Basal Plane Surfaces. *Appl. Surf. Sci.* **1984**, *20*, 193–198.

- (133) Shi, Y.; Huang, J. K.; Jin, L.; Hsu, Y.-T.; Yu, S. F.; Li, L.-J.; Yang, H. Y. Selective Decoration of Au Nanoparticles on Monolayer MoS₂ Single Crystals. *Sci. Rep.* **2013**, *3*, 1839.
- (134) Malmsten, G.; Thorén, I.; Högberg, S.; Bergmark, J. E. Selenium Compounds Studied by Means of ESCA. *Phys. Scripta* **1971**, *3*, 96–100.
- (135) Abdallah, W. A.; Nelson, A. E. Characterization of MoSe₂(0001) and Ion-Sputtered MoSe₂ By XPS. *J. Mater. Sci.* **2005**, *40* (9-10), 2679–2681.
- (136) Salvati, L.; Makovsky, L. E.; Stencel, J. M.; Brown, F. R.; Hercules, D. M. Surface Spectroscopic Study of Tungsten-Alumina Catalysts Using X-Ray Photoelectron, Ion Scattering, and Raman Spectroscopies. *J. Phys. Chem.* **1981**, *85* (24), 3700–3707.
- (137) Martin, I.; Vinatier, P.; Levasseur, A.; Dupin, J. C.; Gonbeau, D. XPS Analysis of the Lithium Intercalation in Amorphous Tungsten Oxysulfide Thin Films. *J. Power Sources* **1999**, *81-82*, 306–311.
- (138) Martin-Litas, I.; Vinatier, P.; Levasseur, A.; Dupin, J. C.; Gonbeau, D.; Weill, F. Characterisation of R.F. Sputtered Tungsten Disulfide and Oxysulfide Thin Films. *Thin Solid Films* **2002**, *416*, 1–9.
- (139) Zong, X.; Han, J.; Ma, G.; Yan, H.; Wu, G.; Li, C. Photocatalytic H₂ Evolution on CdS Loaded with WS₂ As Cocatalyst Under Visible Light Irradiation. *J. Phys. Chem. C* **2011**, *115*, 12202–12208.
- (140) Boscher, N. D.; Carmalt, C. J.; Parkin, I. P. Atmospheric Pressure Chemical Vapor Deposition of WSe₂ Thin Films on Glass—Highly Hydrophobic Sticky Surfaces. *J. Mater. Chem.* **2006**, *16* (1), 122–127.
- (141) Li, H.; Zhang, Q.; Yap, C. C. R.; Tay, B. K.; Edwin, T. H. T.; Olivier, A.; Baillargeat, D. From Bulk to Monolayer MoS₂: Evolution of Raman Scattering. *Adv. Funct. Mater.* **2012**, *22* (7), 1385–1390.
- (142) Wang, H.; Kong, D.; Johannes, P.; Cha, J. J.; Zheng, G.; Yan, K.; Liu, N.; Cui, Y. MoSe₂ And WSe₂ Nanofilms with Vertically Aligned Molecular Layers on Curved and Rough Surfaces. *Nano Lett.* **2013**, *13*, 3426–3433.
- (143) Berkdemir, A.; Gutiérrez, H. R.; Botello-Méndez, A. R.; Perea-López, N.; Elías, A. L.; Chia, C.; Wang, B.; Crespi, V.; Lopez-Urías, F.; Charlier, J. C.; Terrones, H.; Terrones, M. Identification of Individual and Few Layers of WS₂ Using Raman Spectroscopy. *Sci. Rep.* **2013**, *3*, 1755.

- (144) Lee, C.; Yan, H.; Brus, L. E.; Heinz, T. F.; Hone, J.; Ryu, S. Anomalous Lattice Vibrations of Single- and Few-Layer MoS₂. *ACS Nano* **2010**, *4* (5), 2695–2700.
- (145) Tongay, S.; Zhou, J.; Ataca, C.; Lo, K.; Matthews, T. S.; Li, J.; Grossman, J. C.; Wu, J. Thermally Driven Crossover From Indirect Toward Direct Bandgap in 2D Semiconductors: MoSe₂ Versus MoS₂. *Nano Lett.* **2012**, *12* (11), 5576–5580.
- (146) Zhao, W.; Ghorannevis, Z.; Chu, L.; Toh, M.; Kloc, C.; Tan, P.-H.; Eda, G. Evolution of Electronic Structure in Atomically Thin Sheets of WS₂ And WSe₂. *ACS Nano* **2012**, *7*, 791–797.
- (147) Greiner, M. T.; Helander, M. G.; Tang, W.-M.; Wang, Z.-B.; Qiu, J.; Lu, Z.-H. Universal Energy-Level Alignment of Molecules on Metal Oxides. *Nat. Mater.* **2011**.
- (148) Xavier Crispin; Victor Geskin; Annica Crispin; Jérôme Cornil; Roberto Lazzaroni; William R Salaneck, A.; Jean-Luc Brédas. Characterization of the Interface Dipole at Organic/ Metal Interfaces. *J. Am. Chem. Soc.* **2002**, *124*, 8131–8141.
- (149) Campbell, I. H.; Rubin, S.; Zawodzinski, T. A.; Kress, J. D.; Martin, R. L.; Smith, D. L.; Barashkov, N. N.; Ferraris, J. P. Controlling Schottky Energy Barriers in Organic Electronic Devices Using Self-Assembled Monolayers. *Phys. Rev. B* **1996**, *54* (20), R14321.
- (150) Bernède, J. C.; Amory, C.; Assmann, L.; Spiesser, M. X-Ray Photoelectron Spectroscopy Study of MoTe₂ Single Crystals and Thin Films. *Appl. Surf. Sci.* **2003**, *219* (3-4), 238–248.
- (151) Bahl, M. K.; Watson, R. L.; Irgolic, K. J. X-Ray Photoemission Studies of Tellurium and Some of Its Compounds. *J. Chem. Phys.* **1977**, *66*, 5526.
- (152) Koo, J.; Jhon, Y. I.; Park, J.; Lee, J.; Jhon, Y. M.; Lee, J. H. Near-Infrared Saturable Absorption of Defective Bulk-Structured WTe₂ For Femtosecond Laser Mode-Locking. *Adv. Funct. Mater.* **2016**, *26* (41), 7454–7461.
- (153) Nefedov, V. I.; Salyn, Y. V.; Leonhardt, G.; Scheibe, R. A Comparison of Different Spectrometers and Charge Corrections Used in X-Ray Photoelectron Spectroscopy. *J Electron Spectros Relat Phenom* **1977**, *10* (2), 121–124.
- (154) Choi, S.; Shaolin, Z.; Yang, W. Layer-Number-Dependent Work Function of MoS₂ Nanoflakes. *J. Korean Phys. Soc.* **2014**, *64* (10), 1550–1555.
- (155) Gu, X.; Cui, W.; Li, H.; Wu, Z.; Zeng, Z.; Lee, S.-T.; Zhang, H.; Sun, B. A Solution-Processed Hole Extraction Layer Made From Ultrathin MoS₂ Nanosheets for Efficient Organic Solar Cells. *Adv. Energy Mater.* **2013**, *3* (10), 1262–1268.

- (156) Capasso, A.; Matteocci, F.; Najafi, L.; Prato, M.; Buha, J.; Cina, L.; Pellegrini, V.; Di Carlo, A.; Bonaccorso, F. Few-Layer MoS₂ Flakes as Active Buffer Layer for Stable Perovskite Solar Cells. *Adv. Energy Mater.* **2016**, *1600920*, 1–12.
- (157) Krebs, F. C. Fabrication and Processing of Polymer Solar Cells: a Review of Printing and Coating Techniques. *Sol. Energ. Mat. Sol. Cells* **2009**, *93* (4), 394–412.
- (158) Green, R.; Morfa, A.; Ferguson, A. J.; Kopidakis, N.; Rumbles, G.; Shaheen, S. E. Performance of Bulk Heterojunction Photovoltaic Devices Prepared by Airbrush Spray Deposition. *Appl. Phys. Lett.* **2008**, *92* (3), 033301.
- (159) Giroto, C.; Rand, B. P.; Genoe, J.; Heremans, P. Exploring Spray Coating as a Deposition Technique for the Fabrication of Solution-Processed Solar Cells. *Sol. Energ. Mat. Sol. Cells* **2009**, *93* (4), 454–458.
- (160) Brabec, C. J.; Durrant, J. R. Solution-Processed Organic Solar Cells. *MRS Bull.* **2008**, *33* (7), 670–675.
- (161) Van Le, Q.; Nguyen, T. P.; Jang, H. W.; Kim, S. Y. The Use of UV/Ozone-Treated MoS₂ Nanosheets for Extended Air Stability in Organic Photovoltaic Cells. *Phys. Chem. Chem. Phys.* **2014**, *16*, 13123.
- (162) Wang, J.; Lee, Y.-J.; Hsu, J. W. P. One-Step Synthesis of ZnO Nanocrystals in N-Butanol with Bandgap Control: Applications in Hybrid and Organic Photovoltaic Devices. *J. Phys. Chem. C* **2014**, *118* (32), 18417–18423.
- (163) Burkhard, G. F.; Hoke, E. T.; McGehee, M. D. Accounting for Interference, Scattering, and Electrode Absorption to Make Accurate Internal Quantum Efficiency Measurements in Organic and Other Thin Solar Cells. *Adv. Mater.* **2010**, *22* (30), 3293–3297.
- (164) Wang, J.; Xu, L.; Lee, Y. J.; De Anda Villa, M.; Malko, A. V.; Hsu, J. W. P. Effects of Contact-Induced Doping on the Behaviors of Organic Photovoltaic Devices. *Nano Lett.* **2015**, *15* (11), 7627–7632.
- (165) Mihailetchi, V. D.; Blom, P. W. M.; Hummelen, J. C.; Rispen, M. T. Cathode Dependence of the Open-Circuit Voltage of Polymer:Fullerene Bulk Heterojunction Solar Cells. *J. Appl. Phys.* **2003**, *94* (10), 6849–6854.
- (166) Lai, T.-H.; Tsang, S.-W.; Manders, J. R.; Chen, S.; So, F. Properties of Interlayer for Organic Photovoltaics. *Mater. Today* **2013**, *16* (11), 424–432.

- (167) Kautek, W.; Gerischer, H.; Tributsch, H. The Role of Carrier Diffusion and Indirect Optical Transitions in the Photoelectrochemical Behavior of Layer Type D-Band Semiconductors. *J. Electrochem. Soc.* **1980**, *127* (11), 2471–2478.
- (168) Addou, R.; Colombo, L.; Wallace, R. M. Surface Defects on Natural MoS₂. *ACS Appl. Mater. Interfaces* **2015**, *7*, 11921–11929.
- (169) Kam, K. K.; Parkinson, B. A. Detailed Photocurrent Spectroscopy of the Semiconducting Group VI Transition Metal Dichalcogenides. *J. Phys. Chem.* **2002**, *86*, 463–467.
- (170) Mak, K. F.; Lee, C.; Hone, J.; Shan, J.; Heinz, T. F. Atomically Thin MoS₂: A New Direct-Gap Semiconductor. *Phys. Rev. Lett.* **2010**, *105* (13), 136805.
- (171) McDonnell, S.; Addou, R.; Buie, C.; Wallace, R. M.; Hinkle, C. L. Defect-Dominated Doping and Contact Resistance in MoS₂. *ACS Nano* **2014**, *8* (3), 2880–2888.
- (172) McDonnell, S.; Azcatl, A.; Addou, R.; Gong, C.; Battaglia, C.; Chuang, S.; Cho, K.; Javey, A.; Wallace, R. M. Hole Contacts on Transition Metal Dichalcogenides: Interface Chemistry and Band Alignments. *ACS Nano* **2014**, *8*, 6265–6272.
- (173) McGovern, I. T.; Williams, R. H.; Mee, C. H. B. Electronic Properties of Cleaved Molybdenum Disulphide Surfaces. *Surf. Sci.* **1974**, *46* (2), 427–440.
- (174) Wilson, J. A.; Yoffe, A. D. The Transition Metal Dichalcogenides Discussion and Interpretation of the Observed Optical, Electrical and Structural Properties. *Adv. Phys.* **1969**, *18* (73), 193–335.
- (175) Hansen, W. N.; Hansen, G. J. Standard Reference Surfaces for Work Function Measurements in Air. *Surf. Sci.* **2001**, *481* (1-3), 172–184.
- (176) KC, S.; Longo, R. C.; Wallace, R. M.; Cho, K. Surface Oxidation Energetics and Kinetics on MoS₂ Monolayer. *J. Appl. Phys.* **2015**, *117* (13), 135301.
- (177) Schlaf, R.; Lang, O.; Pettenkofer, C.; Jaegermann, W. Band Lineup of Layered Semiconductor Heterointerfaces Prepared by Van Der Waals Epitaxy: Charge Transfer Correction Term for the Electron Affinity Rule. *J. Appl. Phys.* **1999**.
- (178) Pan, T.; Sun, L. Sub-Microscopic Phenomena of Metallic Corrosion Studied by a Combined Photoelectron Spectroscopy in Air (PESA) and Scanning Kelvin Probe Force Microscopy (SKPFM) Approach. *Int J Electrochem Sci* **2012**, *7*, 9325–9344.

- (179) Steirer, K. X.; Chesin, J. P.; Widjonarko, N. E.; Berry, J. J.; Miedaner, A.; Ginley, D. S.; Olson, D. C. Solution Deposited NiO Thin-Films as Hole Transport Layers in Organic Photovoltaics. *Organic Electronics* **2010**, *11*, 1414–1418.
- (180) Steirer, K. X.; Ndione, P. F.; Widjonarko, N. E.; Lloyd, M. T.; Meyer, J.; Ratcliff, E. L.; Kahn, A.; Armstrong, N. R.; Curtis, C. J.; Ginley, D. S.; Berry, J. J.; Olson, D. C. Enhanced Efficiency in Plastic Solar Cells via Energy Matched Solution Processed NiO_x Interlayers. *Adv. Energy Mater.* **2011**, *1*, 813–820.
- (181) Irwin, M. D.; Buchholz, D. B.; Hains, A. W.; Chang, R. P. H.; Marks, T. J. P-Type Semiconducting Nickel Oxide as an Efficiency-Enhancing Anode Interfacial Layer in Polymer Bulk-Heterojunction Solar Cells. *Proc. Natl. Acad. Sci. U.S.A.* **2008**, *105* (8), 2783–2787.
- (182) Widjonarko, N. E.; Ratcliff, E. L.; Perkins, C. L.; Sigdel, A. K.; Zakutayev, A.; Ndione, P. F.; Gillaspie, D. T.; Ginley, D. S.; Olson, D. C.; Berry, J. J. Sputtered Nickel Oxide Thin Film for Efficient Hole Transport Layer in Polymer–Fullerene Bulk-Heterojunction Organic Solar Cell. *Thin Solid Films* **2012**, *520* (10), 3813–3818.
- (183) Betancur, R.; Maymó, M.; Elias, X.; Vuong, L. T.; Martorell, J. Sputtered NiO as Electron Blocking Layer in P3HT:PCBM Solar Cells Fabricated in Ambient Air. *Sol. Energ. Mat. Sol. Cells* **2011**, *95* (2), 735–739.
- (184) Wagenpfahl, A.; Rauh, D.; Binder, M.; Deibel, C.; Dyakonov, V. S-Shaped Current-Voltage Characteristics of Organic Solar Devices. *Phys. Rev. B* **2010**, *82* (11), 115306.

BIOGRAPHICAL SKETCH

Diego Barrera Méndez was born in Mexico City, Mexico. He earned his bachelor's degree in Chemical Engineering from the University of Coahuila, Mexico in 2009. He later earned his master's degree in Environmental Engineering and Renewable Energies working with SnO₂ infrared reflective coatings on solar collectors at the Research Center for Advanced Materials (CIMAV), Mexico in 2011. After earning his master's degree, he received a full scholarship from the National Science and Technology Council (CONACyT) of Mexico to enroll in the Materials Science and Engineering PhD program at UTD under the supervision of Professor Julia Hsu in January 2012. His research focused on the synthesis of nanomaterials with suitable electronic, transport, and interfacial properties to be used as transport layer in organic photovoltaics by low-temperature processing integration techniques.

CURRICULUM VITAE
DIEGO BARRERA MENDEZ

RESEARCH EXPERIENCE

University of Texas at Dallas

Richardson, TX

Graduate Research Assistant

Jan 2012-May 2017

Conducted research on synthesis and characterization of solution processed metal oxides and transition metal dichalcogenides for organic photovoltaic application. In addition, he performed fabrication and electrical characterization of organic photovoltaic devices.

- Synthesized nanomaterials with suitable electronic, transport, chemical, and interfacial properties to be used in contact or active layer in organic or hybrid solar cells.
- Derived chemical routes to control oxidation states of the nanoparticles and correlate it with the oxidation states and the change in work function in the nanoparticles films.
- Integrated the novel materials into solar cells with low-temperature solution processing techniques.
- Understood the effects of device configuration and materials selection on the performance of organic photovoltaic devices.
- Optimized material selection and device architecture of solution processed organic photovoltaic devices.

- Thin Film Materials Characterization: Structural, Morphological, Mechanical and Electrical properties
- Advanced Microscopy: AFM, SEM, TEM
- Advanced Spectroscopy: XPS, UPS, PESA

Advanced Materials Research Center (CIMAV)

Chihuahua, Mexico

Graduate Research Assistant

Jan 2010-Dec 2012

Performed research on fabrication and characterization of tin oxide thin films for solar collector application:

- Fabricated crystalline tin oxide thin films by aerosol assisted chemical vapor deposition (AACVD).
- Characterized optical and structural properties of tin oxide thin films by spectroscopic and microscopic methods including SEM, XRD, and UV-Vis transmission.

EDUCATION

University of Texas at Dallas

Richardson, TX

Ph. D. candidate in Materials Science and Engineering

May 2017

Advisor: Prof. Julia W.P. Hsu

University of Texas at Dallas

Richardson, TX

M.S. in Materials Science and Engineering

May 2014

Advisor: Prof. Julia W.P. Hsu

Center for Advanced Materials Research (CIMAV)

Chihuahua, Mexico

M.S. in Environmental Engineering

Dec 2012

Advisor: Prof. Mario Miki-Yoshida

University of Coahuila

Saltillo, Mexico

B.E. in Chemical Engineering

Jun 2009

HONORS

CONACYT Fellowship for Foreign Study

2012-2016

PUBLICATIONS

1. Y.-J. Lee, **D. Barrera**, K. Luo, J.W.P. Hsu, In Situ Chemical Oxidation of Ultrasmall MoO_x Nanoparticles in Suspensions, *Nanotechnology* 195761 (2012). doi:10.1155/2012/195761.
2. **D. Barrera**, Y.-J. Lee, J.W.P. Hsu, Influence of ZnO sol-gel electron transport layer processing on BHJ active layer morphology and OPV performance, *Sol. Energ. Mat. Sol. Cells.* 125 (2014) 27–32. doi:10.1016/j.solmat.2014.02.014.
3. Y.-J. Lee, J. Wang, J.W. Hsu, **D. Barrera**, General method to synthesize ultrasmall metal oxide nanoparticle suspensions for hole contact layers in organic photovoltaic devices, *MRS Commun.* 5 (2015) 45-50. doi:10.1557/mrc.2015.5.
4. P. Huang, J. Du, S. S. Gunathilake, E. A. Rainbolt, J. W. Murphy, K. T. Black, **D. Barrera**, J.W.P. Hsu, B. E. Gnade, M. C. Stephan, M. C. Biewer, Benzodifuran and benzodithipene

- donor-acceptor polymers for bulk heterojunction solar cells, *J. Mater. Chem. A*, 3 (2015) 6980. doi:10.1039/c5ta00936g
5. J. Wang, V. Ibarra, **D. Barrera**, L. Xu, Y.-J. Lee, J.W.P. Hsu, Solution Synthesized p-Type Copper Gallium Oxide Nanoplates as Hole Transport Layer for Organic Photovoltaic Devices, *J. Phys. Chem. Lett.* 6 (2015) 1071–1075. doi:10.1021/acs.jpcclett.5b00236.
 6. R. Addou, S. McDonnell, **D. Barrera**, Z. Guo, A. Azcatl, J. Wang, H. Zhu, C. L. Hinkle, M. Quevedo-Lopez, H. N Alshareef, L. Colombo, J. W. P. Hsu, and R. M. Wallace, Conductivity Variation of Exfoliated Natural MoS₂ Crystals, *ACS Nano*, 9 (2015) 9124-9133.
 7. R. Y, Y. Nie, L. Walsh, R. Addou, C. Liang, N. Lu, A. Barton, H. Zhu, Z. Che, **D. Barrera**, L. Cheng, P. Cha, M. Kim, J.W.P. Hsu, J. Kim, L. Colombo, Y. Chabal, R. Wallace, K. Cho, C. Hinkle, Nucleation and Growth of WSe₂: Enabling Larger Grain Transition Metal Dichalcogenides, *Adv. Mater.*, **in rev.**
 8. R. Longo, R. Addou, KC Santosh, J. Noh, C. Smith, **D. Barrera**, J.W.P. Hsu, R. Wallace, K. Cho, Intrinsic Air Stability Mechanisms of Two-Dimensional Transition Metal Dichalcogenide Surfaces, *2D Materials*, **in rev.**
 9. **D. Barrera**, Q. Wang, Y.-J. Lee, L. Cheng, M. Kim, J. Kim, J.W.P. Hsu, Solution synthesis of few-layered 2H MX₂ (M=Mo,W; X=S,Se) nanoflakes, *J. Mat. Chem. C*, 5 (2017) 2859-2864.
 10. **D. Barrera**, A. Jawaid, T. Daunis, L. Cheng, Q. Wang, Y.-J. Lee, M. Kim, J. Kim, R. Vaia, J.W.P. Hsu, Inverted OPVs with MoS₂ Hole Transport Layer Deposited by Spray Coating, *Mater. Today Energy*, **in rev.**

CONFERENCES

1. Y.-J. Lee, **D. Barrera**, J. Wang, G. Gao, S. Cheng, J.W.P. Hsu, Low Temperature Solution Processing of Inorganic Nanoparticles for Contact Layers in Organic Photovoltaics, *Electronic Materials and Applications*, Orlando, FL, January 2013, oral presentation.
2. Y.-J. Lee, J. Wang, **D. Barrera**, G. Gao, J.W.P. Hsu, Low Temperature Solution Processing of Inorganic Nanoparticles for Contact Layers in Organic Photovoltaics, *Forum on New Materials*, Montecatini Terme, Italy, June 2014, oral presentation.
3. Y.-J. Lee, **D. Barrera**, J. Wang, J.W.P. Hsu, General Method to Synthesize Ultrasmall Metal Oxide Nanoparticle Suspensions as Hole Contact Layers in Organic Photovoltaic Devices, 2014 Fall Materials Research Society Meeting, Boston, MA, December 2015, poster.

4. **D. Barrera**, Y. Lee, J. Wang, L. Cheng, J. Kim, J. W. P. Hsu, Synthesis, Characterization, and Electronic Structure of Solution Processed Ultrathin MoS₂, 2015 Spring Materials Research Society Meeting, San Francisco, CA, April 2015, poster.
5. R. Addou, H. Zhu, **D. Barrera**, Santosh KC., J. Wang, K. Cho, J. Hsu, R. M. Wallace, Reactivity of Transition Metal Dichalcogenide, 2015 Spring Materials Research Society Meeting, San Francisco, CA, April 2015, oral presentation.
6. **D. Barrera**, Y. Lee, J. Wang, J. W. P. Hsu, Organic Photovoltaic: Low-cost Power Generation, BUAP University, Puebla, Mexico, June 2016, Invited talk.
7. **D. Barrera**, Q. Wang, Y.-J. Lee, A. Jawaid, L. Cheng, T. Daunis, J. Kim, R. Vaia, M. Kim, J.W.P. Hsu, Solution processed TMDs and their Integration into Organic Photovoltaics, 2016 Fall Materials Research Society Meeting, Boston, MA, December 2016, oral presentation.